Universiteit
Leiden
The Netherlands

Stimulated raman adiabatic passage in optomechanics

Fedoseev, V.

Citation
Fedoseev, V. (2022, July 7). *Stimulated raman adiabatic passage in optomechanics*. *Casimir PhD Series*. Retrieved from https://hdl.handle.net/1887/3421649

Version:	Publisher's Version
License:	Licence agreement concerning inclusion of doctoral thesis in the Institutional Repository of the University of Leiden
Downloaded from:	https://hdl.handle.net/1887/3421649

Note: To cite this publication please use the final published version (if applicable).

Stimulated Raman Adiabatic Passage in Optomechanics

Proefschrift

ter verkrijging van
de graad van doctor aan de Universiteit Leiden,
op gezag van rector magnificus prof.dr.ir. H. Bijl,
volgens besluit van het college voor promoties
te verdedigen op donderdag 7 juli 2022
klokke 10:00 uur

door

Vitaly Fedoseev

geboren te Vinnytsia (Ukraine)
in 1986

Promotor:	Prof. dr. D. Bouwmeester	
Co-promotor:	Dr. W. Löffler	
Promotiecommissie:	Prof. Dr. M. Aspelmeyer	(Vienna University)
	Prof. Dr. G. A. Steele	(TU Delft)
	Dr. D. F. E. Samtleben	(Leiden University / NIKHEF)
	Prof. Dr. J. Aarts	
	Dr. M. J. A. de Dood	
	Prof. Dr. ir. T. H. Oosterkamp	

Casimir PhD series, Delft - Leiden 2022-15 ISBN 978-90-8593-526-1

An electronic version of this thesis can be found at:
https://openaccess.leidenuniv.nl

The work described in this thesis was performed at the Kamerlingh Onnes Laboratory , Leiden University of Physics, Leiden University, The Netherlands. This work is part of the research program of the Foundation for Fundamental Research (FOM), which is part of the Netherlands Organization for Scientific Research (NWO).

Dedicated to

Nastya

&

Yakov

Contents

1 Introduction **1**
- 1.1 Motivation and outlook . . . 2
- 1.2 Basic optomechanics . . . 4
- 1.3 Membrane-in-the-middle . . . 9

2 Squeezed mechanical state **13**
- 2.1 Introduction . . . 13
- 2.2 Setup . . . 15
- 2.3 Active feedback . . . 19
- 2.4 Discussion . . . 21
- 2.5 Conclusions . . . 22

3 STIRAP of a classical state **23**
- 3.1 Introduction . . . 23
- 3.2 Experimental details . . . 27
  - 3.2.1 Setup . . . 27
  - 3.2.2 Membrane positioning . . . 28
  - 3.2.3 Membrane fabrication . . . 29
  - 3.2.4 Generation of driving pulses . . . 29
  - 3.2.5 Calibration procedure . . . 30
- 3.3 Theory . . . 32
- 3.4 Results . . . 34
  - 3.4.1 Membrane heating and non-linear effects . . . 35
- 3.5 Conclusions . . . 38

4 Quantum state transfer and entanlement via STIRAP **39**
- 4.1 STIRAP of a single phonon state . . . 39
  - 4.1.1 Introduction . . . 39

4.1.2 State preparation . . . 41
4.1.3 STIRAP . . . 42
4.1.4 Readout . . . 42
4.1.5 Discussion . . . 43
4.1.6 Other Membrane Modes . . . 45
4.1.7 Conclusions . . . 45
4.2 Creation and detection of an entangled state . . . 46

5 Cryogenic cavity **51**
5.1 Introduction . . . 51
5.2 Design . . . 52
5.3 Alignment procedure . . . 53
5.4 Membrane alignment . . . 55
5.5 Measurements . . . 57
5.6 Conclusions . . . 63

6 Setup for optomechanical quantum experiments **65**
6.1 Filter cavities . . . 66
6.1.1 Optical design . . . 66
6.1.2 Mechanical design of filter cavities . . . 72
6.1.3 Control design . . . 76
6.2 Single photon detectors . . . 79

7 Mechanical ground state **81**
7.1 Requirements . . . 81
7.2 Membrane thermometry via Anti-Stokes sideband . . . 84
7.3 Conclusions . . . 86

8 Summary **87**

Samenvatting **94**

Bibliography **94**

Curriculum Vitae **102**

List of Publications **103**

Acknowledgements **105**

1

Introduction

In 1577 the Great Comet passed close to Earth. One of the best astronomical observers of the time, Tycho Brahe, noted that the comet's tail was pointing away from the Sun. Johannes Kepler, analyzing the data recorded by Brahe and observing another comet 30 years later, concluded that there must be radiation pressure pushing the comet's tail outwards from the Sun. In a letter to Galileo Galilei he hypothesized that one day this radiation pressure could be used for solar sails.

In 1872 James Clerk Maxwell put forward his theory of electromagnetism which gave a quantitative prediction of the radiation pressure. There were several attempts to measure the light pressure by illuminating a light mill in a vacuum chamber. The main difficulty was that the residual gas in the chamber complicated the interpretation of the measurements due to convection and radiometric forces. The first conclusive experimental observation was reported by Pyotr Lebedev in 1899 who managed to decrease the residual gas pressure to $\sim 10^{-4}$ mbar by building a pump similar to the later introduced diffusion pumps.

It was shown by Vladimir Braginskii that there is a limit on the precision with which the position of an object can be continuously monitored [1]. This standard quantum limit (SQL) practically sets a lower bound on the sensitivity of optical interferometers, including gravitational wave detectors such as LIGO and VIRGO. Braginsky also proposed a way to beat the SQL by not measuring the position continuously, such measurements were termed quantum non-demolition (QND) measurements [2]. Nowadays these ideas are explored towards improving the sensitivity of the gravitational wave detectors.

Advances in the micro-electromechanical systems (MEMS) technology allowed to miniaturize optomechanical systems to the micro- and nano- scales. This allowed to reach GHz frequencies for optomechanically coupled oscillators. This is important as such mechanical oscillators are in a thermal state close to the ground state already at the dilution refrigerators temperatures, greatly facilitating experiments in the quantum regime [3, 4, 5].

Another step forward was made with the introduction of phononic crystals in optomechanical devices greatly enhancing the isolation of a mechanical mode from

its mechanical bath [6, 7].

Optomechanical devices are promising candidates to bridge disparate degrees of freedom like microwave and optical signals via a mechanical oscillator coupled to both fields [8]. This is essential in Quantum Information Science, for example for stationary (superconducting transmon) to flying (photon) qubit conversion.

Finally, optomechanical devices serve as ultra-sensitive probes of force, displacement, mass and acceleration [9] and provide a testbed for extensions of Quantum Mechanics [10].

Historically our group has a particular interest in studying massive superpositions and possible interplay of Quantum Mechanics and Gravity [11]. The idea behind it is that the gravitational self-energy might induce higher rates of decoherence than predicted by the standard quantum theory. These effects are predicted to become increasingly pronounced for larger test masses. This is one of the motivations for our group to work with relatively low frequency optomechanical devices naturally having higher effective masses. Therefore, lots of effort is put in the development of a low-vibration refrigeration capable of reaching the sub-mK regime.

1.1 Motivation and outlook

The goal of the work presented in this thesis is to build an optomechanical system based on the membrane-in-the-middle configuration operating in the quantum regime and to develop a method for a quantum state transfer between two mechanical oscillators coupled to a common optical mode.

Mechanical modes have long coherence times and can be used in quantum information as quantum memory. Therefore, a state transfer between mechanical modes may be an important tool for Quantum Information Science. It appears that the process of a state transfer can be stopped in the middle of the process and the mechanical modes become entangled [12, 13]. This brings a possibility to realize entanglement between massive oscillators which is an achievement on itself. Studies of the evolution of entangled oscillators with increasing masses may probe the parameter space where some theories predict new physics beyond predictions based on the model of environment induced decoherence in standard quantum mechanics. [11].

Several methods of a state transfer in optomechanics were demonstrated [14, 12, 15]. The demonstrated state transfer efficiency in the topological energy transfer [14, 15] was about 0.1 which is quite low. The two tone swapping method [12] requires precise control over the experimental parameters: the difference in the frequencies of the driving light tones should be equal to the difference in the mechanical frequencies of the modes adjusted by the optical spring effect within the mechanical linewidth. It is hard to realize experimentally for very high quality mechanical modes.

Stimulated Raman Adiabatic Passage (STIRAP) is a technique for a population transfer which is both robust to uncertainties in the experimental parameters and can achieve high state transfer efficiencies [16, 13]. This is a well-established technique demonstrated in many physical systems but not in optomechanics. The work shown in this thesis was to analyze the feasibility and requirements of STIRAP in op-

tomechanics as well as towards experimental realization of STIRAP of a non-classical state between two vibrational modes in the MHz range.

In section 2 of this chapter we discuss the main optomechanical concepts and effects encountered throughout this thesis. Section 3 introduces the system we are working with - a membrane inside a high finesse optical cavity.

The work presented in this thesis started with building a membrane-in-the-middle setup using a commercial SiN membrane. Chapter 2 presents a strong squeezing of a thermal mechanical state achieved in this system by parametric modulation of the optical spring effect.

Next, we introduced a phononic crystal membrane into this cavity fabricated in our group in UC Santa Barbara. These membranes possess 1-2 orders of magnitude higher mechanical quality factors for vibrational modes localized in the defect of the phononic crystal. High mechanical quality factors and the phononic crystal bandgap allowed the realization of a high efficiency state transfer between two vibrational modes of the same membrane through the optical mode using STIRAP. Such a state transfer of a classical state at room temperature is described in Chapter 3.

Chapter 4 discusses a possibility to realize STIRAP of single-phonon Fock state between two in-gap membrane modes. We show that a state transfer with fidelity of 0.6 is feasible assuming system parameters achieved in state-of-the-art devices at 1 K with single photon detection by superconducting nanowire single photon detectors. We also discuss a possibility to entangle two membrane modes and detect such an entanglement using a modified version of STIRAP.

Next, the design and fabrication of a novel cryogenic compatible optical cavity is presented. In Chapter 5 we characterize this cavity and demonstrate optical coupling to a single mode optical fiber > 0.9 at cryogenic temperatures.

In Chapter 6 we discuss a setup for quantum optomechanical experiments based on detection of Stokes and anti-Stokes photons. For example, it would be possible to realize STIRAP of a single-phonon state described in Chapter 4 using this setup. Such a setup is under construction in our lab.

In Chapter 7 we investigate the feasibility of measuring the average phonon occupation of a thermal state close to the quantum ground state in our system using a balanced heterodyne detection scheme. We found that it is not possible to do such a measurement without sending relatively strong probe light fields which most likely will heat the membrane. To do a measurement where the heating by the intracavity light fields of a probe light is weaker than the heating by the cooling light, single photon detection described in Chapter 6 is required.

The work presented in this thesis is summarized in Chapter 8 in connection to previous and future work in our lab.

1.2 Basic optomechanics

A generic optomechanical system based on a Fabry-Perot resonator is depicted in Fig. 1.1. The Fabry-Perot resonator (which will be further referred to as the optical cavity) consists of two high reflectivity mirrors where one of the mirrors is fixed while the other mirror is attached to a spring. The movable mirror on a spring system has a resonance frequency Ω.

Let's find the evolution of the intracavity light fields. Light with frequency ω_L and electric field amplitude E_{in} is sent to the cavity. Light entering the cavity will be reflected inside the cavity many times. Interference of these reflections will result in an intracavity light field amplitude E. In the steady state situation:

$$E = E_{\text{in}}t + E_{\text{in}}tr^2e^{i\phi} + E_{\text{in}}t(r^2e^{i\phi})^2 + .., \tag{1.1}$$

where t and r are amplitude transmissivity and reflectivity of each mirror (mirrors are ideal and identical, $r^2 + t^2 = 1$) and ϕ is accumulated phase in one round trip $\phi = 2\pi/\lambda \times 2L = \frac{\omega_L}{c} \times 2L$ with λ the wavelength of light, L the cavity length and c the speed of light. For this derivation we consider flat parallel mirrors for simplicity with plane waves E_{in}. Performing the summation in Eq. 1.1 we get

$$E = \frac{E_{\text{in}}t}{1 - r^2e^{i\phi}}. \tag{1.2}$$

The incoming light fields are on resonance with the cavity when $e^{i\phi} = 1$ corresponding to the frequency ω_{cav} such that $e^{i\frac{2L}{c}\omega_{\text{cav}}} = 1$ and the intracavity light fields amplitude $E = E_{\text{in}}/t$. Let's introduce the detuning Δ from the cavity resonance $\Delta = \omega_L - \omega_{\text{cav}}$. For the detuning values much smaller than the frequency between the two adjacent resonances which is equivalent to $|\phi| \ll 1$

$$e^{i\phi} = e^{i\frac{2L}{c}\omega_L} = e^{i\frac{2L}{c}\omega_L}e^{-i\frac{2L}{c}\omega_{\text{cav}}} = e^{i\frac{2L}{c}\Delta} \approx 1 + i\Delta\frac{2L}{c}. \tag{1.3}$$

Equation 1.2 can be written as

$$E_{\text{in}}t = E(1 - r^2e^{i\phi}) \approx E(1 - (1 - t^2)(1 + i\Delta\frac{2L}{c})) \approx Et^2(1 - i\Delta\frac{2L}{ct^2}). \tag{1.4}$$

We see that the intracavity light amplitude is a function of the distance between the mirrors. Therefore, the mechanical motion of the movable mirror affects the intracavity light fields. Further we will see that there is also a reverse effect where the intracavity light affects the motion of the mirror - hence the name optomechanics.

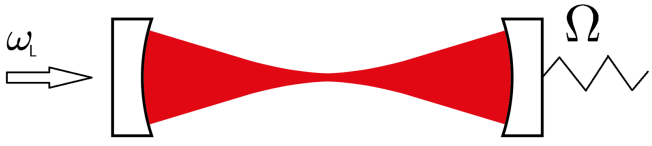

Figure 1.1: Basic optomechanical system.

Let's consider a situation where the incoming light fields are abruptly switched off. The intracavity light will decay. To find the decay rate let's consider photons inside the cavity. The probability of a photon to leave the cavity via one of the mirrors is t^2, each photon impinges on a mirror every L/c seconds, thus the energy decay rate $\kappa = t^2/(L/c)$. The intracavity electric field will decay as

$$\dot{E} = -\frac{\kappa}{2}E. \tag{1.5}$$

The 2 in the denominator comes from the fact that energy ($\propto E^2$) decays with the rate κ, electric field E decays with the rate $\kappa/2$.

Now we introduce the frame rotating at $\omega_{\rm cav}$ and find the electric field in this frame $E_{\rm cav}$. Recalling that E is the field amplitude, the intracavity field changes with time as

$$E(t) = Ee^{i\omega_L t} = E_{\rm cav}e^{i\omega_{\rm cav}t}, \tag{1.6}$$

therefore

$$E = E_{\rm cav}e^{i(\omega_{\rm cav}-\omega_L)t} = E_{\rm cav}e^{-i\Delta t}, \tag{1.7}$$

where $\Delta = \omega_L - \omega_{\rm cav}$ is the light fields detuning. Substituting E from Eq. 1.7 into Eq. 1.5 we get

$$\dot{E}_{\rm cav} = -\frac{\kappa}{2}E_{\rm cav} + i\Delta E_{\rm cav}. \tag{1.8}$$

Returning to the case of the steady state situation Eq. 1.4 can be written as

$$0 = -\frac{\kappa}{2}E_{\rm cav} + i\Delta E_{\rm cav} + \sqrt{\kappa_{\rm ext}}\sqrt{\frac{c}{2L}}E_{\rm in}, \tag{1.9}$$

where we introduced the coupling rate of the incoming light fields $\kappa_{\rm ext} = \kappa/2$. Generalizing Eq. 1.8 and 1.9 for a non-steady state we get

$$\dot{E}_{\rm cav} = -\frac{\kappa}{2}E_{\rm cav} + i\Delta E_{\rm cav} + \sqrt{\kappa_{\rm ext}}\sqrt{\frac{c}{2L}}E_{\rm in}, \tag{1.10}$$

To find the quantum analog of Eq. 1.10 we need the expressions for the incoming light intensity

$$I_{\rm in} = \frac{1}{2}c\epsilon_0|E_{\rm in}|^2 = \hbar\omega_L\langle\hat{a}^\dagger_{\rm in}\hat{a}_{\rm in}\rangle \tag{1.11}$$

and the energy of the intracavity light fields

$$W = I_{\rm cav}\frac{2L}{c} = \frac{1}{2}c\epsilon_0|E_{\rm cav}|^2 \times \frac{2L}{c} = \hbar\omega_L\langle\hat{a}^\dagger\hat{a}\rangle, \tag{1.12}$$

where ϵ_0 is the vacuum dielectric permittivity, $a_{\rm in}$ is the quantum field corresponding to the incoming light fields, $I_{\rm cav}$ is the intracavity light intensity corresponding to the running wave with amplitude $E_{\rm cav}$ and $\hat{a}$ is the intracavity quantum field. Using these expressions we get

$$\dot{\hat{a}} = -\frac{\kappa}{2}\hat{a} + i\Delta\hat{a} + \sqrt{\kappa_{\rm ext}}\hat{a}_{\rm in}. \tag{1.13}$$

Equation 1.13 is identical to the general one describing the evolution of the intracavity light fields [9] in the absence of any incoming noise $\hat{f}_{\rm in}$. We showed here an intuition behind this equation rather than its derivation.

Next, we consider how the intracavity light affects the motion of an optomechanically coupled oscillator. For the simple case shown in Fig. 1.1 the equation of motion of the movable mirror is

$$\ddot{x} + \Gamma_m \dot{x} + \Omega^2 x = \frac{F}{m}, \tag{1.14}$$

where x is the shift of the mirror along the optical axis, $\Gamma_m = \Omega/Q$ is the damping rate and Q is the mechanical quality factor, m is the mirror mass and F is the radiation pressure force due to the intracavity light fields $\hat{a}$. Each photon transfers a momentum $2\hbar\omega_L/c$ each $2L/c$ seconds, resulting in the overall force

$$F = (2\hbar\omega_L/c)/(2L/c)\langle\hat{a}^\dagger\hat{a}\rangle = \hbar\frac{\omega_L}{L}\langle\hat{a}^\dagger\hat{a}\rangle. \tag{1.15}$$

Generally, the force is

$$F = \hbar G\langle\hat{a}^\dagger\hat{a}\rangle, \tag{1.16}$$

where we introduced optomechanical coupling $G = -\partial\omega_{\rm cav}/\partial x$, in our case $G = \frac{\omega_L}{L}$.

In the case of a high-Q mechanical oscillator Eq. 1.14 can be simplified to a first order differential equation because the amplitude of oscillations cannot change fast [9]. Let's use this property:

$$x = Ae^{-i\Omega t}, \dot{x} = \dot{A}e^{-i\Omega t} - i\Omega Ae^{-i\Omega t}, \ddot{x} = -2i\Omega\dot{A}e^{-i\Omega t} - \Omega^2 Ae^{-i\Omega t}, \tag{1.17}$$

where we neglected the term containing $\ddot{A}$. Using Eq. 1.17 and 1.14 we get

$$-2i\Omega\dot{A}e^{-i\Omega t} - i\Omega\Gamma_m Ae^{-i\Omega t} = \frac{F}{m}, \tag{1.18}$$

where we neglected the term containing $\Gamma\dot{A}$ (Γ and $\dot{A}$ are small). Going back to the non-rotating frame $x = Ae^{-i\Omega t}$ we get

$$\dot{x} = (-\frac{\Gamma_m}{2} - i\Omega)x + i\frac{F}{2m\Omega}. \tag{1.19}$$

The quantum version of this equation is [9]

$$\dot{\hat{b}} = (-\frac{\Gamma_m}{2} - i\Omega)\hat{b} + i\frac{\hat{F}}{2m\Omega x_{\rm zpf}}, \tag{1.20}$$

where $\hat{x} = x_{\rm zpf}(\hat{b} + \hat{b}^\dagger)$ and $x_{\rm zpf} = \sqrt{\langle 0|\,\hat{x}^2\,|0\rangle} = \sqrt{\frac{\hbar}{2m\Omega}}$ is the zero point fluctuation amplitude, $|0\rangle$ is the mechanical vacuum state. Using Eq. 1.16 we get

$$\dot{\hat{b}} = (-\frac{\Gamma_m}{2} - i\Omega)\hat{b} + ig_0\hat{a}^\dagger\hat{a}, \tag{1.21}$$

where $g_0 = Gx_{\rm zpf}$ is the single photon optomechanical coupling rate.

Equation 1.21 together with Eq. 1.13 written in the form

$$\dot{\hat{a}} = -\frac{\kappa}{2}\hat{a} + i(\Delta_0 + g_0(\hat{b} + \hat{b}^\dagger))\hat{a} + \sqrt{\kappa_{\text{ext}}}\hat{a}_{\text{in}} \tag{1.22}$$

are the basic optomechanical equations governing the dynamics of the interaction of light fields and an optomechanically coupled oscillator. The classical version of these two coupled differential equations is used in Chapter 3.

Next, we expand the detuning Δ from Eq. 1.13 into $\Delta = \Delta_0 + \hat{x}\partial\Delta/\partial x = \Delta_0 + G\hat{x}$ and $\hat{x} = x_{\text{zpf}}(\hat{b} + \hat{b}^\dagger)$, where Δ_0 is the unperturbed laser detuning.

The energy of an optomechanical system consists of the energy of the photons $\hbar\omega_L\langle\hat{a}^\dagger\hat{a}\rangle$, energy of the phonons $\hbar\Omega\langle\hat{b}^\dagger\hat{b}\rangle$, and their interaction energy. The interaction part is the potential energy of the oscillator $-\langle\hat{F}\hat{x}\rangle = -\hbar g_0\langle\hat{a}^\dagger\hat{a}(\hat{b} + \hat{b}^\dagger)\rangle$. Now we can write the full Hamiltonian of an optomechanical system

$$\hat{H} = \hbar\omega_L\hat{a}^\dagger\hat{a} + \hbar\Omega\hat{b}^\dagger\hat{b} - \hbar g_0\hat{a}^\dagger\hat{a}(\hat{b} + \hat{b}^\dagger). \tag{1.23}$$

In Chapter 4 we use Eq. 1.23 to simulate the dynamics of an optomechanical system via the Linblad formalism requiring a Hamiltonian.

Next, we consider an oscillator in thermal equilibrium with a thermal bath at temperature T. The oscillator has a mechanical susceptibility defined through $x(\omega) = \chi(\omega)F(\omega)$

$$\chi_m(\omega) = \frac{1}{2m\Omega(\Omega - \omega - i\Gamma_m/2)}, \tag{1.24}$$

where $x(\omega)$ is the Fourier transform of the oscillator position x and $F(\omega)$ is the Fourier transform of the external force applied to the oscillator. The power spectral density (PSD) of the oscillator relates to the mean square of x via

$$\frac{1}{2\pi}\int_{-\infty}^{\infty} S_{xx}(\omega)\, d\omega = \langle x^2\rangle. \tag{1.25}$$

The fluctuation dissipation theorem relates $S_{xx}(\omega)$ to the mechanical response $\chi_m(\omega)$ in thermal equilibrium [9]:

$$S_{xx}(\omega) = \frac{2kT}{\omega}\text{Im}\chi_m(\omega) = \frac{kT}{2m\Omega^2}\frac{\Gamma_m}{(\omega - \Omega)^2 + \Gamma_m^2/4}. \tag{1.26}$$

These relationships allow us to calculate the PSD of the force exerted by the bath on the oscillator:

$$S_{FF}(\omega) = \frac{S_{xx}(\omega)}{|\chi_m(\omega)|^2} = 2kTm\Gamma_m. \tag{1.27}$$

Next, we consider the case when a constant intensity light fields with detuning Δ is sent to the cavity with an optomechanically coupled oscillator. The dynamics of the oscillator can be found by solving Eq. 1.21 and 1.22. The radiation pressure backaction alters the mechanical susceptibility to

$$\chi(\omega) = \frac{1}{2m\Omega((\Omega + \delta\Omega_{\text{opt}}) - \omega - i(\Gamma_m + \Gamma_{\text{opt}})/2)}, \tag{1.28}$$

with

$$\delta\Omega_{\rm opt} = g_0^2 n_{\rm cav}\left(\frac{\Delta-\Omega}{(\Delta-\Omega)^2+\kappa^2/4}+\frac{\Delta+\Omega}{(\Delta+\Omega)^2+\kappa^2/4}\right) \tag{1.29}$$

$$\Gamma_{\rm opt} = g_0^2 n_{\rm cav}\left(\frac{\kappa}{(\Delta+\Omega)^2+\kappa^2/4}-\frac{\kappa}{(\Delta-\Omega)^2+\kappa^2/4}\right) \tag{1.30}$$

under the assumption of small intracavity photon number $n_{\rm cav}$ resulting in $\Gamma_{\rm opt} \ll \kappa$. Now the oscillator is not in thermal equilibrium with the bath. Let's find its mean square motion $\langle x^2\rangle$. Though the mechanical susceptibility has changed to Eq. 1.28 the oscillator is still driven by the thermal force given by Eq. 1.27:

$$S_{xx}(\omega) = S_{FF}(\omega)|\chi(\omega)|^2 = \frac{kT}{2m\Omega^2}\frac{\Gamma_m}{(\omega-\Omega)^2+(\Gamma_m+\Gamma_{\rm opt})^2/4}. \tag{1.31}$$

Comparing this result to Eq. 1.26 we find

$$\langle x^2\rangle = \frac{1}{2\pi}\int_{-\infty}^{\infty} S_{xx}(\omega)\,d\omega = \frac{\Gamma_m}{\Gamma_m+\Gamma_{\rm opt}}\langle x^2\rangle|_{n_{\rm cav}=0}. \tag{1.32}$$

Now we can define the effective temperature $T_{\rm eff}$ satisfying the fluctuation-dissipation theorem:

$$T_{\rm eff} = \frac{\Gamma_m}{\Gamma_m+\Gamma_{\rm opt}}T. \tag{1.33}$$

Finding $T_{\rm eff}$ for an oscillator in the quantum regime requires consideration of the rates of the probabilities of the oscillator transitioning from the state with n phonons to the state of $n+1$ phonons [17]

$$\gamma_{n\to n+1} = \frac{x_{\rm zpf}^2}{\hbar^2}(n+1)S_{FF}(-\Omega) \tag{1.34}$$

and the rates of the probabilities of the oscillator transitioning from the state with n phonons to the state of $n-1$ phonons

$$\gamma_{n\to n-1} = \frac{x_{\rm zpf}^2}{\hbar^2}nS_{FF,\rm total}(\Omega). \tag{1.35}$$

In this case a bare mechanical oscillator is considered with $S_{FF,\rm total}$ being the total PSD due to the radiation pressure forces and the forces from the mechanical bath. The final phonon occupation $\bar{n}_f$ is obtained by finding a steady state when the probabilities of the oscillator to occupy a state n are not changing in time. This gives [17]:

$$\bar{n}_f = \frac{\gamma_{0\to1}}{\gamma_{1\to0}-\gamma_{0\to1}}. \tag{1.36}$$

Considering the same probabilities it can be shown that the state $\bar{n}_f$ is approached with the rate $\Gamma = \gamma_{1\to0}-\gamma_{0\to1}$, therefore this rate is the energy decay rate as defined above.

If the oscillator is coupled to the mechanical bath only, it has the phonon population $\bar{n}_{f,m} = n_{\rm th} = \frac{kT}{\hbar\Omega}$ for $kT \gg \hbar\Omega$ and has the energy decay $\gamma_{1\to0}-\gamma_{0\to1} = \Gamma_m$.

If the oscillator is coupled to the optical bath only, the PSD of the forces acting on it is [17]:

$$S_{FF,\mathrm{opt}}(\omega) = \frac{\hbar^2}{x_{\mathrm{zpm}}^2} g_0^2 n_{\mathrm{cav}} |\chi_{\mathrm{opt}}(\omega)|^2, \tag{1.37}$$

where $\chi_{\mathrm{opt}}(\omega) = \frac{\sqrt{\kappa}}{\kappa/2+i(\Delta-\omega)}$ is the optical susceptibility of the cavity. Now we can find the steady state phonon occupation of an oscillator coupled to the optical bath only using Eq. 1.37 and 1.36:

$$\bar{n}_{f,\mathrm{opt}} = \frac{|\chi_{\mathrm{opt}}(-\Omega)|^2}{|\chi_{\mathrm{opt}}(\Omega)|^2 - |\chi_{\mathrm{opt}}(-\Omega)|^2}. \tag{1.38}$$

The energy decay of the oscillator in this case is

$$\Gamma_{\mathrm{opt}} = g_0^2 n_{\mathrm{cav}} (|\chi_{\mathrm{opt}}(\Omega)|^2 - |\chi_{\mathrm{opt}}(-\Omega)|^2), \tag{1.39}$$

which coincides with Eq. 1.30.

Finally, we can find the steady state when the oscillator is coupled to the optical and mechanical baths simultaneously. As the optical and thermal forces are independent the total PSD of the force is the sum of the mechanical and optical components:

$$S_{FF,\mathrm{total}}(\omega) = S_{FF,m}(\omega) + S_{FF,\mathrm{opt}}(\omega). \tag{1.40}$$

Therefore,

$$\bar{n}_f = \frac{\gamma_{0\to1,m} + \gamma_{0\to1,\mathrm{opt}}}{(\gamma_{1\to0,m} + \gamma_{1\to0,\mathrm{opt}}) - (\gamma_{0\to1,m} + \gamma_{0\to1,\mathrm{opt}})} = \tag{1.41}$$

$$= \frac{\gamma_{0\to1,m} + \gamma_{0\to1,\mathrm{opt}}}{\Gamma_m + \Gamma_{\mathrm{opt}}}. \tag{1.42}$$

Using Eq. 1.36 we are getting $\gamma_{0\to1,j} = \Gamma_j \bar{n}_{f,j}$ and finally

$$\bar{n}_f = \frac{\Gamma_m n_{\mathrm{th}} + \Gamma_{\mathrm{opt}} n_{\mathrm{min}}}{\Gamma_m + \Gamma_{\mathrm{opt}}}, \tag{1.43}$$

where $n_{\mathrm{min}} = \bar{n}_{f,\mathrm{opt}}$ from Eq. 1.38.

1.3 Membrane-in-the-middle

In this section we discuss an optical cavity with a transparent dielectric membrane in the middle. The reflectivity of the membrane is given by [18]

$$r_d = \frac{(n^2-1)\sin(\frac{2\pi}{\lambda} n L_d)}{2in\cos(\frac{2\pi}{\lambda} n L_d) + (n^2+1)\sin(\frac{2\pi}{\lambda} n L_d)}, \tag{1.44}$$

where n is the refractive index of the membrane and L_d is the thickness of the membrane. In this thesis we are discussing two SiN membranes with $n \approx 2$, one with thickness 50 nm in Chapter 2, all the other chapters are based on a membrane with

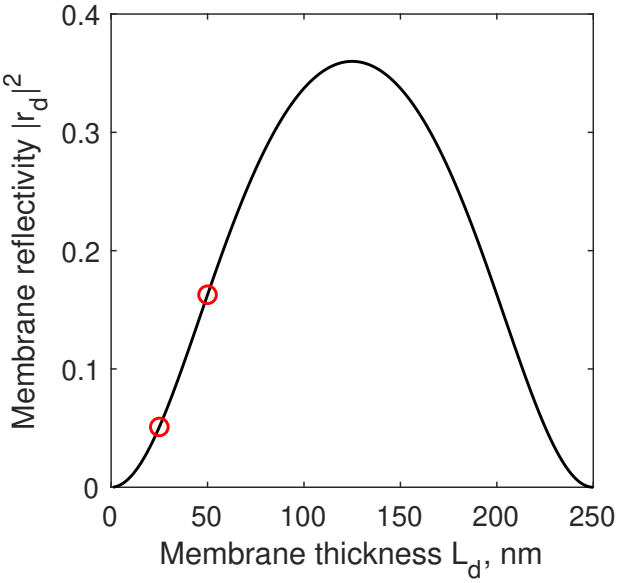

Figure 1.2: Theoretical reflectivity of a SiN membrane as a function of thickness. The red circles represent theoretical values for the two membranes used in this thesis with $L_d = 25$ nm and $L_d = 50$ nm.

thickness 25 nm. Theoretical intensity reflectivity $|r_d|^2$ is plotted in Fig. 1.2 as a function of the membrane thickness. Membrane acts as a Fabry-Perot resonator which gives rise to the shape of this curve.

Solving the boundary condition equations for the electromagnetic wave in the cavity with a membrane results in the following equation under the assumption of $\mathrm{Im}(n) = 0$ and cavity mirror reflectivities $r_m \to 1$ [18]:

$$\omega_{\mathrm{cav}}(x) = \frac{c}{L}\arccos(|r_d|\cos\frac{2\pi}{\lambda}x), \tag{1.45}$$

where c is the speed of light. Here x is a membrane shift from the cavity center on the wavelength scale. The theoretical cavity-with-membrane resonant frequency ω_{cav} is plotted in Fig. 1.3 for various membrane reflectivities.

The membrane-in-the-middle system differs from the system with one fixed mirror and one movable mirror depicted in Fig. 1.1 and it's not straightforward to see how the optomechanical coupling arises in the membrane-in-the-middle system. Generally, the intensities of light at the left membrane boundary and at the right one are different. This is true for all membrane positions except for the nodes and antinodes. The difference in the intensities gives rise to non-zero net radiation pressure and thus to optomechanical coupling. Mathematically the dependence of the cavity resonance frequency on the membrane position $\omega_{\mathrm{cav}}(x)$ as seen in Fig. 1.3 gives rise to the optomechanical coupling.

Another important difference with the system with a moving mirror is that the difference of the consecutive cavity resonance frequencies is a function of the mem-

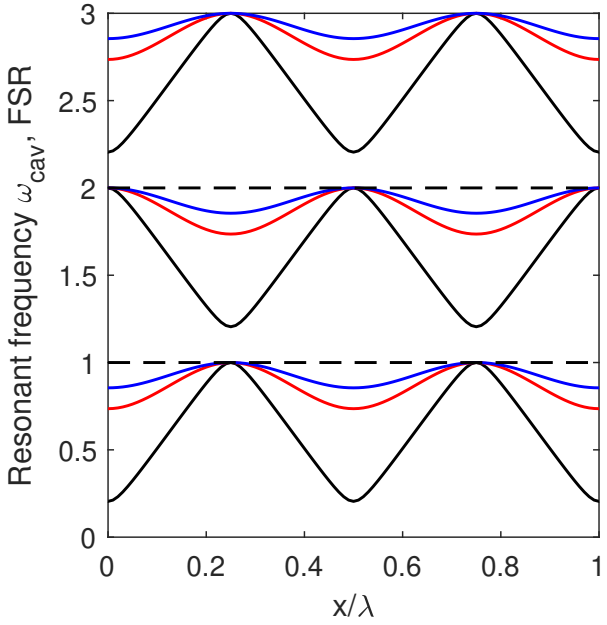

Figure 1.3: Resonant frequency of a cavity with a SiN membrane in the middle as a function of the membrane position x for different membrane reflectivities. The dashed line corresponds to $|r_d|^2 = 0$ (empty cavity), the blue line corresponds to membrane thickness $L_d = 25$ nm and $|r_d|^2 = 0.05$, red to $L_d = 50$ nm and $|r_d|^2 = 0.16$, black to $|r_d|^2 = 0.9$.

brane position while the odd or even cavity resonances have constant frequency difference which we further will call 2FSR.

2

Squeezed mechanical state

In this chapter we demonstrate strong optomechanical squeezing of a thermal state in the membrane-in-the-middle setup. Parametric modulation is used to squeeze the in-phase quadrature. The out-of-phase quadrature is restrained from diverging by a single-quadrature active feedback cooling. The parametric modulation is accomplished by modulating the detuning of a red-detuned pump light fields at twice the frequency of the mechanical mode, while the feedback cooling is provided by electrostatic forces from a sharp metallic tip in the vicinity of the mechanical mode.

This chapter is based on: S. Sonar, **V. Fedoseev**, M.J. Weaver, F. Luna, E. Vlieg, H. van der Meer, D. Bouwmeester and W. Löffler, Strong thermomechanical squeezing in a far-detuned membrane-in-the-middle system, Physical Review A 98, 013804 (2018). The experiment was performed together with Sameer Sonar.

2.1 Introduction

Non-classical states of a mechanical oscillator are of considerable interest to improve the measurement sensitivity of an optical interferometer with mirrors attached to a mechanical resonator (as needed for example for gravitational wave detectors such as LIGO and VIRGO), and for fundamental tests of quantum mechanics [19]. Here we discuss a method to produce a mechanical state where one of the motional quadratures is diminished at the expense of the other quadrature. The method is applied to a thermal state while generally it works also in the quantum regime. Methods have been proposed to generate squeezing in the classical [20, 21] and in the quantum regimes [2, 22, 23, 24, 25]. Experimental demonstrations [26, 27, 28, 29, 30] of squeezing include an observation of 4.7 dB squeezing below the zero point motion [19].

The idea of squeezing is based on a parametric oscillator, where the spring constant is modulated at twice the mechanical frequency Ω_m. Let's consider a response of such an oscillator to the in-phase excitation $f_s \sin \Omega t$ and out-of-phase excitation

$f_c \cos \Omega t$ for frequencies Ω:

$$\ddot{x} + \frac{\Omega_m}{Q}\dot{x} + \Omega_m^2(1 + \epsilon \sin 2\Omega_m t)x = f_s \sin \Omega t + f_c \cos \Omega t. \tag{2.1}$$

Let's find the steady state solution of this equation in the form

$$x = A \sin \Omega t + B \cos \Omega t \tag{2.2}$$

and in the limit of high quality factor $Q \gg 1$, where A and B are mechanical susceptibilities. Noticing that

$$\begin{aligned} \sin^2 \Omega t \cos \Omega t &= \frac{1}{4}\cos \Omega t - \frac{3}{4}\cos 3\Omega t, \\ \sin \Omega t \cos^2 \Omega t &= \frac{1}{4}\sin \Omega t + \frac{3}{4}\sin 3\Omega t \end{aligned} \tag{2.3}$$

and neglecting terms rotating at 3Ω, for $\Omega \approx \Omega_m$ we get

$$\begin{aligned} A &= \frac{Qf_c}{\Omega_m^2}\frac{1}{1+g}, \\ B &= -\frac{Qf_s}{\Omega_m^2}\frac{1}{1-g}, \end{aligned} \tag{2.4}$$

where we introduced gain $g = \frac{\epsilon Q}{2}$. Therefore, in the presence of the parametric modulation the response of the oscillator depends on the phase of the modulation relative to the excitation force acting on the oscillator. Significantly, in the presence of the in-phase excitation and $g > 1$ the motion of the oscillator becomes unstable: the amplitude of motion grows exponentially with time. If $g < 1$, a steady state solution exists with different susceptibilities A and B.

Now, extending this analysis to the case of a mechanical oscillator excited by thermal forces, we get the variances of the oscillator quadratures of motion $x(t) = X_2(t) \sin \Omega_m t + X_1(t) \cos \Omega_m t$ [31, 9]:

$$\begin{aligned} \langle X_2^2 \rangle &= \frac{k_B T}{m_{\text{eff}} \Omega_m}\frac{1}{1+g}, \\ \langle X_1^2 \rangle &= \frac{k_B T}{m_{\text{eff}} \Omega_m}\frac{1}{1-g}, \end{aligned} \tag{2.5}$$

where m_{eff} is the effective mass of the oscillator, T is its temperature. In the absence of the modulation $g = 0$ the oscillator is in a thermal state with equal quadrature variances

$$\sigma_0 = \langle X_1^2 \rangle = \langle X_2^2 \rangle = \frac{k_B T}{m_{\text{eff}} \Omega_m}. \tag{2.6}$$

It can be seen that modulating the oscillator with $g < 1$ the thermal state becomes squeezed. Maximal squeezing is achieved when $g \to 1$: in this case $\langle X_2^2 \rangle \to +\sigma_0^2/2$ and $\langle X_1^2 \rangle \to \infty$.

Thus parametric modulation squeezing is limited to $1/2$ or ~ 3 dB. This limit is not universal, it can be overcome by cooling the diverging quadrature. In this

approach g may become larger than 1. This was demonstrated experimentally using active feedback on the diverging quadrature [31, 32].

How can parametric modulation be achieved in an optomechanical system? The intracavity light fields modify the spring constant and the damping rate of an optomechanically coupled oscillator via the optical spring effect. This effect can be used to modulate the overall spring constant of an oscillator and perform the parametric modulation. The optical spring effect is a function of the light fields detuning $\Delta = \omega_L - \omega_{\mathrm{cav}}$. If the detuning is modulated at twice the mechanical frequency, then the frequency of the mechanical mode is also modulated at twice the mechanical frequency. This approach was demonstrated in a sideband-unresolved system [33] by modulation of the pump light fields detuning. Here we demonstrate 8.5 dB squeezing of a mechanical state using the same technique but in a sideband-resolved regime.

The remainder of this chapter is structured as follows. First we describe our setup, the realization of the parametric modulation and active feedback cooling. Next we show the experimental results of the parametric modulation only. Finally we stabilize the diverging quadrature and show a beyond 3 dB squeezing.

2.2 Setup

Our setup consists of a high mechanical quality transparent membrane placed in the middle of a high-finesse 98 mm optical cavity. The membrane is a high-stress (1 GPa) Si_3N_4 50 nm thick membrane attached to a silicon chip available commercially from NORCADA Inc, see Fig. 2.1. A sharp metallic tip is positioned in the vicinity of the membrane. Generally, there are charges on the membrane, application of a voltage to the tip induces a force on the membrane. The cavity consists of two DBR mirrors with 10 ppm transmission (specs) from Laseroptik GmbH implying optical finesse of 3×10^5, but optical ringdown measurements showed finesse of 6×10^4 and much smaller than expected transmission consistent with 40 ppm of absorption. This can be explained by dust particles visible by naked eye in the mirror holding box as delivered from the company. The mirrors were cleaned by blowing clean He gas. Insertion of the membrane in the cavity reduced the optical finesse further to 3.3×10^4. The setup is placed in a room temperature vacuum chamber pumped by an ion pump to pressure of $\sim 10^{-6}$ mbar. The membrane holder can be tip-tilted in situ by three rotary piezo stick-slip motors with a step size of about 20 nm, see Fig. 2.2. The motors are used to maximize the transmission signal and membrane positioning.

The membrane is positioned ~ 30 μm from the exact center along the optical axis of the cavity by measuring the 2FSR value. The detailed description can be found in the next chapter.

We performed experiments with the fundamental vibrational mode of the membrane having resonance frequency $\Omega_m = 385$ kHz, effective mass $m_{\mathrm{eff}} = 30$ ng and mechanical quality factor $Q = 3 \times 10^5$, further called mechanical mode.

The optical setup is shown in figure 2.3. A weak probe laser (10 μW) is used to trace the resonance of the cavity via the Pound-Drever-Hall locking technique

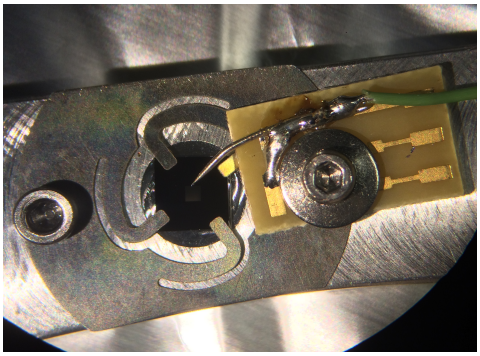

Figure 2.1: Photo of the membrane on a sample holder. The sharp tip does not touch the membrane.

(PDH) [34]. To accomplish this the probe laser light goes through an electro-optical modulator (EOM) modulated at 9.5 MHz. The light back-reflected from the cavity is detected by a photodetector and its signal is demodulated at 9.5 MHz to get the PDH error signal. This error signal is sent to a proportional-integral-differential controller (PID) providing feedback to the probe laser. The feedback bandwidth is much smaller than Ω_m. The PDH error signal is also demodulated at Ω_m to get the two motional quadratures $X_1(t)$ and $X_2(t)$ of the mechanical mode.

A strong pump laser is used to modulate the frequency of the mechanical mode by dynamic backaction. The optical fields back-reflected from the optical cavity are directed towards detectors using an optical circulator. The pump and probe fields are separated by a polarizing beam splitter (PBS). To decrease possible interference effects at the detectors even further, different cavity resonances are used for the probe and pump lasers. The pump laser is locked to the probe laser with a frequency difference ~ 3 GHz by a phase-locked-loop: the light from both lasers interferes on a fast photodiode which produces a beat electronic signal, see Fig. 2.4. This beat signal is mixed with a reference radio-frequency (RF) signal produced by a signal generator and sent to a low pass filter. The resulting signal is sent to a PID controller which provides feedback to the pump laser maintaining the frequency difference of the lasers equal to the RF signal frequency. This frequency difference is set to 2FSR + Δ, where Δ is the required detuning of the pump laser from the cavity resonance. We chose 2FSR because the consecutive resonance frequency difference 1FSR is a function of the membrane position x (see Fig. 1.3 from Chapter 1), while 2FSR is not in the case when the membrane is exactly in the middle of the cavity. The pump frequency detuning Δ is modulated at $2\Omega_m$ using a signal $\propto \sin(2\Omega_m t + \phi)$, this signal is added to the pump feedback signal. The feedback bandwidth of the phase-locked-loop is much smaller than $2\Omega_m$ and thus the added modulation does not affect the frequency locking between the lasers. The phase ϕ is adjusted to align the squeezing axis such that X_2 quadrature is squeezed.

A change in the detuning of the pump laser Δ with fixed light intensity outside the cavity leads also to a change in the effective quality factor of the oscillator. Figure 2.5 shows the measured frequency shift $\delta\Omega_m$ and the effective damping

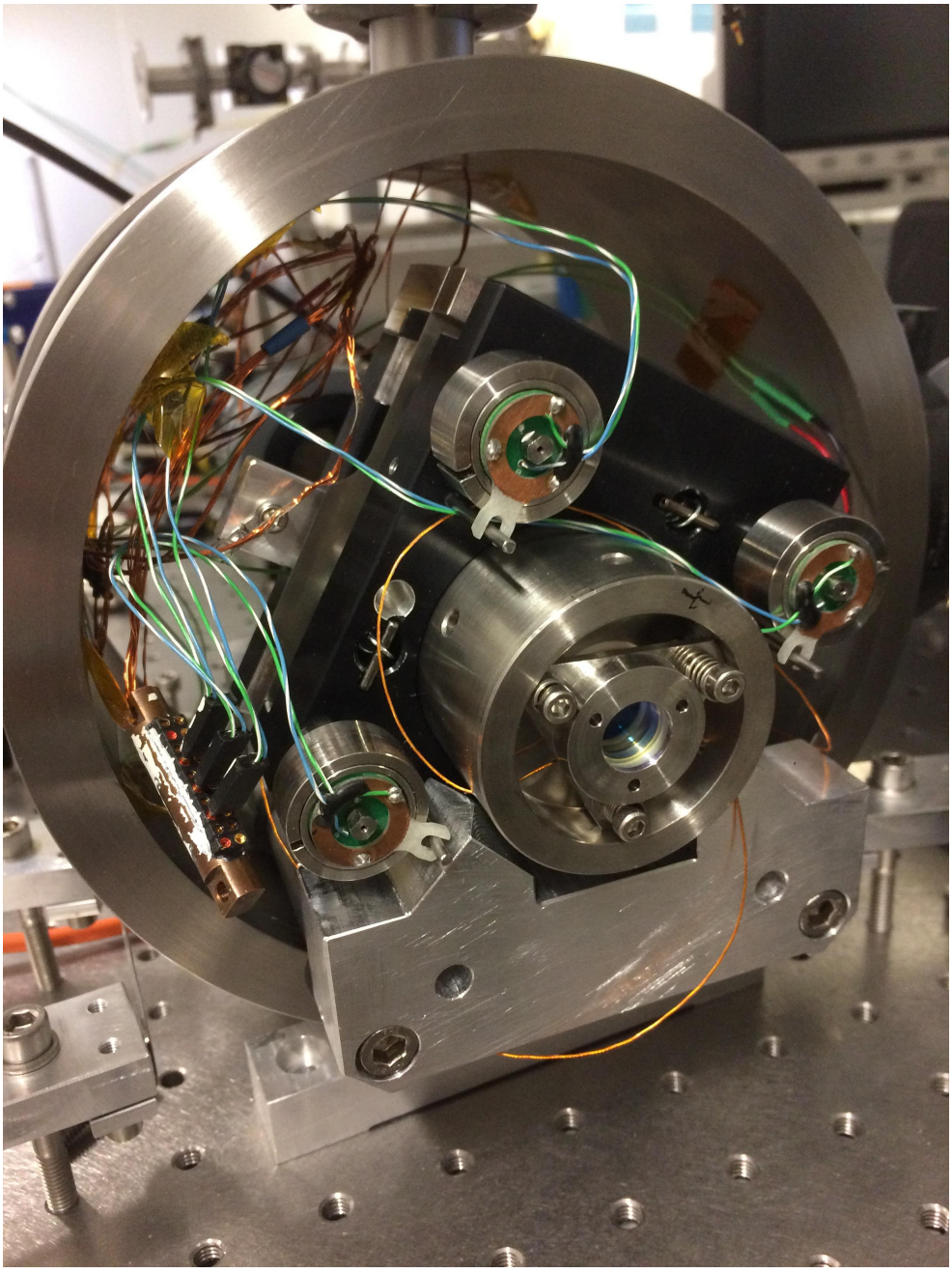

Figure 2.2: Setup in a room temperature vacuum chamber. The first cavity mirror is visible pressed against the Invar body. The sample holder is mounted on a motorized tip-tilt stage (black).

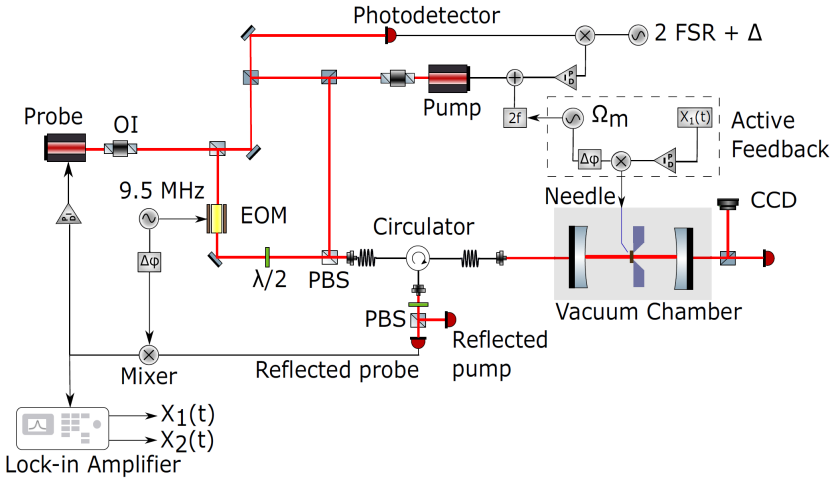

Figure 2.3: Optical setup.

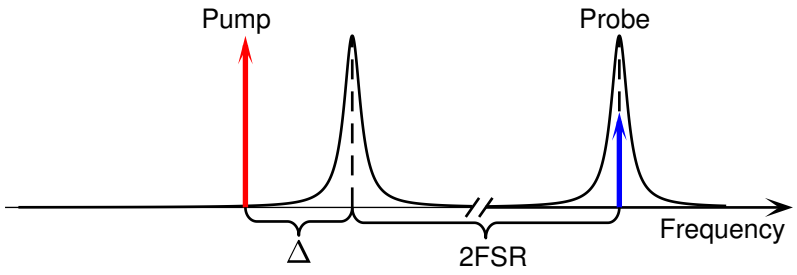

Figure 2.4: The probe and pump laser frequencies.

$\Gamma_{\text{eff}} = \Omega_m/Q + \Gamma_{\text{opt}}$, where Γ_{opt} is the optical damping due to dynamic backaction in a detuning Δ sweep. Note, the intracavity light intensity also changes when the detuning is changed. $\delta\Omega_m$ and Γ_{eff} were extracted from fitting the noise spectrum of the mechanical mode. We highlight three different detuning regions in this plot where the slope of the frequency shift is much larger than the slope of the damping curve as required by our model Eq. 2.1. Region I was hard to realize for our system because due to fluctuations in the detuning the detuning occasionally becomes positive and the lock of the probe laser is lost. In region II the second derivative of the frequency shift is significant which makes the modulation non-linear. Region III where $\Delta = -1.43\Omega_m$ is most practical due to stability considerations of our system.

In the case of an ideal membrane the modulation of the intracavity light intensity at $2\Omega_m$ should excite the 2,2 vibrational mode. For our membrane the frequency of the 2,2 mode is however a few hundred Hertz away from $2\Omega_m$, so this mode is not excited due to the parametric modulation.

Figure 2.6 shows phase-space trajectories under different conditions. Figure 2.6(a)

shows a thermal state with effective temperature $T = 120$ K when the pump light is on and is not modulated, providing a weak cooling effect only. When the pump modulation is on, the X_2 quadrature becomes squeezed and the X_1 quadrature becomes enhanced, Fig. 2.6(b). When the modulation strength is increased even further to surpass the limit $g = 1$, the motion becomes bi-stable probably due to non-linear mechanical effects in the membrane, Fig. 2.6(c) and 2.6(d).

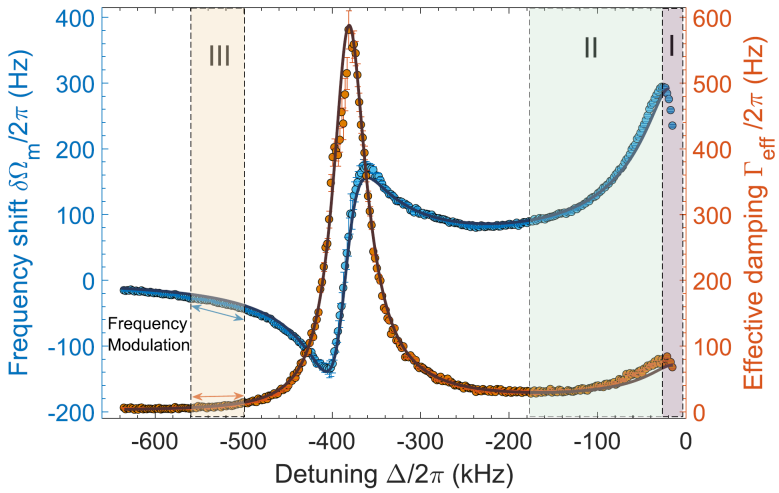

Figure 2.5: Optical spring effect as a function of the pump detuning Δ showing three regions I, II and III where frequency modulation can be realized.

2.3 Active feedback

To achieve stronger squeezing we applied active feedback to cool the diverging mode X_1 only.

The mechanical mode can be cooled by applying active feedback via the introduction of a viscose damping force $f \propto -\dot{x}$ [9]. In the limit of a high-Q oscillator

$$\begin{aligned} x(t) &= X_2(t)\sin\Omega_m t + X_1(t)\cos\Omega_m t, \\ \dot{x}(t) &\approx \Omega_m X_2(t)\cos\Omega_m t - \Omega_m X_1(t)\sin\Omega_m t, \\ \dot{x}(t) &\approx \Omega_m x(t + \frac{\pi}{2\Omega_m}) \approx -\Omega_m x(t - \frac{\pi}{2\Omega_m}), \end{aligned} \tag{2.7}$$

where we neglected the terms proportional to $\dot{X}_1$ and $\dot{X}_2$. Thus by measuring $x(t)$ and applying a force proportional to the measured value with a fixed delay of one quarter of the mechanical period the mechanical mode can be cooled. Both quadratures are cooled equally. To cool $X_1(t)$ only the following feedback force should be applied:

$$f \propto X_1(t)\sin\Omega_m t. \tag{2.8}$$

For this purpose we applied a voltage signal to the sharp metal tip in the vicinity of the membrane in the form $V(t) \propto X_1(t) \sin \Omega_m t$. To realize this experimentally one of the measured quadratures is mixed with the local oscillator Ω_m and after amplification it's sent to the sharp metal tip. In this case the variance of the quadratures of a mechanical mode driven by thermal motion and parametric modulation is modified in the following way [31]:

$$\begin{aligned} \langle X_2^2 \rangle &= \frac{k_B T}{m_{\text{eff}} \Omega_m} \frac{1}{1+g}, \\ \langle X_1^2 \rangle &= \frac{k_B T}{m_{\text{eff}} \Omega_m} \frac{1}{1-g+h}, \end{aligned} \tag{2.9}$$

where h is proportional to the strength of the feedback. We see that the variance of X_2 stays unchanged. Now, the 3 dB limit can be surpassed by increasing g above unity while keeping $1 - g + h > 0$.

Figure 2.7 shows squeezing results for different feedback strengths h. The variances are normalized against the case of $g = 0$ and $h = 0$ but with the pump light on, resulting in an effective temperature $T_{\text{eff}} = 120$ K.

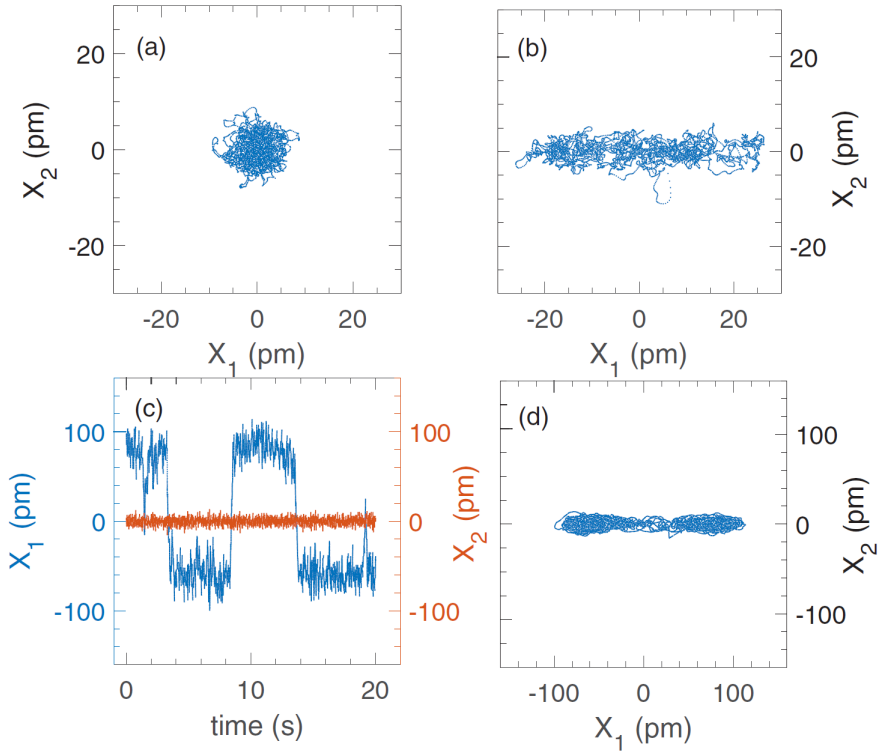

Figure 2.6: Quadratures X_1 and X_2 evolution for (a) thermal state; (b) squeezed state for parametric modulation with $g < 1$; (c) and (d) parametric modulation with $g > 1$.

The first measurement was done without any feedback ($h = 0$), the results are

shown with diamonds. A maximum squeezing of 3 dB was achieved.

The second measurement run was done with feedback strength equivalent to $h = 2.9$. A maximum squeezing of 7 dB was achieved.

In the third measurement run the intensity of the pump laser light was decreased. The effective temperature was measured to be 182 K with the pump light on. Using the feedback strength of $h = 21.5$, a maximum squeezing of 8.5 dB was achieved. For high values of gain g the experimentally measured squeezing starts to deviate from the theoretical predictions. Some assumptions of our model are not fulfilled in this regime, for example the quadratures are not independent any more or some linearity conditions are violated. Another possible reason is that the modulation of the pump laser light leads to a sideband with detuning $-1.43\Omega_m + 2\Omega_m = 0.57\Omega_m$. This sideband is blue-detuned and heats both quadratures. This can be avoided if the detuning $\Delta < -2\Omega_m$.

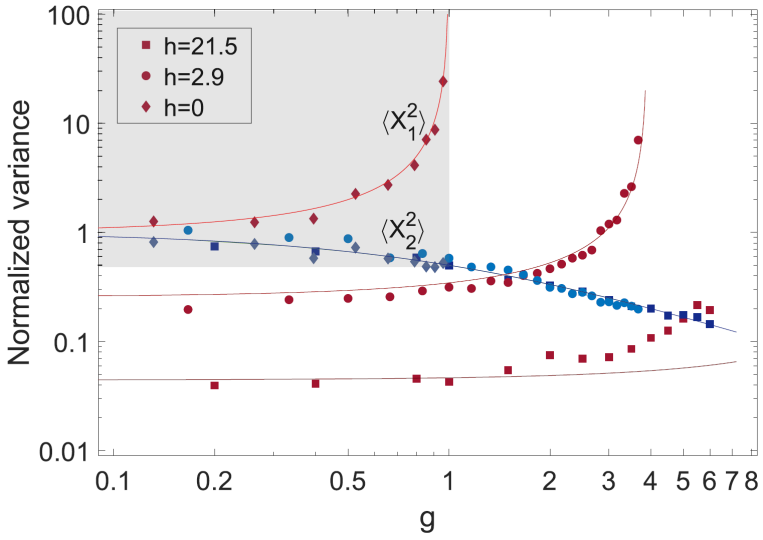

Figure 2.7: Normalized variance of X_1 (red) and X_2 (blue) as a function of parametric modulation g for $h = 0$ (diamonds), $h = 2.9$ (circles), $h = 21.5$ (squares).

2.4 Discussion

Let's consider the final state achieved with highest gain $g = 6$ and feedback strength $h = 21.5$. It has approximately equal quadrature variances for X_1 and X_2, see Fig. 2.7. Generally speaking, it can be achieved just by sideband cooling without any feedback or parametric modulation. Another thing to note is that when $g = 21.5$ and $h = 0$ (strongest feedback and no parametric modulation) the achievable state is squeezed 14 dB, which is more than the maximum squeezing reported here (8.5 dB) due to the parametric modulation. However, it is worth to note that the squeezing due to parametric modulation is in principle noiseless [31], while to achieve

a quantum squeezed state via the single quadrature feedback, strong backaction-evading quantum-limited measurement of the single quadrature would be required. Such a measurement does not introduce any noise due to backaction into the measured quadrature (all the noise goes to the other quadrature [9]) and as the measured quadrature can be measured to an arbitrary precision, this quadrature becomes squeezed just by the measurement.

A limitation of a sideband-resolved system as used here is that active feedback becomes less efficient as the mechanical mode makes many oscillations within the time of light leakage from the cavity $1/\kappa$.

2.5 Conclusions

We demonstrated strong squeezing of a mechanical thermal state via parametric modulation of the effective spring constant of the mechanical mode. Single quadrature feedback was essential to achieve beyond 3 dB squeezing for high-gain modulation, which restrains the non-squeezed quadrature from unconstrained growth. The modulation is achieved by frequency modulation of a red-detuned pump, while the feedback force is generated by electrostatic forces exerted on the membrane from a sharp metallic tip.

This method can be also applied in the quantum regime to squeeze one of the quadrature of a mechanical mode below the vacuum noise level. This will increase the sensitivity of position measurements of a mechanical oscillator, and will allow for a study of decoherence and the corresponding evolution of quantum systems into classical ones [35].

Acknowledgements

The results in this chapter are part of the M.Sc. thesis of S. Sonar. The research was conducted together with and under the daily supervision of Vitaly Fedoseev. Figures 2.3, 2.5, 2.6 and 2.7 were prepared by S. Sonar.

3

STIRAP of a classical state

In multimode optomechanical systems, the mechanical modes can be coupled via the radiation pressure of the common optical mode, but the fidelity of the state transfer is limited by the optical cavity decay. In this chapter we demonstrate stimulated Raman adiabatic passage (STIRAP) in optomechanics, where the optical mode is not populated during the coherent state transfer between the mechanical modes. Therefore the optical decay channel is avoided. We show a state transfer of a coherent mechanical excitation between vibrational modes of a membrane in a high-finesse optical cavity with a transfer efficiency of 86%. Combined with exceptionally high mechanical quality factors, STIRAP between mechanical modes can enable generation, storage and manipulation of long-lived mechanical quantum states, which is important for quantum information science and for the investigation of macroscopic quantum superpositions.

This chapter is based on: **V. Fedoseev**, F. Luna, I. Hedgepeth, W. Löffler and D. Bouwmeester, Stimulated Raman Adiabatic Passage in Optomechanics, Phys. Rev. Lett. 126, 113601 (2021).

3.1 Introduction

STIRAP describes adiabatic population transfer between two states coherently coupled via a mediating state that remains unoccupied. This renders STIRAP robust against loss and noise in the mediating state, leading to profound applications in atomic- and molecular-optics research [16, 36], trapped-ion physics [37], superconducting circuits [38], other solid-state systems [39, 40], optics [41], in entanglement generation [42, 43] and qubit operations [44]. STIRAP in optomechanics has been proposed for optical frequency conversion with a mechanical mode being the mediating state, where the fidelity of the state transfer is not deteriorated by the residual thermal noise of the mechanical mode [45, 46], and for a mechanical state transfer through the common optical mode [47].

In a theory paper [48] a method was proposed to create an indirect coupling

between non-degenerate mechanical modes via a common optical mode. In this scheme the coupling is created by two stationary red-detuned pump light fields. Experimentally the coupling was observed in an electromechanical system via splitting of the hybridized mechanical peaks in the avoided level crossing [49]. The same indirect coupling can be seen in the energy transfer between two mechanical modes. Such a transfer between the two non-degenerate mechanical modes was demonstrated in [12, 15] where the beating between two driving light fields bridges the frequency difference of the modes. The motion of the modes modulate the intracavity light fields creating motional sidebands [9]. This transfer scheme relies on the matched motional sidebands and requires the detuning of the driving fields to be much higher than the mechanical frequencies [48]. In this case the other unmatched motional sidebands are of similar amplitudes as the matched ones and cause incoherent driving or cooling of the mechanical modes, limiting the state transfer fidelity. In optomechanical STIRAP in the sideband-resolved regime the loss due to the unmatched motional sidebands can be made negligibly small by choosing the detuning of the two driving light fields equal to the frequencies of the mechanical modes. In this case the two matched sidebands at the cavity resonance interfere destructively driving the state transfer. The other motional sidebands have much smaller amplitudes. This strongly decreases the unwanted effects of the unmatched motional sidebands and allows the state transfer fidelity to approach unity in the quantum regime. Such a state transfer is equivalent to the π-pulse (π rotation on the Bloch-sphere in the vertical plane). Via a specific modification of the STIRAP driving pulses a $\pi/2$-pulse can be achieved resulting in a fully entangled state. In spite of the two red-detuned pumps no energy is lost to the environment from the mechanical modes in a STIRAP transfer with the adiabaticity condition fulfilled.

An indirect cavity-mediated coupling can also be created via one red-detuned pump and one blue-detuned pump with detunings equal to the corresponding frequencies of the mechanical modes. Such a scheme was realized in electro-mechanical systems in the quantum regime [50, 51, 52]. The coupling resulted in an entanglement of the two mechanical oscillators. In this scheme the state of the mechanical mode corresponding to the red-detuned pump (mode 1) is transferred to the other mechanical mode (mode 2) similar to the two red-detuned pumps scheme. But, in addition, mode 2 is being driven incoherently by the blue-detuned pump and a fully entangled state cannot be achieved.

Fig. 3.1(a) shows the basic Λ-type arrangement of 3 levels typical for STIRAP. In the triply rotating frame at frequencies $\omega_i = E_i/\hbar$ for states ψ_i, $i = 1, 2, 3$, the Hamiltonian is:

$$\hat{H}(t) = \frac{\hbar}{2}\begin{pmatrix} 0 & \Omega_{12}(t) & 0 \\ \Omega_{12}(t) & 0 & \Omega_{23}(t) \\ 0 & \Omega_{23}(t) & 0 \end{pmatrix}, \tag{3.1}$$

with Ω_{12} and Ω_{23} the Rabi frequencies resulting from two driving fields at frequencies $(E_2 - E_1)/\hbar$ and $(E_2 - E_3)/\hbar$. One of the three instantaneous eigenstates has eigenvalue 0 and does only include states ψ_1 and ψ_3:

$$\Phi_0(t) = \cos\theta(t)\psi_1 - \sin\theta(t)\psi_3, \tag{3.2}$$

with $\tan\theta(t) = \Omega_{12}(t)/\Omega_{23}(t)$. The existence of this "dark" state in optomechanics

has been firstly demonstrated in [53]. STIRAP is based on the adiabatic following of $\Phi_0(t)$ by slowly varying $\theta(t)$ from $\theta(-\infty) = 0$ to $\theta(\infty) = \pi/2$. Thus, the system can be adiabatically transferred from ψ_1 to ψ_3, never occupying state ψ_2. Fig. 3.1(b) shows a driving pulse sequence satisfying this requirement and Fig. 3.1(c) shows the energy eigenvalues corresponding to the three eigenstates $\Phi_+(t)$, $\Phi_0(t)$, and $\Phi_-(t)$. This driving pulse sequence together with the adiabaticity condition $\sqrt{\Omega_{12}(t)^2 + \Omega_{23}(t)^2} \gg \dot{\theta}$ prevents the lossy mediating state from being occupied throughout the transfer process.

The Hamiltonian in Eq. (3.1) can be realized in multimode optomechanics [45, 46] where states 1 and 3 are mechanical excitations with frequencies ω_1 and ω_2 and state 2 is an optical cavity mode at $\omega_{\rm cav}$, see Fig. 3.1(d). Two optical driving fields at $\omega_{{\rm L}i} = \omega_{\rm cav} - \omega_i$ for $i = 1, 2$ are introduced in order to create the beamsplitter interaction $\hat{a}\hat{b}_i^\dagger + \hat{a}^\dagger\hat{b}_i$ that couples the mechanical modes to the cavity mode, where $\hat{a}(\hat{a}^\dagger)$ and $\hat{b}_i(\hat{b}_i^\dagger)$ are the photon and phonon annihilation (creation) operators.

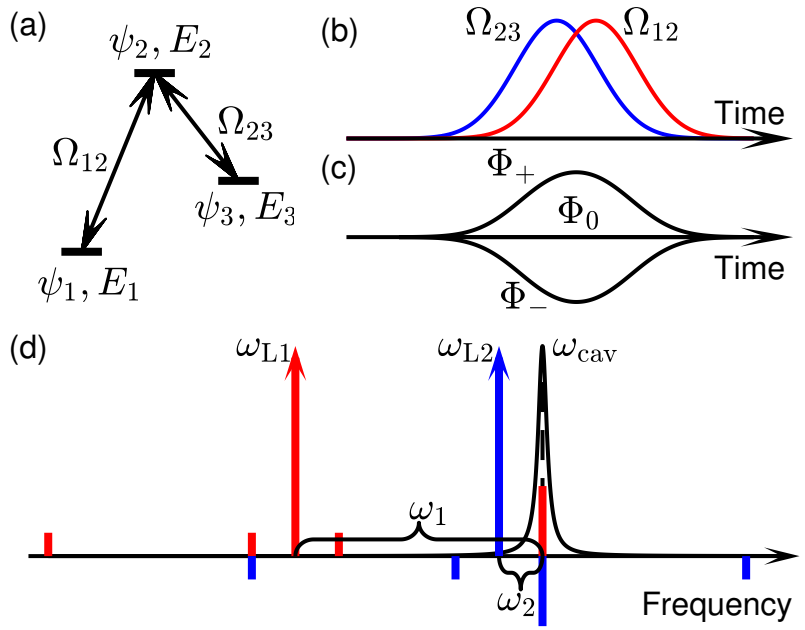

Figure 3.1: STIRAP scheme in optomechanics. (a) Energy levels diagram. (b) Coupling strengths of the pulse sequence for the driving fields. (c) The resulting energy eigenvalues for the instantaneous Hamiltonian eigenstates. STIRAP explores the properties of $\Phi_0(t)$ given in Eq. (3.2). (d) The optomechanical implementation contains a cavity mode at frequency $\omega_{\rm cav}$, two driving fields at $\omega_{\rm L1}$ and $\omega_{\rm L2}$ and eight motional sidebands due to the mechanical modes at ω_1 and ω_2 on the driving fields, red bars corresponding to the sidebands on $\omega_{\rm L1}$ and blue bars corresponding to the sidebands on $\omega_{\rm L2}$. Two sidebands match $\omega_{\rm cav}$. In the case of $\Phi_0(t)$ the states ψ_1 and ψ_3 are out of phase leading to destructive interference of the sidebands that overlap with $\omega_{\rm cav}$.

The optical mode can be represented by the operator $\hat{a} = \bar{\alpha} + \delta\hat{a}$, where $\bar{\alpha}$ is the

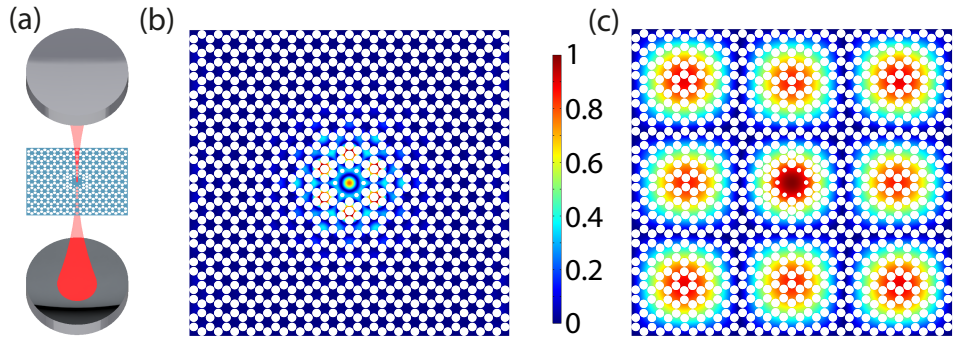

Figure 3.2: Optomechanical setup. (a) A transparent dielectric membrane patterned with a phononic crystal is placed in the middle of a high-finesse optical cavity. Shift of the membrane along the axis of the cavity changes the cavity resonance frequency, causing coupling of light in the cavity to vibrational modes of the membrane. (b) Simulated displacement of a mechanical mode of the defect of the phononic crystal. The mode is localized as its frequency lies in the band gap (mode 1, initially excited). (c) Simulated displacement of the 3,3 drumhead mode of the full membrane (mode 2). This second mode was selected because it has an appropriate mechanical frequency and quality factor and has a maximum amplitude at the center. This allows both modes to be aligned for optimal coupling to the same cavity mode.

average coherent amplitude due to the driving optical fields and $\delta\hat{a}$ is the fluctuating term [9]. Each mechanical mode produces two sidebands on each optical field. Due to resonance with the cavity the two sidebands with frequencies ω_{cav} acquire much larger amplitudes than the other sidebands. Taking into account only those two sidebands and including mechanical and optical loss rates, Γ_i and κ, the time evolution of the state vector $\psi(t) = (\hat{b}_1(t), \delta\hat{a}(t), \hat{b}_2(t))^T$ is given by

$$i\frac{d\psi(t)}{dt} = \begin{pmatrix} -i\frac{\Gamma_1}{2} & g_1(t) & 0 \\ g_1(t) & -i\frac{\kappa}{2} & g_2(t) \\ 0 & g_2(t) & -i\frac{\Gamma_2}{2} \end{pmatrix} \psi(t). \tag{3.3}$$

Here, the rotating wave approximation has been used and it is valid in the linearized regime of cavity optomechanics [9]. $g_i(t)$ is the optomechanical multiphoton coupling for mechanical modes $i = 1, 2$, $g_i = g_{i0}\bar{\alpha}_i$, where g_{i0} is single photon coupling and $\bar{\alpha}_i$ is the driving field at $\omega_{\mathrm{L}i}$, see section Theory. Equation (3.3) is valid in the sideband resolved regime together with the requirement $|\omega_1 - \omega_2| \gg \kappa$ and is identical to Eq. (3.1) in the absence of losses and with the Rabi frequencies Ω_{12} and Ω_{23} corresponding to $2g_1$ and $2g_2$.

Experimentally we demonstrate the state transfer in the membrane-in-the-middle (MIM) configuration [54], where a membrane with low optical absorption is placed in the center of a high-finesse optical cavity with $\kappa/2\pi = 54$ kHz (including membrane), see Fig. 3.2. A displacement of the membrane along the optical axis leads to a shift in the optical cavity transmission described by the interaction Hamiltonian $\hat{H}_{int} = -\hbar g_0 \hat{a}^\dagger \hat{a}(\hat{b} + \hat{b}^\dagger)$, where g_0 is the single photon optomechanical coupling [9]. The membrane is a highly stressed 25 nm thick SiN film lithographically patterned

with a phononic crystal with a defect in its center suspended on a silicon frame [7]. There are two types of mechanical modes: whole membrane drumhead modes and modes localized near the phononic crystal defect with frequencies in the phononic crystal bandgap. Vibrational energy of the drumhead modes is mainly lost in the bending regions where the membrane is connected to the frame [55, 7]. The modes localized near the defect possess enhanced quality factors by 1-2 orders of magnitude compared to the drumhead modes [7]. We demonstrate STIRAP between the fundamental mode of the defect with frequency $\omega_1/2\pi = 1.25$ MHz and quality factor $Q = 1.3 \cdot 10^7$ (mode 1, Fig. 3.2(b)), and the 3,3 drumhead mode with $\omega_2/2\pi = 0.22$ MHz and $Q = 1.2 \cdot 10^6$ (mode 2, Fig. 3.2(c)). The modes are coupled to the optical cavity with single-photon couplings of $g_{01}/2\pi = 1.5 \pm 0.1$ Hz and $g_{02}/2\pi = 1.0 \pm 0.1$ Hz respectively. In addition to these modes possessing relatively large single photon coupling, quality factors and frequency separation, there are no other mechanical modes in the range of $\sim 1/\sigma$ from ω_1 and ω_2, where σ defines the width of the driving pulses. The latter requirement guaranties that modes 1 and 2 are not coupled to other modes during the transfer. STIRAP is very sensitive to the double-photon detuning $\Delta_{2\mathrm{ph}} = (\omega_{\mathrm{L1}} + \omega_1) - (\omega_{\mathrm{L2}} + \omega_2)$ [13], therefore the two optical fields are created by amplitude modulation of light from a single 1064 nm laser using acousto-optic modulator (AOM). As a result the laser phase noise is not limiting the transfer efficiency [56]. Due to nonlinear response of the AOM the detuning of this single laser light tone is chosen such that harmonics of the AC voltage sent to the AOM have a negligible effect on the transfer efficiency (see section Generation of driving pulses). The membrane is in a vacuum chamber with pressure below 10^{-6} mbar at room temperature.

3.2 Experimental details

3.2.1 Setup

The motion of the membrane is read out via the light fields generated by a probe laser at ω_{probe} (10 μW) locked to the transmission resonance frequency of the optical cavity via the Pound-Drever-Hall technique (PDH) [34]. In order to measure the instantaneous oscillation displacement of a mechanical mode ω, the reflection signal is demodulated at $\omega + \omega_{\mathrm{EOM}}$, where $\omega_{\mathrm{EOM}} = 10$ MHz is the detuning frequency of the sidebands in the PDH locking scheme. The driving light fields generated by the pump laser at ω_{pump} is locked to the probe laser by a phase-locked loop, see Fig. 3.3. The light fields from the two lasers are measured by a fast photodetector and the beating signal is mixed with a reference microwave signal, supplied by an RF generator. The resulting signal is sent to a proportional-integral-differential controller (PID) which adjusts the frequency of the pump laser. The difference between the lasers frequencies is kept at $\omega_{\mathrm{probe}} - \omega_{\mathrm{pump}} = 2\mathrm{FSR} + \Delta \sim 3$ GHz because the dispersion curves of membrane-in-the-middle systems are parallel for all odd and all even resonances [18]. This ensures a well-defined cavity resonance detuning of the pump laser in spite of drifts in the membrane position along the optical axis (~ 10 nm/hour). The pump light fields have orthogonal polarization to the probe light fields in order to minimize interference of both fields at the reflection photodetector.

To excite a membrane mechanical mode, an AC voltage (~ 10 mV) at its mechanical frequency is applied to a needle placed close to the defect of the membrane (~ 0.5 mm). The full membrane 1,1 mechanical mode thermal motion is damped by applying an electrostatic force through the needle. The force is proportional to the instantaneous position of this mode but delayed by a quarter of its oscillation, which effectively creates a frictional force proportional to the mode's velocity.

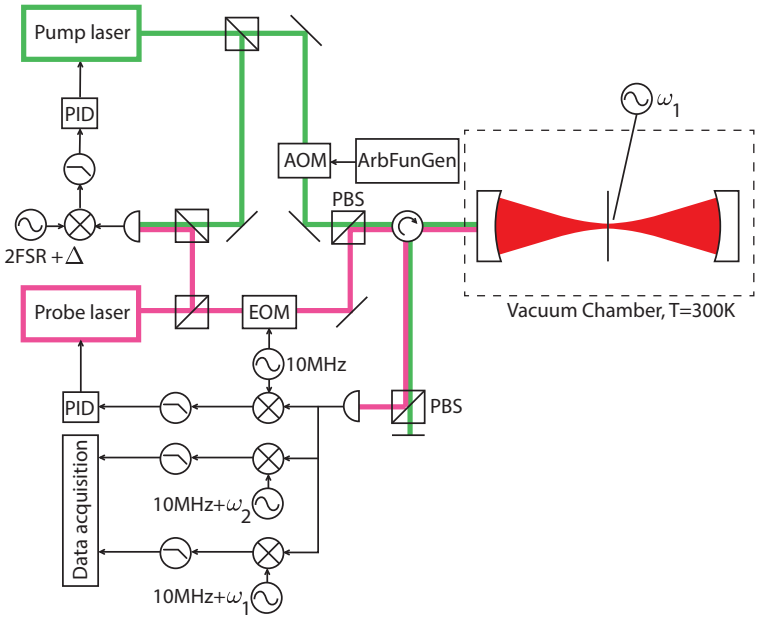

Figure 3.3: Optical setup. The probe laser is locked to the transmission peak of the cavity. The pump laser is locked to the probe laser with frequency difference $\omega_{\mathrm{probe}} - \omega_{\mathrm{pump}} = 2\mathrm{FSR} + \Delta$, controlled by an RF source. The driving pulses are shaped by electronic pulses sent to the AOM from an arbitrary wave function generator (ArbFunGen). Polarizing beam splitters (PBS) are used to separate the probe and pump light fields. Mechanical modes are excited by a needle placed close to the membrane defect.

3.2.2 Membrane positioning

The dispersion curves of a membrane-in-the-middle system are parallel for the curves separated by 2FSR provided the membrane is positioned exactly in the middle of the cavity. For a small displacement z of the membrane from the center, the free-spectral range changes as $2\mathrm{FSR} - 2\mathrm{FSR}_{\mathrm{middle}} \propto 2\mathrm{FSR}_{\mathrm{middle}} \frac{z}{L} \sin \pi \frac{z}{\lambda}$, where L is the length of the cavity and λ is the wavelength. The membrane holder is mounted on a tip-tilt stage with 3 vacuum compatible motors (1 step ~ 20 nm). To minimize the influence of the membrane drift along the optical axis, the membrane was moved towards the middle of the cavity to $z \sim 30$ μm by measuring 2FSR as a function of z, which

provides an estimate for the direction and amplitude of the movement. To further minimize the influence of membrane drifts, we use a piezo element to bring the membrane to the position where 2FSR has a local maximum as a function z. This position coincides with the maximum optomechanical coupling strength. As a result an average drift of the membrane during a measurement run of 1 hour causes an acceptable change of 2FSR ~ 5 kHz. When the actual experiment is running, we use the piezo to bring the membrane back to the position of maximum 2FSR every hour.

3.2.3 Membrane fabrication

We begin the fabrication process of the devices with a commercially supplied $525\ \mu\mathrm{m}$ thick silicon wafer coated on both sides with 25 nm of LPCVD high-stress silicon nitride. We pattern the phononic crystal structure into the nitride on one side through the use of standard photolithography. During a second photolithography step, we use an IR contact aligner to pattern a square hole in photoresist on the opposite side of the chip. A subsequent Bosch etch step etches through the exposed nitride and removes about $425\ \mu\mathrm{m}$ of the silicon underneath the phononic crystal. After cleaning the chip in piranha solution, we release the phononic crystal membrane by wet etching the remaining $100\ \mu\mathrm{m}$ of silicon using KOH at $80°$C. We perform a final clean by submerging the chip in HF for 1 minute and then we extract it out of IPA and allow it to dry through evaporation.

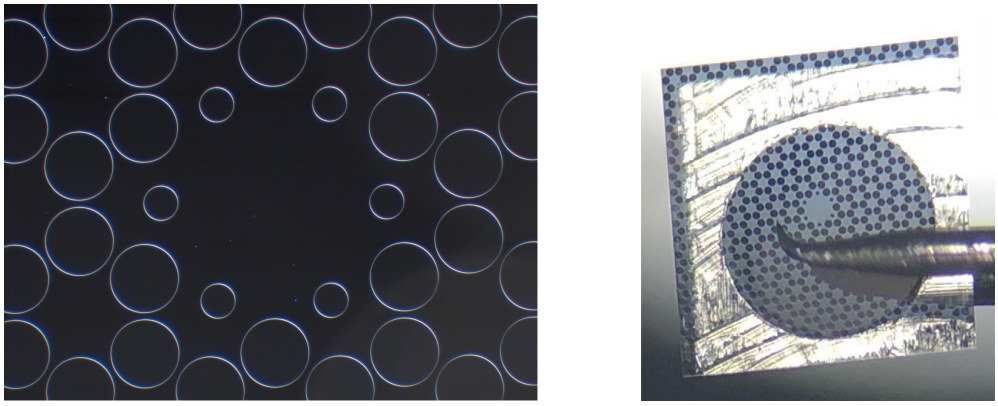

Figure 3.4: Photos of the membrane. The left photo is the dark field imaging, any particle on the membrane is visible as a bright spot. The right photo shows the device on a metallic holder. The sharp metallic tip for driving via electrostatic forces is also visible in the front.

3.2.4 Generation of driving pulses

Fluctuations in the difference of the frequencies of the two driving pulses must be much less than $1/T_{\mathrm{transfer}}$ for the adiabaticity condition to be satisfied[13]. We achieve this by generating both driving pulses from the same pump laser by frequency shift, see Fig. 3.5. An AC voltage with frequency ω_{AOM} generates two light

fields in the first diffraction maximum of the acousto-optical modulator (AOM) with frequencies $\omega_{\mathrm{pump}} \pm \omega_{\mathrm{AOM}}$. In order to independently address both frequencies required for the state transfer (ω_{L1} and ω_{L2}), we send two electronic pulses to the AOM with frequencies $\omega_{\mathrm{AOM},i}$, $i = 1, 2$ and Gaussian envelopes generated by an arbitrary function generator (ArbFunGen). The pump laser detuning $\Delta = 3.5$ MHz is chosen so that $\omega_{\mathrm{L}i} = \omega_{\mathrm{pump}} + \omega_{\mathrm{AOM},i} = \omega_{\mathrm{cav}} - \omega_i$ for mechanical modes at ω_i, $i = 1, 2$, and the effect on the transfer process of the other pair of light fields at $\omega_{\mathrm{pump}} - \omega_{\mathrm{AOM},i}$ and harmonics $\omega_{\mathrm{pump}} + k \cdot \omega_{\mathrm{AOM},i}$, $k = 2, 3, 4, ...$ is negligible. The measured amplitude of the 2^{nd} harmonics is much smaller than that of the 3^{rd} harmonics, as is represented by the arrows labeled "harm." in Fig. 3.5. To check the effect of the harmonics, we excite the mechanical modes to a level much higher than the thermal motion and we send driving pulses individually during the mechanical decay. With the above shown value for Δ, mode 2 is not affected by the pulse sent to the AOM at $\omega_{\mathrm{AOM},1}$ within detection sensitivity, while the measured effect of the pulse at $\omega_{\mathrm{AOM},2}$ on mode 1 agrees well with the theoretically predicted optomechanical effect from the light fields at ω_{L2}.

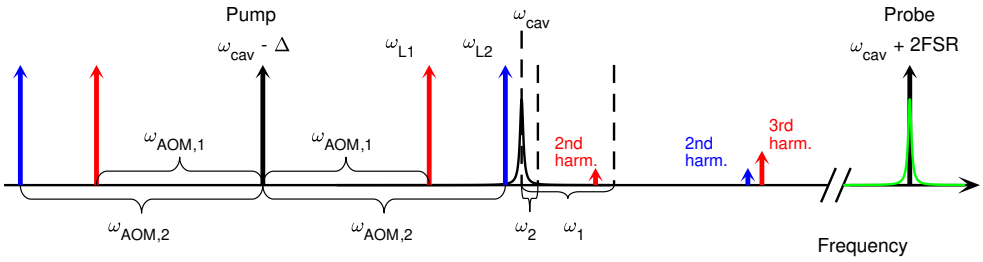

Figure 3.5: Scheme of the optical frequencies. The probe laser is locked to the cavity resonance at $\omega_{\mathrm{cav}} + 2\mathrm{FSR}$. The amplitude of the pump laser at $\omega_{\mathrm{cav}} - \Delta$ is fully modulated by an AOM driven with AC voltage at $\omega_{\mathrm{AOM},i}$, thus only the light fields at $\omega_{\mathrm{pump}} \pm \omega_{\mathrm{AOM},i}$ reach the cavity. The upper sidebands ($\omega_{\mathrm{pump}} + \omega_{\mathrm{AOM},i}$) drive the state transfer, while the unwanted light fields at $\omega_{\mathrm{pump}} - \omega_{\mathrm{AOM},i}$ have a negligible effect due to their large detuning. The nonlinear response of the AOM leads to harmonics (small red and blue arrows) which we measure to also have a negligible effect.

3.2.5 Calibration procedure

The transfer efficiency is defined as the ratio of the phonon population in mode 2 at the end of the transfer process to the phonon population in mode 1 at the beginning. The number of phonons in a mechanical mode $\langle \hat{b}_i^\dagger \hat{b}_i \rangle + \frac{1}{2} \propto u_i^2 \propto R_i^2$, where u_i is the amplitude of oscillation, and R_i is the amplitude of the demodulated reflection signal measured at $\omega_i + \omega_{\mathrm{EOM}}$. Thus the transfer efficiency is

$$\mathrm{Eff}_{1\to 2} = \frac{k_2 R_2^2(t_{end,1\to 2})}{k_1 R_1^2(t_{beginning,1\to 2})}, \tag{3.4}$$

where the state is transferred from mode 1 to mode 2 and k_i are coefficients of proportionality. Let us consider the reverse transfer $2 \to 1$. The product of the transfer

efficiencies

$$\mathrm{Eff}_{1\to2}\mathrm{Eff}_{2\to1} = \frac{R_2^2(t_{end,1\to2})}{R_1^2(t_{beginning,1\to2})}\frac{R_1^2(t_{end,2\to1})}{R_2^2(t_{beginning,2\to1})} \tag{3.5}$$

does not have any coefficients of proportionality, thus it can be measured directly without any calibration. For the parameters of the transfer $\sigma = 25$ ms and $\Delta t/\sigma = 1.25$, this product is measured to be 0.73 ± 0.05. This implies that we demonstrate a transfer efficiency of at least $\sqrt{\mathrm{Eff}_{1\to2}\mathrm{Eff}_{2\to1}} = 0.855 \pm 0.03$, independently of the model and calibrations. A numerical solution of the full model shows that for the above chosen σ and Δt, the efficiencies $\mathrm{Eff}_{1\to2}$ and $\mathrm{Eff}_{2\to1}$ differ by 0.01, which amounts to the transfer efficiency from the defect mode to the 3,3 mode being 0.86 ± 0.03, see Fig. 3.6.

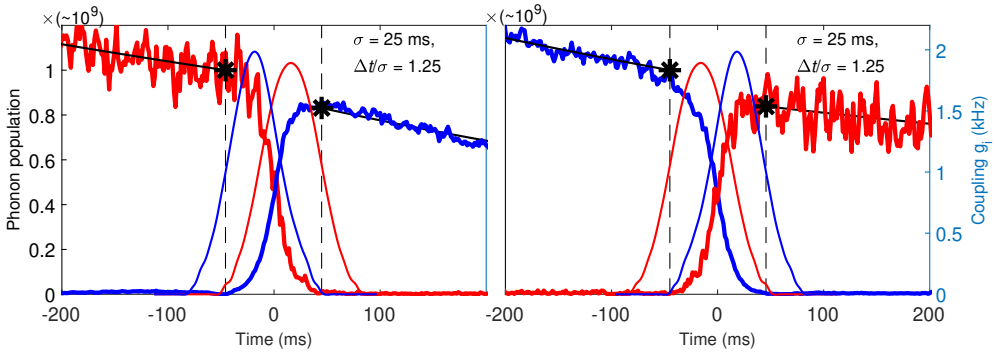

Figure 3.6: Representative single runs of state transfer from mode 1 to mode 2 (left) and in the opposite direction (right). Left scale, thick lines: phonon population as a function of time, red line corresponds to mode 1, blue line to mode 2, both divided by the phonon population of mode 1 in the beginning of the transfer. Right scale, thin lines: multiphoton optomechanical couplings $g_1(t)$ red line, $g_2(t)$ blue line. The driving field pulses have a nearly Gaussian temporal profile, but their beginning and ending are modified such that they have zero amplitude outside the pulse. Vertical lines indicate the beginning and ending of the transfer process. Black stars correspond to the phonon populations used to calculate the transfer efficiency.

The AOM used to shape the driving pulses has a non-linear intensity vs voltage response, which causes the actual temporal profile of the pulse's intensity to deviate from a Gaussian shape. Another consequence of this non-linearity is that the sum of intensities of individual pulses is not equal to the intensity of the pulse resulting from two Gaussian pulses being added and sent to the AOM. To account for these undesired effects, we measured the time profiles of the multiphoton optomechanical coupling $g_i(t)$ as follows. We excite mode 1 to a level much higher than the thermal occupation. During the mechanical decay, we send a single short Gaussian pulse $g_1(t, \sigma)$ to the cavity, with frequency $\omega_{\mathrm{L}1}$ and the same peak intensity as used for the STIRAP measurements. We adjust σ for this pulse so that exactly half of the initial excitation energy is lost due to the optomechanical damping. This gives $\sigma_{1,1/2} = 0.12 \pm 0.01$ ms. Numerical solution of Eq. (3.3) for such a pulse gives the peak value of the pulse $\max g_1(t) \sim 2$ kHz. Next a similar procedure is followed for mode 2,

but σ of the pulse is set equal to $\sigma_{1,1/2}$, and the peak value of the pulse is set so that exactly half of the initial excitation of mode 2 is lost after the pulse $g_2(t, \sigma_{1,1/2})$ at ω_{L2}. This gives the estimate of $\max g_2(t) \sim 2\,\mathrm{kHz}$ and the required voltage amplitude sent to AOM in the pulse.

To get the actual temporal profile of $g_i(t)$, we measure in transmission the time profiles of the intensities of the pulses used for the transfer, with $\sigma = 25\,\mathrm{ms}$ and with each value of $\Delta t/\sigma$ used for the measurements (-1, -0.75, -0.5, .., 3.5, 3.75, 4). In order to measure the exact temporal intensity profile of both STIRAP pulses individually, while both pulses are simultaneously applied (STIRAP sequence), the pump laser detuning Δ is adjusted such that $\omega_{\mathrm{cav}} - \omega_{\mathrm{L1}} \sim \kappa$, while $\omega_{\mathrm{L2}} + \omega_2 = \omega_{\mathrm{L1}} + \omega_1$ as always, making $|\omega_{\mathrm{cav}} - \omega_{\mathrm{L2}}| \gg \kappa$. Therefore the transmitted light consists almost exclusively of the intensity at ω_{L1}. To correct for the small fraction of light at ω_{L2}, we send this pulse individually with the same detunings, and subtract the measured transmission from the case when both pulses are present. We follow the same procedure in order to measure the individual intensity of light at ω_{L2}. The measured intensity profiles of the pulses are used in the numerical simulations presented here.

3.3 Theory

Here we derive Eq. (3.3) and the full model which accounts for the unmatched sidebands. We start from the optomechanical equations of motion [9] in the presence of two mechanical modes $\hat{b}_i$ and two coherent driving fields at ω_{L1} and ω_{L2} with the condition $\omega_{\mathrm{L1}} + \omega_1 = \omega_{\mathrm{L2}} + \omega_2 = \omega_{\mathrm{cav}}$, where ω_i is the frequency of mechanical mode i, i=1,2. In the linearized approximation and in the frame rotating at ω_{cav}, the total intracavity light fields $\hat{a}$ is

$$\hat{a} = |\bar{\alpha}_1(t)|e^{i(\omega_1 t + \phi_1)} + |\bar{\alpha}_2(t)|e^{i(\omega_2 t + \phi_2)} + \delta\hat{a}, \tag{3.6}$$

where $\bar{\alpha}_i$ is the amplitude of the intracavity field due to driving field i, ϕ_i is a constant and $\delta\hat{a}$ is a fluctuating term. The evolution of $\delta\hat{a}$ is given by

$$\delta\dot{\hat{a}} = -\frac{\kappa}{2}\delta\hat{a} + i(G_1\hat{x}_1 + G_2\hat{x}_2)\hat{a}, \tag{3.7}$$

where G_i is the optical frequency shift per displacement of the mechanical mode $\hat{x}_i = x_{zpm,i}(\hat{b}_i + \hat{b}_i^\dagger)$ with x_{zpm} being the zero-point motion of mode i. Neglecting the thermal occupation of the environment, the mechanical modes evolve as

$$\dot{\hat{b}}_i = (-\frac{\Gamma_i}{2} - i\omega_i)\hat{b}_i + ig_{0i}\hat{a}^\dagger\hat{a}, \tag{3.8}$$

where g_{0i} is the single photon optomechanical coupling of mode i. In the frame rotating at ω_i for both mechanical modes $\hat{c}_i = e^{i(\omega_i t + \phi_i)}\hat{b}_i$

$$\dot{\hat{c}}_i = -\frac{\Gamma_i}{2}\hat{c}_i + ig_{0i}\hat{a}^\dagger\hat{a}e^{i(\omega_i t + \phi_i)}. \tag{3.9}$$

The sidebands at ω_{cav} have much larger amplitude than the other sidebands. Thus RWA is a good approximation for this situation. Applying RWA and linearizing, we

obtain

$$\begin{aligned}\hat{a}^\dagger\hat{a}e^{i(\omega_i t+\phi_i)} &= (|\bar{\alpha}_1|e^{-i(\omega_1 t+\phi_1)} + |\bar{\alpha}_2|e^{-i(\omega_2 t+\phi_2)} + \delta\hat{a}^\dagger)\times \\ &\times (|\bar{\alpha}_1|e^{i(\omega_1 t+\phi_1)} + |\bar{\alpha}_2(t)|e^{i(\omega_2 t+\phi_2)} + \delta\hat{a})e^{i(\omega_i t+\phi_i)} = \\ &= |\bar{\alpha}_i|\delta\hat{a},\end{aligned}$$

$$\dot{\hat{c}}_i = -\frac{\Gamma_i}{2}\hat{c}_i + ig_{0i}|\bar{\alpha}_i|\delta\hat{a}, \tag{3.10}$$

$$\delta\dot{\hat{a}} = -\frac{\kappa}{2}\delta\hat{a} + iG_1 x_{zpm,1}|\bar{\alpha}_1|\hat{c}_1 + iG_2 x_{zpm,2}|\bar{\alpha}_2|\hat{c}_2. \tag{3.11}$$

Using the multiphoton optomechanical coupling $g_i(t) = G_i x_{zpm,i}|\bar{\alpha}_i(t)|$, changing notation $\hat{c} \to \hat{b}$ and $\delta\hat{a} \to -\delta\hat{a}$ we get Eq. (3.3):

$$i\dot{\hat{b}}_i = -i\frac{\Gamma_i}{2}\hat{b}_i + g_i(t)\delta\hat{a}, \tag{3.12}$$

$$i\delta\dot{\hat{a}} = -i\frac{\kappa}{2}\delta\hat{a} + g_1(t)\hat{b}_1 + g_2(t)\hat{b}_2. \tag{3.13}$$

Next, we consider the full model which includes the unmatched sidebands by not using RWA. We start with the linearized equation for the light fields Eq. (3.11) and the expression $\hat{x}_i = x_{zpm,i}(\hat{b}_i + \hat{b}_i^\dagger)$. Using Eq. (3.10) we get

$$\begin{aligned}\delta\dot{\hat{a}} = -\frac{\kappa}{2}\delta\hat{a} + i(g_{01}(\hat{b}_1 + \hat{b}_1^\dagger) + g_{02}(\hat{b}_2 + \hat{b}_2^\dagger))\times \\ \times (|\bar{\alpha}_1(t)|e^{i(\omega_1 t+\phi_1)} + |\bar{\alpha}_2(t)|e^{i(\omega_2 t+\phi_2)}).\end{aligned} \tag{3.14}$$

The dynamics of the mechanical modes is still described by Eq. (3.12). As before we change the frame by applying the transformation $\hat{c}_i = e^{i(\omega_i t+\phi_i)}\hat{b}_i$. In the expansion of its last term $ig_{0i}\hat{a}^\dagger\hat{a}$ the terms not including $\delta\hat{a}$ can be omitted and we get

$$\begin{aligned}\dot{\hat{c}}_i = -\frac{\Gamma_i}{2}\hat{c}_i + ig_{0i}e^{i(\omega_i t+\phi_i)}\times \\ \times (|\bar{\alpha}_1(t)|e^{-i(\omega_1 t+\phi_1)}\delta\hat{a} + |\bar{\alpha}_2(t)|e^{-i(\omega_2 t+\phi_2)}\delta\hat{a} + \\ + |\bar{\alpha}_1(t)|e^{i(\omega_1 t+\phi_1)}\delta\hat{a}^\dagger + |\bar{\alpha}_2(t)|e^{i(\omega_2 t+\phi_2)}\delta\hat{a}^\dagger).\end{aligned} \tag{3.15}$$

To simulate this model we average the operators $\hat{a}$, $\hat{c}$ to get the classical fields. Simulation of this model for the experimental parameters is done by solving these differential equations.

The transfer efficiencies calculated by the full model start to deviate from ones by Eq. (3.3) by more than 3% for pulses with $\sigma \gtrsim 25$msec. We see negligibly small dependence of the transfer efficiency on $\phi_1 - \phi_2$.

Note, simulations show that using Eq. (3.3) with added corrections due to the optical spring effect of the unmatched sidebands give incorrect result.

3.4 Results

STIRAP with parameters tuned for maximum phonon number state transfer efficiency is shown in Fig. 3.7. The measurement of a typical transfer process has the following sequence: mode 1 is excited to an amplitude much higher than its thermal occupation by applying an AC voltage in resonance with the mechanical frequency to a needle positioned close to the center of the membrane. During its free decay the

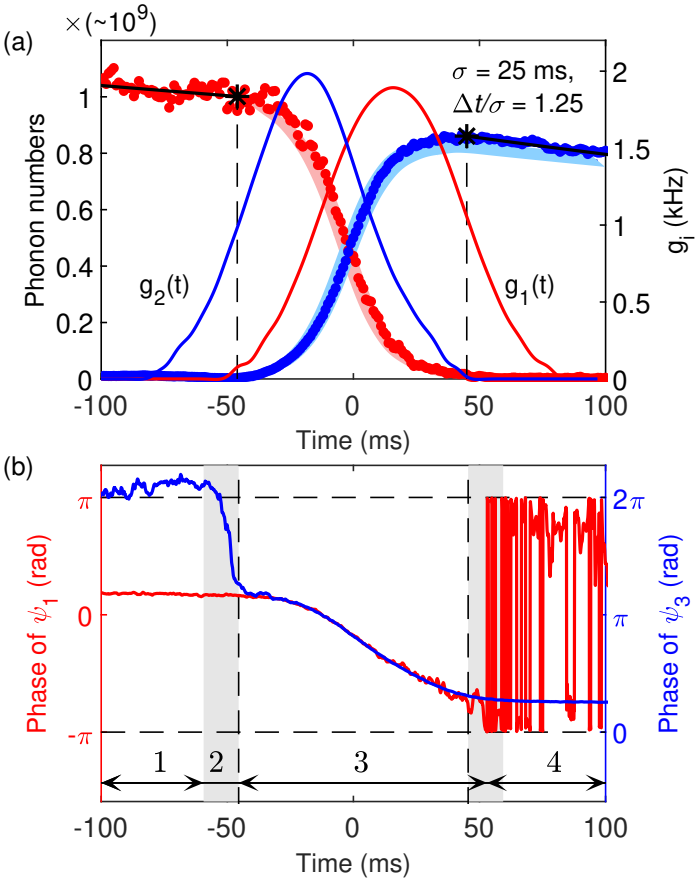

Figure 3.7: Experimental optomechanical STIRAP. (a) Left scale: phonon number as a function of time, red dots correspond to averaged measurements for mode 1 (ψ_1), blue dots for mode 2 (ψ_3). The prefactor 10^9 is a rough estimate. Light red and light blue regions represent the phonon populations with statistical uncertainties (1 standard deviation) obtained from simulations without free fit parameters. Right scale: multiphoton optomechanical coupling strengths, calculated from measured pulse intensities. The driving field pulses have a nearly Gaussian profile with the standard deviation parameter σ and separation Δt, but their beginning and ending are smoothly truncated to zero. Black stars correspond to the phonon populations used to calculate the transfer efficiency (5% of the peak voltage sent to the AOM). (b) Measured phases of mode 1 (red) and mode 2 (blue) in the rotating frame.

two optical pulses are sent which transfers the excitation of mode 1 to mode 2. The transfer starts with the beginning of pulse 1 (red) and finishes with the end of pulse 2 (blue), these moments are denoted by dashed vertical lines. The transfer efficiency is calculated as the ratio of the number of phonons in mechanical mode 2 at the end of the transfer to the number of phonons in mechanical mode 1 at the beginning of the transfer (black stars). A theoretical model without free fit parameters was developed in the classical limit to simulate the transfer process taking into account the corrections due to the other sidebands and the measured profiles of the light pulses (see section Theory), and shows excellent agreement to the experimental data in Fig. 3.7(a). Simulations show that the average rate of loss through the optical mode is $\sim$1 Hz in the dark state during the transfer. We observe small variations in the frequencies of the mechanical modes with each STIRAP sequence. To account for these variations, we measure the mechanical frequencies in thermal motion and adjust the values of the mechanical frequencies for the driving pulse generation accordingly before each STIRAP sequence.

In our realization of STIRAP using coherent state populations, i.e. in the classical regime, the phases of the mechanical modes during the transfer can be continuously monitored, see Fig. 3.7(b). There are four time domains with distinct behavior of phases: in domain 1 $g_1(t) = 0$ and the phase of mode 1 is defined by the excitation used to drive it, while mode 2 is in its thermal motion, thus the difference between the phases is random; in domain 2 STIRAP starts and the phase of mode 2 adjusts itself until the sidebands at $\omega_{\rm cav}$ become π out of phase; in domain 3 the phase of the locked mechanical modes changes due to the optomechanically induced frequency shift from field $\omega_{\rm L2}$ (unmatched sidebands); in domain 4 the read-out signal of mode 1 becomes much less than the read-out noise.

Next we investigate the dependence of the transfer efficiency on the parameters of the process. First the time delay between the optical pulses Δt is varied, see Fig. 3.8. The adiabaticity condition becomes more and more violated when the separation between the pulses is too small or too large, leading to decreasing efficiency. Then the duration of the pulses σ is varied while keeping the time delay Δt optimal. The adiabaticity condition is satisfied increasingly better with longer pulses such that for pulses with $\sigma = 100$ ms only 2% of the initial phonon population in mode 1 is lost through the population and decay of the optical mode. Nevertheless the efficiency starts to decrease for $\sigma \gtrsim 25$ ms due to the mechanical decay of the modes, setting the upper bound on the transfer efficiency. The solid curves in Fig. 3.8(a-b) are numerical results and Fig. 3.8(c-d) compare experiment and simulations for varying Δt and σ. We observe an increasing discrepancy between measured and simulated data for the state transfer with $\sigma \gtrsim 25$ ms. This is caused by membrane heating from the driving pulses and by the defect mode frequency dependence on the amplitude of the full membrane 3,3 mode, see below.

3.4.1 Membrane heating and non-linear effects

We observe increasing discrepancy of measured and simulated data for the state transfer with $\sigma \gtrsim 25$ msec. This is caused by membrane heating by the driving pulses and by the defect mode frequency dependence on the amplitude of the full

membrane 3,3 mode. Driving pulses heat the area of the membrane in the vicinity of the defect which decreases its frequency by $\sim$ 5 Hz (out of 1.25 MHz) through thermal expansion leading to a decrease in the local stress. We observed a frequency change of the defect mode persisting for some time after a driving pulse. The other effect that changes the frequency of the defect mode is non-linearity of the membrane. In the realization of STIRAP, the level of excitation of the 3,3 mode should be

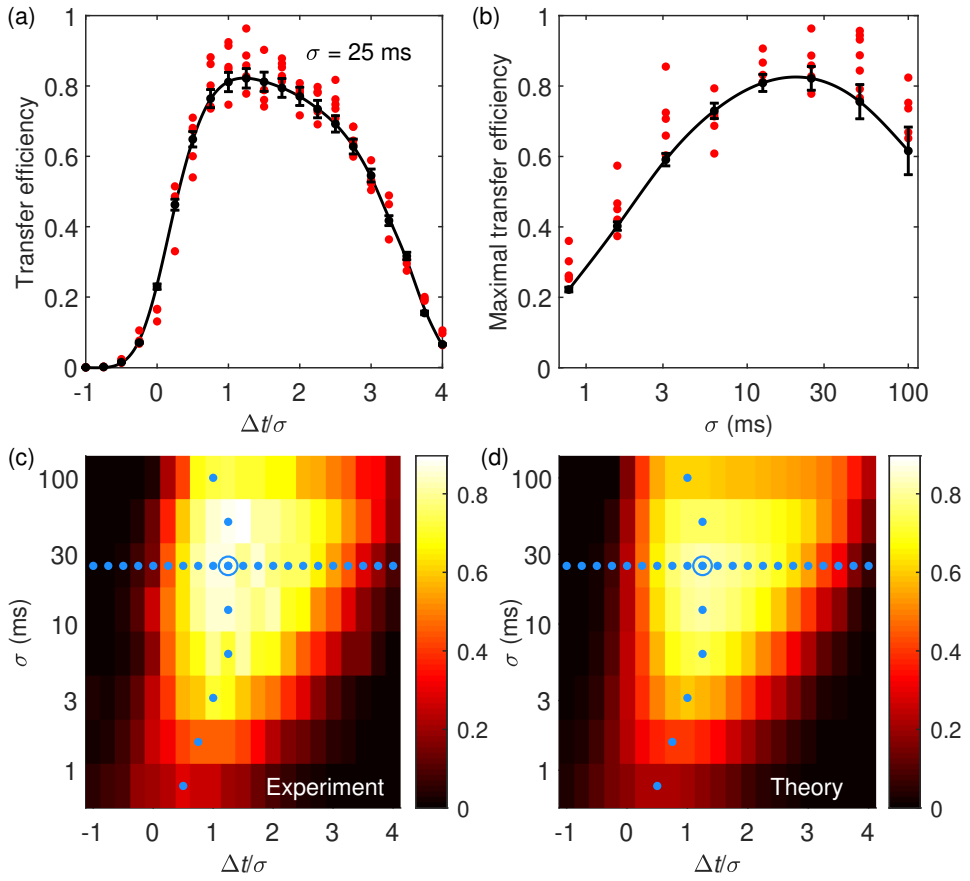

Figure 3.8: The transfer efficiencies under different parameters of the optical pulses. (a) The transfer efficiency as a function of the ratio of the delay between the pulses Δt and the Gaussian pulse width σ. Positive values of Δt correspond to the case that the field at ω_{L2} is applied before the field at ω_{L1}. (b) Maximal transfer efficiencies as a function of σ. In (a) and (b) the red dots show measured efficiencies in individual runs, black dots are the simulated efficiencies, and the black lines are guides to the eye. The increasing error bars for larger σ in (b) are due to observed but not accounted for small non-linear and heating effects. (c) and (d) show the experimental (c) and predicted (d) transfer efficiency as a function of the Gaussian parameter σ and separation Δt. The horizontal row of dots in (c) and (d) correspond to the data shown in (a), while the vertical row of dots correspond to the data shown in (b). The transfer process for the parameters corresponding to the open circle in (c) and (d) is shown in Fig. 3.7.

much higher than its thermal occupation. This requires relatively large amplitudes of the 3,3 mode which effects the frequency of the defect mode through increased stress in the membrane averaged over an oscillation of the 3,3 mode. We observed an increase of the frequency of the defect mode when the 3,3 mode is excited by a couple of Hz.

To calculate ω_{L1} and ω_{L2} we measure the frequencies of the mechanical modes in their thermal motion before each STIRAP sequence. The two effects described above shift the frequency of the defect mode, effectively introducing a small two-photon detuning with complicated dependence on time, which we do not take into account in our simulations. This small two-photon detuning of the order of 5Hz becomes comparable to the width of the two-photon detuning curve and starts influencing the state transfer with $\sigma \gtrsim 25$ msec as the width of the two-photon detuning curve is inversely proportional to σ.

A signature of STIRAP [13] is strong sensitivity of the transfer efficiency to the two-photon detuning $\Delta_{\mathrm{2ph}} = (\omega_{\mathrm{L1}} + \omega_1) - (\omega_{\mathrm{L2}} + \omega_2)$ given $\Delta_{\mathrm{1ph}} = 0$, compared to the sensitivity to the single-photon detuning $\Delta_{\mathrm{1ph}} = \omega_{\mathrm{cav}} - (\omega_{\mathrm{L1}} + \omega_1)$ given $\Delta_{\mathrm{2ph}} = 0$, Fig. 3.9. The frequency scale for the two-photon detuning is set by the duration of the transfer process: $\Delta_{\mathrm{2ph}} \sim \pi/\tau_{\mathrm{transfer}}$, implying that the sidebands at ω_{cav} accumulate a phase difference of π during the transfer and consequently no longer interfere destructively. The frequency scale for Δ_{1ph} is set by the optical cavity linewidth κ: non-zero Δ_{1ph} leads to changes in the intracavity light fields intensities and in the amplitudes of the sidebands.

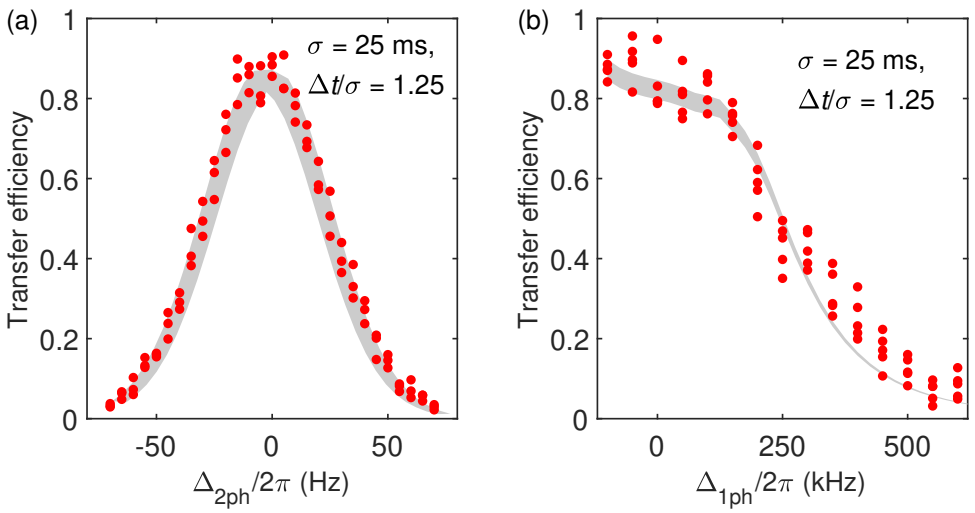

Figure 3.9: (a) The transfer efficiency as a function of the two-photon detuning Δ_{2ph} with zero single-photon detuning. (b) The efficiency as a function of the single-photon detuning Δ_{1ph} with zero two-photon detuning. In (a) and (b) the red circles are measured efficiencies in individual runs, and the shaded regions are simulated efficiencies with statistical uncertainties. The simulated curve in (a) has a frequency correction of 4 Hz caused by small non-linear and heating effects.

The highest phonon number transfer efficiency we observe in our system is $86 \pm 3\%$. The highest demonstrated state transfer efficiencies in other systems are: transmon qubit 83% [38]; Bose–Einstein condensate of atoms 87% [57]; trapped ions 90% [37]; superconducting Xmon qutrit 96% [58]; doped crystals $98 \pm 2\%$ [59]; atom beams $98 \pm 2\%$ [60]. In general, the STIRAP scheme in optomechanics can result in the transfer efficiencies close to unity if the following set of requirements is satisfied:

$$\begin{aligned} &\omega_i \gg \kappa, \\ &|\omega_1 - \omega_2| \gg \kappa, \\ &\kappa \gg \max g_i(t), \\ &\tau \max g_i^2(t) \gg \kappa, \\ &\Gamma_i \tau_{\mathrm{transfer}} \ll 1. \end{aligned} \tag{3.16}$$

The first two inequalities allow to address the mechanical modes individually; the third one is the weak coupling regime; the forth one is the adiabaticity condition; the last inequality assumes that the loss due to intrinsic mechanical decay during the transfer is small. This set of stringent requirements applies both to the classical and the quantum regime of STIRAP in optomechanics. Other experimental challenges are the accurate control of 1- and 2-photon detunings, circumventing detrimental effects of the unmatched sidebands, and proving stable subwavelength positioning of the membrane to maximize the coupling strength.

3.5 Conclusions

Here we have shown the first optomechanical implementation of STIRAP and demonstrated a maximum phonon number state transfer efficiency of $86 \pm 3\%$. The efficiency is benchmarked against variation in the STIRAP pulse duration and separation as well as against the STIRAP single- and 2-photon detuning and is found to be in good agreement with theory. Our quantum simulations show that STIRAP of a single phonon Fock state is feasible to observe with demonstrated technology. Furthermore, modified versions of STIRAP (fractional STIRAP [61], tripod STIRAP [62]) can be used to create and detect entangled mechanical states. Therefore, STIRAP in optomehanics can play an important role in quantum information protocols and in generating macroscopic superposition states.

4

Quantum state transfer and entanlement via STIRAP

In this chapter we show the feasibility of preparing a single-phonon mechanical Fock state in mechanical mode 1 and transferring this state to mechanical mode 2 using optomechanical STIRAP and reading out the final state with current technology. Also we discuss modifications to STIRAP allowing to entangle mechanical states and verify an entangled state.

This chapter is partially based on Supplemental Material of: **V. Fedoseev**, F. Luna, I. Hedgepeth, W. Löffler and D. Bouwmeester, Stimulated Raman Adiabatic Passage in Optomechanics, Phys. Rev. Lett. 126, 113601 (2021). Simulations of this chapter were done together with Ian Hedgepeth.

4.1 STIRAP of a single phonon state

4.1.1 Introduction

STIRAP technique was initially developed to manipulate quantum states. Here we show that optomechanical STIRAP can be used to manipulate quantum states of mechanical modes. State transfer via STIRAP of single-phonon Fock state can in principle be observed experimentally with the same membranes in a cryogenic setting. Specifically, we consider 2 defect modes of the membranes discussed before. We provide a full quantum treatment of the protocol for such a state transfer including known sources of noise and unwanted effects: thermalization to the environment, heating by the laser light fields, the presence of other nearby membrane modes, realistic overall detection efficiency and dark count rate of a single photon detector. We consider STIRAP between two modes of the defect of the phononic crystal in the membrane, with quality factors of 10^9 [63] (we observed 0.25×10^9 for one of our membranes at 1 K), resulting in a thermal decoherence time [9] of approximately 5 ms at 1 K (1 phonon is added from the environment). This sets the time scale for the whole experiment. In laser cooling experiments [64, 65] the steady state temper-

ature of similar membranes was observed to be less than 0.5 K above the cryostat base temperature when being sideband cooled, thus we adopt 1 K as a conservative estimate for the membrane temperature due to laser heating when operating in a dilution cryostat.

We assume the system to be at 1 K at all times for simplicity. The protocol consists of the following steps: both modes are sideband cooled to an average phonon occupation $\bar{n} = 0.1$, which is a reasonable assumption [64, 66, 67] and requires $g/\kappa \sim 0.03$ for our membranes, where g is the multiphoton optomechanical coupling, κ is the cavity linewidth; detection of a Stokes photon from a weak blue-detuned pulse projects the state of mode 1 to a state close to single-phonon Fock state; the STIRAP pulse sequence is sent; the state of the modes is read-out by a strong red-detuned pulse through detection of anti-Stokes photons. It is essential to filter out the strong pump light fields and to send the scattered photons to a single photon detector with high enough overall detection efficiency. Based on demonstrated experimental parameters we calculate that single-phonon Fock state can be transferred with fidelity of 60%.

We assume the following parameters of the system: mechanical mode 1 with resonance frequency $\omega_1/2\pi = 1.2$ MHz and quality factor $Q = 10^9$, single-photon optomechanical coupling $g_{01}/2\pi = 1$ Hz; mechanical mode 2 with resonance frequency $\omega_2/2\pi = 1.4$ MHz and quality factor $Q = 10^9$, single photon optomechanical coupling $g_{02}/2\pi = 1$ Hz; cavity linewidth $\kappa/2\pi = 50$ kHz and environment temperature $T = 1$ K. Such a high quality factor in membranes can be observed only for mechanical modes of a defect in the phononic crystal. Thus we are limited to the modes from the phononic bandgap typically having the width of 300 kHz. To minimize the crosstalk between mechanical mode 1 and mechanical mode 2, their resonances should be separated in frequency as much as possible, there should be no other modes in the vicinity of ~ 50 kHz. This defines our choice for ω_1 and ω_2.

The system evolution consisting of mechanical mode 1, mechanical mode 2 and the optical mode (all scattered photons) is calculated using Quantum Toolbox in Python (QuTiP) [68] during all the whole protocol. In the presence of N pump light fields α_i with detuning $\Delta_i = \omega_{\mathrm{L}i} - \omega_{\mathrm{cav}}$ the interaction part of the Hamiltonian reads as follows:

$$H_{\mathrm{int}} = \sum_{i=1}^{N}\sum_{j=1}^{2} g_{0j}\alpha_i(\hat{a}^\dagger e^{i\Delta_i t} + \hat{a}e^{-i\Delta_i t})(\hat{b}_j e^{-i\omega_j t} + \hat{b}_j^\dagger e^{i\omega_j t}) \tag{4.1}$$

in the triply rotating frame with mechanical frequencies and at ω_{cav}. We operate QuTiP in the density matrix formalism. The evolution of the full density matrix (mechanical mode 1, mechanical mode 2, the optical mode) is obtained via solving the Linblad equation:

$$\dot{\rho}(t) = \frac{-i}{\hbar}\left[H_{\mathrm{int}}, \rho\right] + \frac{\kappa}{2}\mathcal{L}(\hat{a}) + \sum_{i=1}^{2}\frac{\Gamma_{mi}}{2}\Big((\bar{n}_i + 1)\mathcal{L}(\hat{b}_i) + \bar{n}_i\mathcal{L}(\hat{b}_i^\dagger)\Big), \tag{4.2}$$

where $\mathcal{L}(\hat{O}) = \frac{1}{2}(2\hat{O}\rho(t)\hat{O}^\dagger - \rho(t)\hat{O}^\dagger\hat{O} - \hat{O}^\dagger\hat{O}\rho(t))$ are superoperators and $\bar{n}_i = (e^{\hbar\omega_i/k_bT} - 1)^{-1}$ is the average number of thermal phonons at the i-th mechanical frequency at the environment temperature T.

4.1.2 State preparation

We start from a thermal state of the mechanical modes corresponding to $T = 1$ K (about 10^4 phonons). Further, red-detuned pump light fields are sent to the cavity providing sideband cooling for each mechanical mode. We would like to note that sending two such light fields simultaneously looks very close to the STIRAP pulses (for the light frequency, not in the time domain). This might set the system in the dark mechanical state and prevent the loss of the mechanical population. To avoid this one of the light fields can be shifted in frequency by ~ 1 kHz from $\Delta_i = -\omega_i$, this will effectively destroy the mechanical dark state due to high 2-photon detuning.

In theory one can expect to reach $\bar{n}_{\min} = 10^{-4}$ for $g_r \sim \kappa$, but as the minimal reported thermal occupation is ~ 0.1 we restrict ourselves to $g_r/2\pi = 1600$ Hz resulting in the thermal state with $\bar{n} = 0.1$. This corresponds to a thermal state with

$$\begin{aligned} \rho_1^r =& 0.906\,|0\rangle\langle 0| + 0.085\,|1\rangle\langle 1| + 0.008\,|2\rangle\langle 2| + \ldots, \\ \rho_2^r =& 0.906\,|0\rangle\langle 0| + 0.085\,|1\rangle\langle 1| + 0.008\,|2\rangle\langle 2| + \ldots, \end{aligned} \tag{4.3}$$

where ρ_i^r is the reduced density matrix for mechanical mode i in the Fock basis.

Now mechanical mode 1 is prepared in a single-phonon state. For this a 0.1 ms blue-detuned pulse with $\Delta = \omega_1$ and $g^b/2\pi = 2410$ Hz is sent. This pulse increases the average occupation of the modes to $\bar{n}_1 = 0.20$ and $\bar{n}_2 = 0.12$ with the density matrices for modes 1 and 2:

$$\begin{aligned} \rho_1^b =& 0.831\,|0\rangle\langle 0| + 0.140\,|1\rangle\langle 1| + 0.024\,|2\rangle\langle 2| + \ldots, \\ \rho_2^b =& 0.893\,|0\rangle\langle 0| + 0.095\,|1\rangle\langle 1| + 0.010\,|2\rangle\langle 2| + \ldots. \end{aligned} \tag{4.4}$$

The pulse is weak, so that the probability of photon scattering in the cavity $p = 0.1$. Thus one time out of ten pulses a scattering event occurs and a Stokes photon is detected by the single photon detector (SPD). Such detection projects mechanical mode 1 state to a non-classical state:

$$\rho_1^{her} = 0.831\,|1\rangle\langle 1| + 0.140\,|2\rangle\langle 2| + 0.024\,|3\rangle\langle 3| + \ldots. \tag{4.5}$$

Just after the detection there is no vacuum component in mechanical mode 1 and its state is close to single-phonon state.

Detection of a scattered photon requires filtering of the pump light fields. Such a filter was demonstrated in [66] with pump light attenuation of 150 dB at a cost of 30% transmission for the light frequency of interest. Overall detection efficiency was reported 2.5% with avalanche SPD having detection efficiency of 30%.

In reality SPDs always have non-zero dark count rate (DCR), clicking of the detector due to DCR admixes thermal state ρ_1^b to the projected state of mechanical mode 1. Let's take this into account. A conservative estimate of DCR is 10 Hz, though our superconducting nanowire SPD (SNSPD) achieve DCR of 0.01 Hz with proper stray light isolation. Thus keeping in mind SNSPD with detection efficiency of 90% further we assume overall detection efficiency $\eta = 0.075$. The rate of detected Stokes

photons is $(\tau_b/p\eta)^{-1} = 75$ Hz, thus the density matrix of mode 1 after a click of the detector is

$$\begin{aligned}\rho_1^i &= \frac{10\text{ Hz}}{10\text{ Hz}+75\text{ Hz}}\rho_1^b + \frac{75\text{ Hz}}{10\text{ Hz}+75\text{ Hz}}\rho_1^{her} = \\ &= 0.098\,|0\rangle\langle 0| + 0.750\,|1\rangle\langle 1| + 0.126\,|2\rangle\langle 2| + \dots .\end{aligned} \tag{4.6}$$

Detection of the Stokes photon practically does not change the state of mode 2.

4.1.3 STIRAP

The previous steps are repeated until a click of the SPD. Just after the click the STIRAP pulse sequence $\alpha_1(t)$ and $\alpha_2(t)$ is sent, where

$$\begin{aligned}\alpha_1(t) &= \alpha_{max} e^{-(t-\tau)^2/2\sigma^2} \\ \alpha_2(t) &= \alpha_{max} e^{-(t+\tau)^2/2\sigma^2}\end{aligned} \tag{4.7}$$

and $\sigma = 0.14$ ms, $\tau = \sigma/3$, $\alpha_{max} = 5000$. Simulation of these pulses with the initial state ρ_1^i and ρ_2^b produces Fig. 4.1. The resulting states of the mechanical modes after the pulses are

$$\begin{aligned}\rho_1^s &= 0.900\,|0\rangle\langle 0| + 0.091\,|1\rangle\langle 1| + 0.007\,|2\rangle\langle 2| + \dots , \\ \rho_2^s &= 0.370\,|0\rangle\langle 0| + 0.447\,|1\rangle\langle 1| + 0.137\,|2\rangle\langle 2| + \dots .\end{aligned} \tag{4.8}$$

Mode 1 is in a state very close to the initial thermal state ρ_1^r. The single phonon transfer efficiency is $0.447/0.75 = 0.596$.

Note that for this calculation the scattered photons at ω_{cav} are not monitored. In the hypothetical case of very high total detection efficiency $\eta \sim 1$ the state transfer fidelity can be increased to near unity: if the heralding photon during the STIRAP pulses is detected, then the quantum state of mechanical mode 1 is lost to the optical mode and the whole experiment should be repeated until no such heralded photon is detected.

Low temperature of the environment is essential for this experiment. We simulated the transfer at $T = 8$ K, the results are shown in Fig. 4.2. In this case thermalization to environment is 8 times faster, and STIRAP with high transfer efficiency would require higher than available pump intensity (due to weak coupling requirement). With $\alpha = 5000$ the evolution of probability of mode 2 being in single phonon state is similar to just thermalization to the environment without the STIRAP pulses.

4.1.4 Readout

The final state of the mechanical modes is read out with a strong red-detuned pulse with $g/2\pi = 5000$ Hz and duration of 0.5 ms (each mode requires separate read out with appropriate detuning $\Delta = -\omega_i$). Such a pulse provides a scattering probability of 99.8% and thus if the mechanical mode is not in the vacuum state, this pulse

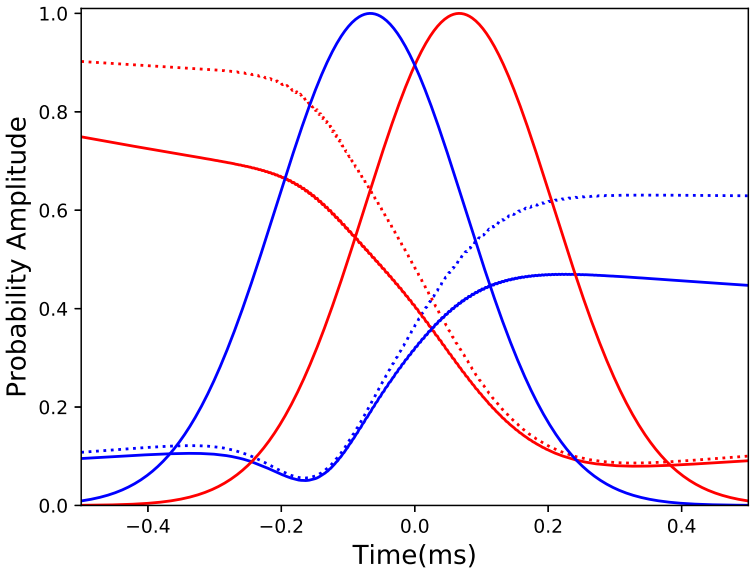

Figure 4.1: State transfer using STIRAP at 1K. Red and blue represent the first and second modes respectively. Solid denotes the probability of detecting a single phonon (ρ_{11}), while dotted denotes the probability that the mode is populated ($1 - \rho_{00}$). The efficiency of state transfer is 59.6% and includes unmatched sidebands.

produces an anti-Stokes photon (or photons). We assume that the SNSPD is not photon number resolving, meaning that absorption of a two photon state results in the same click as a single photon. So we cannot distinguish between a single phonon and more than 1 phonon state of a mechanical mode. Thus what we can observe is $1 - \rho_{00}$ rather than ρ_{11}. This probability is plotted in Fig. 4.1 by dashed line. Knowledge of the total detection efficiency η and DCR of our detector allows to estimate $1 - \rho_{00}$ term of both mechanical modes.

4.1.5 Discussion

The whole experiment looks as follows:
1) both modes are sideband-cooled during 5 ms;
2) the blue-detuned pulse is sent. If the heralded photon is detected, we proceed to step 3), otherwise repeat 1) and 2);
3) the STIRAP pulse sequence is sent;
4) the red-detuned readout pulse is sent to get information about mechanical mode i, $i = 1$ or 2.

Let's calculate the time to get a single anti-Stokes photon detection at step 4). To

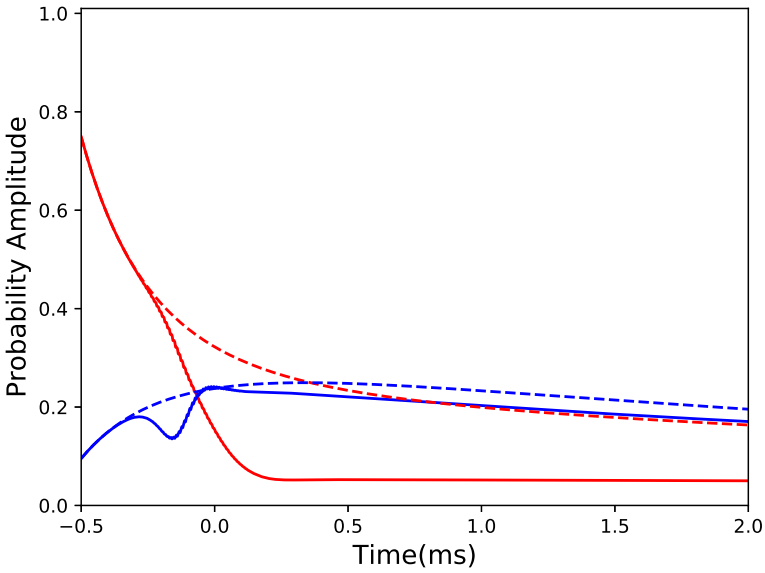

Figure 4.2: State transfer at 8K realized using STIRAP. Red and blue represent the first and second modes respectively. Solid denotes a state transfer via STIRAP, while dashed denotes evolution in the presence of the environment, without the STIRAP pulses.

get to step 3) it will take on average

$$T_3 = \frac{5\text{ ms} + 0.1\text{ ms}}{0.1\eta} = 0.7\text{ s}. \tag{4.9}$$

The probability to detect a single anti-Stokes photon at step 4) is

$$P_f = \eta(1 - \rho_{00}) < 0.075. \tag{4.10}$$

Thus the time to get a single anti-Stokes photon detection at step 4) is $\frac{T_3}{P_f} > 9.3$ s. Now, let's estimate the effect of DCR of 10 Hz. The detection rate of the heralding Stokes photon from 2) is 75 Hz. At this stage our single-phonon state preparation deteriorates, but not significantly, see above. During the detection of herading anti-Stokes photon from step 4) the signal rate is

$$f_4 = (\frac{0.5\text{ ms}}{P_f})^{-1} = 150\text{ Hz (for } 1 - \rho_{00} = 1). \tag{4.11}$$

At step 4) DCR should be subtracted from the clicking rate. DCR equals the photon detection rate for $1 - \rho_{00} = 0.07$. We can conclude that DCR of 10 Hz is not a limiting factor for the considered parameters of the experiment.

4.1.6 Other Membrane Modes

Now we consider the presence of other nearby mechanical modes in the membrane. The STIRAP protocol relies on the heralding Stokes photons from the blue-detuned pulse and anti-Stokes photons from the read-out pulse. These two pulses affect other modes of the membrane in the frequency range of a few κ around ω_1 and ω_2. As a consequence, a flux of spurious Stokes and anti-Stokes photons is produced by these modes. We have observed modes in our membranes with quality factors as low as 10^6 in the vicinity of mode 1 and 2. The upper bound of the rate for the phonons to enter these modes from the environment is 100 kHz (based on $\Phi \approx \Gamma_m n_{th}$ where $n_{th} = 10^5$). Additionally, the upper limit for the conversion of phonons into photons for these modes is $\Gamma_{opt}/2\pi$ <2 kHz.

Because we are operating in the bandgap of our membrane, the spurious modes are at least 70 kHz away from modes 1 and 2. This is also the minimal frequency separation of the spurious photons from ω_{cav}, where the heralded photons are passing through the cascade of filtering cavities described above. These filtering cavities produce at least 50 dB of isolation at 70 kHz [66] detuning, which decreases the flux of the spurious photons factor of 10^5 not taking into account the detection efficiency. This causes the rate of detector clicks due to other modes in the membrane to become negligibly small and does not effect the STIRAP protocol.

4.1.7 Conclusions

We discussed and estimated quantitatively a protocol where two mechanical modes of our membrane are cooled near a quantum ground state, mode 1 is prepared in a close to single-phonon Fock state and this state is transferred to mechanical mode 2 of the same membrane. We used conservative parameters of the whole experiment and showed that it is feasible to observe such a state transfer with state of the art membrane-in-the-middle sideband-resolved system. We included in our consideration all known experimental complications. The main challenge of the experiment is to keep heating of the membrane due to pump light fields at a level that the temperature of the membrane is below 1 K. This requirement appears to keep the rate of thermalization to environment at an acceptable level.

4.2 Creation and detection of an entangled state

In [69] it was shown that the STIRAP pulse sequence can be modified to produce a system in a superposition of two quantum states. Let's consider the dark state which the system is following during STIRAP:

$$\Phi_0(t) = \cos\theta(t)\psi_1 - \sin\theta(t)\psi_3, \tag{4.12}$$

with $\tan\theta(t) = \Omega_{12}(t)/\Omega_{23}(t)$, where $\Omega_{ij}(t)$ is the Rabi frequency of the coupling between states i and j. In STIRAP we start from the system being in state ψ_1 requiring $\Omega_{12}(t=-\infty)/\Omega_{23}(t=-\infty) = 0$ and finish in state ψ_3 requiring $\Omega_{23}(t=\infty)/\Omega_{12}(t=\infty) = 0$, see Fig. 4.3. If the pulses are modified such that they start as in STIRAP and finish with constant ratio of drive strength $\Omega_{12}(t)/\Omega_{23}(t) = \text{const} = r$, see Fig. 4.4, then the system ends up in a superposition state

$$\Phi_{\text{final}} = \alpha\psi_1 - \beta\psi_3, \tag{4.13}$$

where $\alpha = 1/\sqrt{1+r^2}$ and $\beta = r/\sqrt{1+r^2}$. Indeed, at the time when the ratio of the driving strengths approaches r (dashed line Fig. 4.4) the system reaches state Φ_{final}, and at all times after this moment the system stays in Φ_{final} including the time when the pulses are finished.

In optomechanical STIRAP such modified pulses with $r = 1$ will produce an entangled state of the mechanical modes:

$$\Phi_{\text{final}} = (|1\rangle_1 |0\rangle_2 - |0\rangle_1 |1\rangle_2)/\sqrt{2}, \tag{4.14}$$

where $|n\rangle_i$ is mechanical mode i in n-phonon Fock state. All simulations of this section are done with the following parameters: $\omega_1/2\pi = 1.2$ MHz, $\omega_2/2\pi = 1.4$ MHz, $Q = 10^9$, $\kappa/2\pi = 50$ kHz, $g_{\max}/2\pi = 5$ kHz, $T = 0$. These parameters satisfy the criterion of adiabaticity and are chosen to show the properties of fractional STIRAP in a clear way. Note, the optical mode (green dashed line) is practically not populated in line with the adiabatic evolution.

Due to time reversal symmetry this process can be reversed: we start from a superposition $(|1\rangle_1 |0\rangle_2 - |0\rangle_1 |1\rangle_2)/\sqrt{2}$ and after the pulses have been sent mode 1 reaches single-phonon state, mode 2 reaches vacuum state, see Fig. 4.5. The optical mode is also practically not occupied in this process.

But if the initial state of the system differs from Eq. 4.14, then this state is also different from the dark state dictated by the ratio of the drive strengths. Thus the quantum state of the system will evolve to reach this dark state. For example, if the initial state of the system is $(|1\rangle_1 |0\rangle_2 + |0\rangle_1 |1\rangle_2)/\sqrt{2}$, then the optical mode becomes populated during the pulses, see Fig. 4.6. By the time system reaches the dark state (approximately -0.8 ms) all the population is lost to the optical mode and the final state is vacuum for both mechanical modes.

For any other initial state different from $(|1\rangle_1 |0\rangle_2 + |0\rangle_1 |1\rangle_2)/\sqrt{2}$ the final state will not be vacuum. For example, if the initial state is a classical mixture

$$\rho = (|1\rangle_1 |0\rangle_2 \langle 0|_2 \langle 1|_1 + |0\rangle_1 |1\rangle_2 \langle 1|_2 \langle 0|_1)/2, \tag{4.15}$$

then the final state is $\rho_1 = 0.5\,|0\rangle\langle 0| + 0.5\,|1\rangle\langle 1|$ and mode 2 is in the vacuum state, see Fig. 4.7. The system reaches the dark state at approximately -0.8 ms loosing half of the initial population to the optical mode and then the system follows the dark state according to the driving pulses without further loss.

These properties of reversed fractional STIRAP open a way to probe the quantum

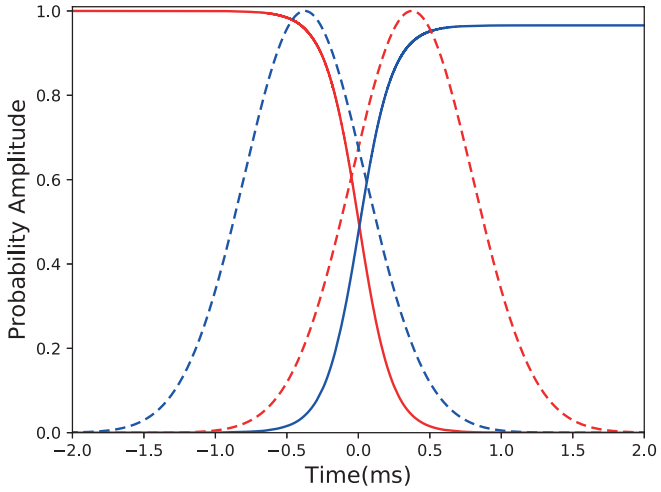

Figure 4.3: State transfer using STIRAP at $T = 0$. Red and blue represent mechanical mode 1 and mechanical mode 2 respectively. Solid lines denote the probability of a single Fock state ρ_{11}, while dashed lines denote the pulses driving strength Ω_{12} and Ω_{23}.

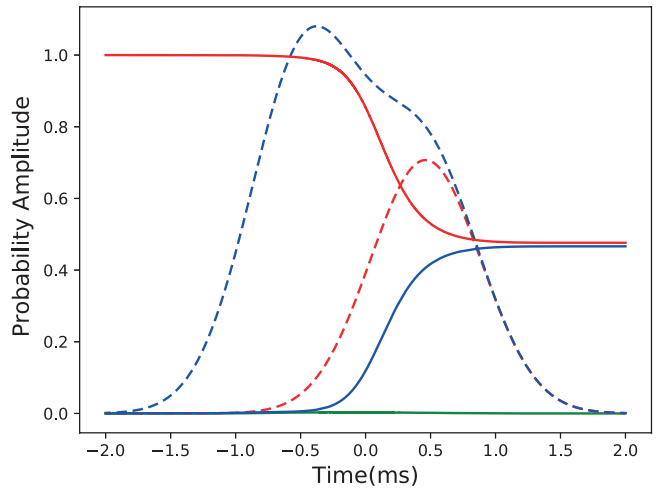

Figure 4.4: Creation of mechanical modes entanglement $(|1\rangle_1 |0\rangle_2 - |0\rangle_1 |1\rangle_2)/\sqrt{2}$ using fractional STIRAP at $T = 0$. Red, blue and green represent mechanical mode 1, mechanical mode 2 and the optical mode respectively. Solid lines denote the probability of a single Fock state ρ_{11}, while dashed lines denote the pulses driving strength Ω_{12} and Ω_{23}.

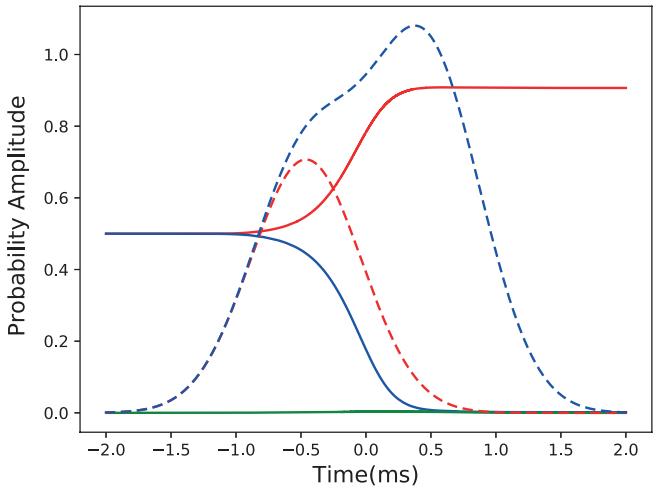

Figure 4.5: Reverse fractional STIRAP: entanglement verification, initial state $(|1\rangle_1 |0\rangle_2 - |0\rangle_1 |1\rangle_2)/\sqrt{2}$. Mode 1 ends up in single-phonon state. Red, blue and green represent mechanical mode 1, mechanical mode 2 and the optical mode respectively. Solid lines denote the probability of a single Fock state ρ_{11}, while dashed lines denote the pulses driving strength Ω_{12} and Ω_{23}.

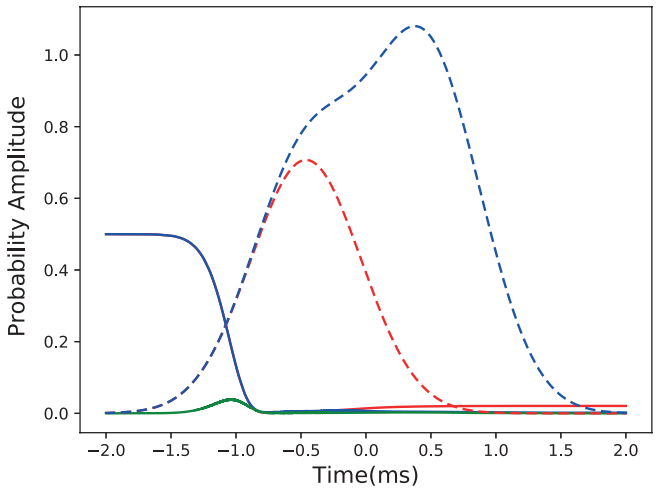

Figure 4.6: Reverse fractional STIRAP: entanglement verification, initial state $(|1\rangle_1 |0\rangle_2 + |0\rangle_1 |1\rangle_2)/\sqrt{2}$. Both mechanical modes end up in vacuum state. Red, blue and green represent mechanical mode 1, mechanical mode 2 and the optical mode respectively. Solid lines denote the probability of a single Fock state ρ_{11}, while dashed lines denote the pulses driving strength Ω_{12} and Ω_{23}. Note, the loss occurs via population of the optical mode.

state of a multimode optomechanical system as demonstrated by the three cases of different initial states. Thus this process can be used to differentiate between an

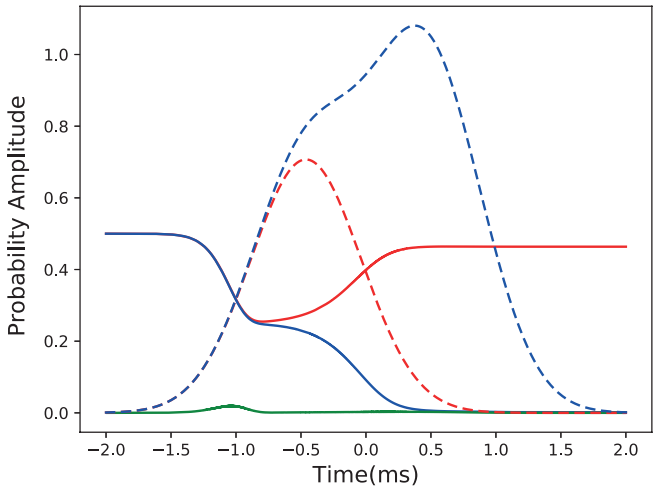

Figure 4.7: Reverse fractional STIRAP: entanglement verification, initial state is statistical mixture $\rho = (|1\rangle_1 |0\rangle_2 \langle 0|_2 \langle 1|_1 + |0\rangle_1 |1\rangle_2 \langle 1|_2 \langle 0|_1)/2$. Mode 1 ends up in approximately $\rho = 0.5 |0\rangle \langle 0| + 0.5 |1\rangle \langle 1|$. Red, blue and green represent mechanical mode 1, mechanical mode 2 and the optical mode respectively. Dashed lines denote the probability of a single Fock state ρ_{11}, while solid lines denote the pulses driving strength Ω_{12} and Ω_{23}. Note, the loss occurs via population of the optical mode.

entangled state and a classical statistical mixture.

Another application of STIRAP in optomechanics is testing whether extra channels of decoherence are present in the system. Dark mode evolution in STIRAP requires the presence of the off-diagonal terms in the full density matrix as can be seen from Eq. 4.12. If a particular model of decoherence requires fast decay of the off-diagonal terms, then during the STIRAP pulses all the population will be lost to the optical mode similar to the considered case shown in Fig. 4.6, and the final population will be vacuum for all the modes. Therefore, experimental STIRAP resulting in the vacuum state for a system where a non-vacuum final state is predicted by the theory might indicate the existence of extra decoherence channels.

5

Cryogenic cavity

This chapter describes a cryogenic cavity with a membrane in the middle. The cavity is coupled to a single-mode optical fiber with coupling efficiency above 90% at mK temperatures without realignment during cooling down. The setup is prealigned at room temperature to compensate for the thermal contraction and change of the refractive index of the optical components during cooling down. This section is based on **V. Fedoseev**, M. Fisicaro, H. van der Meer, W. Löffler and D. Bouwmeester, Realignment-free cryogenic macroscopic optical cavity coupled to an optical fiber, Rev. Sci. Instrum. 93, 013103 (2022).

5.1 Introduction

Complex optical systems with several optical elements are challenging to cool down while keeping aligned due to thermal contraction and changes in refractive index [70]. Therefore such systems are often based on optical free space access cryostats [70, 71, 64, 63] to allow for external compensation of the optical misalignment. Alternatively, fiber coupled optical systems with cryogenic compatible actuators can be used leading to an increase in design complexity and requiring active control protocols while cooling down [72, 73]. Such systems are of particular interest for quantum optomechanical experiments that require low temperature environment and high collection efficiencies [9, 3, 74, 66, 75] because the rate of thermal decoherence is proportional to the temperature of the environment [9]. In quantum optomechanical experiments detection of a scattered photon projects the mechanical system into a specific quantum state. Therefore the total collection efficiency η of the heralding photons is essential for high fidelity operations and affects the duration of data collection τ in such experiments: $\tau \propto 1/\eta^n$, $n \geq 2$ [4, 76]. A constituent of the total collection efficiency is the coupling efficiency of the cryogenic optical cavity to the outside optical path, often an optical fiber. In a Helium-4 flow cryostat with free space optical access a coupling efficiency of 60% is reported [66], while for a free space optical access dilution cryostat a coupling efficiency of 85% was achieved [77].

Keeping mode matching between a single-mode fiber and a free space cavity with cryogenic actuators is even more challenging, requiring many degrees of freedom to be controlled during cooling down. The resulting mode matching in such systems is quite limited, with reported values in the range of 30-40% [78, 15].

Here we present a fiber coupled free space 10 cm long Fabry-Perot resonator which is designed to be fully axially symmetric. This allows for room temperature prealignment of the system such that the optimal alignment is obtained at cryogenic temperatures. Without any position adjustments during a cool down 96±2% coupling efficiency between a single-mode fiber and the optical cavity with a finesse of 12000 at the optical wavelength of 1064 nm is achieved. The elimination of actuators does not only simplify the system but also significantly improves the mechanical stability which is of vital importance for optomechanical experiments [70].

5.2 Design

Figure 5.1 shows the design concept of our custom-built optical setup. Figure 5.2 shows the design drawing of the setup including the membrane holder. Figure 5.3 shows a photo of the setup during membrane alignment. The main body and all the elements in contact with the optical components are made of Invar 36 to minimize thermal contraction. The light reaches the setup via an optical fiber (1060XP) which is terminated with a ceramic ferrule, not angled. The ferrule is held by a differential screw (Invar 36) with a pitch difference of 0.1 mm, where the rotatable part is depicted in red. The inner part of the differential screw is connected to a leaf spring, which allows translation along the optical axis without rotation, and eliminates movement of the inner part due to the tolerances in the threading. Tests of the differential screw showed that the light originating from the fiber ferrule and passing through the first lens only deviates by no more than 1 mm at a distance of 1 m from the ferrule when the screw is rotated by one turn.

Another important design feature is that the lenses and mirrors are held in compartments (light grey) which are pressed towards the body of the setup (dark grey) along the optical axis with springs. The compartments can be shifted perpendicularly to the optical axis by four screws. When the alignment is finished, the screws are retracted which does not change the position of the compartments, and the compartments are held in place by friction. A small shift of the lenses perpendicularly to the optical axis leads to small changes of the position and direction of the light between lens2 and mirror1, effectively acting as a periscope.

	lens1	lens2	mirror1	mirror2
Focal length, mm	4.5	48	25	25
Distance from the fiber tip, mm	4.2	40	94	190
Material	D-ZK3	N-BK7	fused silica	fused silica

Table 5.1: Positions and properties of the optical elements calculated using Gaussian beam propagation.

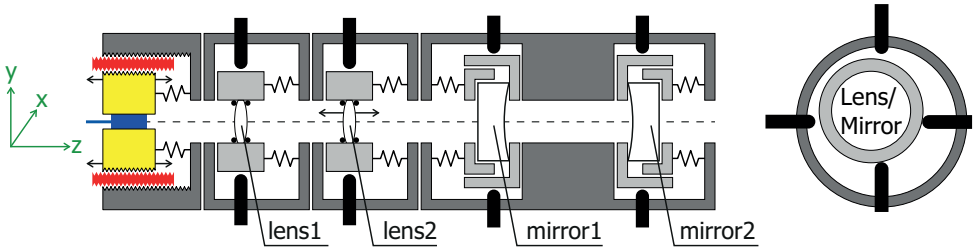

Figure 5.1: Cryogenic setup. The setup is axially symmetric and is made mostly of Invar 36. The fiber ferrule is held in a differential screw, the part shown in red can be rotated, the inner part of the screw is pushed with a leaf spring and allows for purely translational shifts of the ferrule along the optical axis. The lenses and mirrors are held in compartments (light grey) which are pushed against the setup modules (dark grey) with springs. These compartments can be shifted perpendicularly to the optical axis by 4 screws (right sketch). The screws are retracted after the alignment and the compartments are held by friction during cooling down.

The system is designed to be fully axially symmetric: the thermal contraction and change of optical properties of the elements lead to the shift of the waist position of the cavity mode relative to the fiber tip only along the mechanical axis, which can be precompensated before cooling down. The system can be aligned in such a way that the light in the setup travels along the mechanical axis of symmetry. In a conventional design with fixed mirrors and a periscope the cavity mirrors are, to some degree, randomly positioned not guaranteeing the coincidence of the optical and mechanical axes. This issue is especially important for a cavity close to concentric where the angle between the two axes in the cavity α is given by $\tan\alpha = e/(2R - L)$ in the symmetric cavity case, e is the error of positioning of the mirrors, R is the mirrors radius of curvature, L is the distance between the mirrors. For our case of $L = 94$ mm, $R = 50$ mm and a typical error of $e = 0.1$ mm would lead to $\alpha = 0.017$ rad or 0.8 mm shift of the beam center on the mirror.

5.3 Alignment procedure

Positions of the optical elements leading to the theoretically perfect mode matching are shown in Table I. The aligning procedure starts with positioning mirror1 on the mechanical axis of the setup (z-axis). Light going from the fiber through lens1 and a pinhole at the position of mirror2 on the mechanical axis is imaged with an intensity calibrated camera. This allows to position lens1 such that the optical and mechanical axes coincide. Next mirror1 is added and its position is adjusted to maximize the light intensity coupled back to the fiber. This defines the final position of mirror1.

Next, lens2 is placed at the calculated optimal position (see Table I). The fiber ferrule z-position, (x,y) positions of lens1 and lens2 are adjusted to maximize the light intensity coupled back to the fiber. The fiber tip is not anti-reflection coated

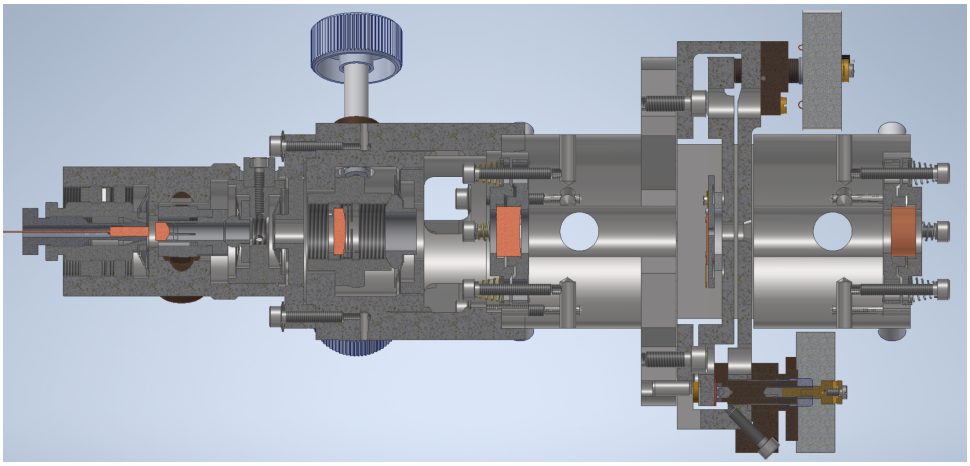

Figure 5.2: Design drawing showing cross-section of the setup. The optical elements are shown in orange: fiber ferule, lens1, lens2, mirror1 and mirror2. Only two translation screws are shown out of 16. The membrane is held on a plate glued to the piezo, which in turn is glued to the sample holder. The sample holder consists of two parts connected by a leaf spring, physically it is one Invar piece (amazing job by our Fine Mechanics Department). The sample holder moving part is resting on three cryogenic piezo motors.

and is not angled, and 3.4% of light is reflected back into the fiber. This reflection interferes with the light reflected from mirror1. The visibility of this interference allows to calculate the coupling efficiency of the light back-reflected from mirror1 [see Fig. 5.6(a)]. The fine adjustment of the fiber ferrule z-position and the lens positions (ferrule z-position, (x,y) positions of lens1 and lens2) are made to minimize the interference visibility.

Now, mirror2 is added. First, its position is changed to maximize the transmission of the 0,0 transverse mode, fine adjustment is achieved by minimizing the 0,1 and 1,0 transverse Hermite-Gaussian modes transmission. The difference in the beam diameters of the light coupled to the cavity and the cavity mode is best visible in the non-zero transmission through 0,2 and 2,0 transverse Hermite-Gaussian modes. This gives an indication whether lens2 is positioned properly.

Lens2 can be shifted along the z-axis and is fixed by two threaded retaining rings. Final position of lens2 is found through repeating the two previous steps: for a set of different z positions of lens2 z-position of the ferrule and (x,y) positions of lens1 and lens2 are adjusted to maximize the light reflected from mirror1 and coupled to the fiber, and mirror2 position is adjusted to minimize the 0,1 and 1,0 couplings. The lens2 z-position with minimal 0,2 and 2,0 transmission is the optimal one. In the end of this procedure we achieved a configuration where 98.5% of light is transmitted through the 0,0 mode and the rest is almost equally distributed between modes 0,1, 1,0, 0,2 and 2,0 modes. Transmission through other higher-order modes is at least one order of magnitude lower.

Finally, the setup is precompensated for the changes due to cooling down: in the ideal axially symmetric case the change of the optical properties of the compo-

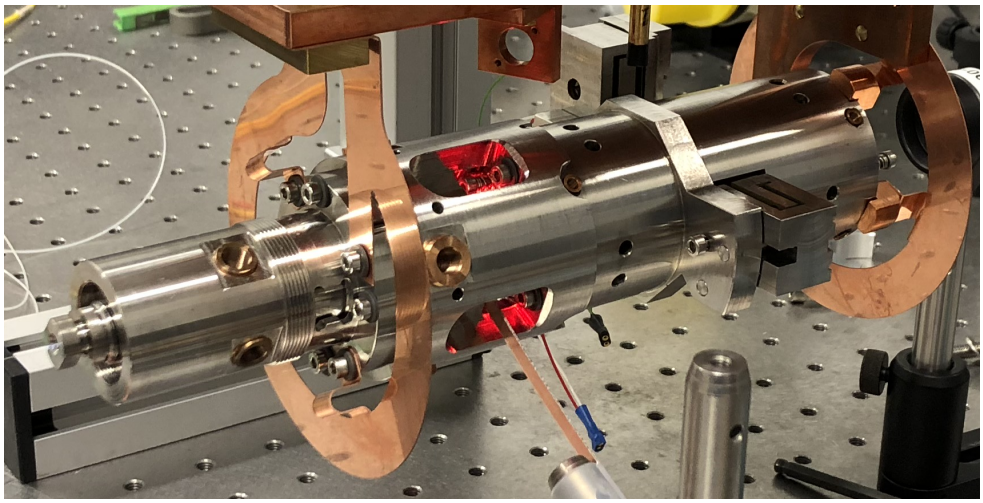

Figure 5.3: Photo of the setup held by copper plates. A red LED is used for membrane positioning.

nents and thermal contraction effectively result in a shift of the waist z-position of the cavity mode at the fiber and its spot size. The spot size change has negligible effect on the fiber-cavity mode overlap. This makes it possible to precompensate for the cooling down effects only by shifting the fiber ferrule along the optical axis outwards from the cavity relative to the optimal room temperature coupling configuration. (x,y) positions of the lenses are readjusted to maximize the coupling of the light reflected from mirror1 to the fiber after the ferrule shift to compensate for small beam-pointing changes mentioned above. In the experiment reported here, the ferrule was retracted by 32$\pm$3 μm before the cool-down. The retraction for this cool down is an estimate of the required precompensation based on the two previous cool downs. Each cool down provides a better estimate of the required precompensation for the next cool down.

5.4 Membrane alignment

Although the measurements below were done without a membrane, here we present a procedure of membrane positioning for this setup. The goal of the membrane positioning is to place the membrane perpendicular to the cavity mode, also the optical mode should cross the membrane in the middle of the phononic crystal defect (~ 250 μm in diameter), another requirement is that the membrane should be close to the center of the cavity. The last requirement is to mode match membrane reflection with the cavity mode and to minimize the 2FSR drifts discussed in Chapter 3. Firstly, the membrane is properly positioned in the xy-plane. To achieve this, a light emitting diode (LED) is placed on the optical axis just between lens2 and mirror1, see Fig. 5.3. An LCD camera positioned after mirror2 is imaging the phononic crystal, see Fig.

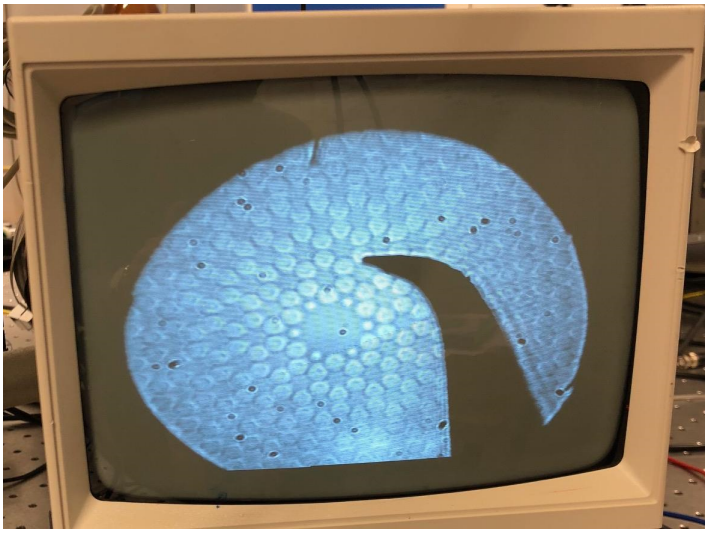

Figure 5.4: Imaging of the membrane placed in the setup. A shadow of the sharp tip for membrane driving by resonant AC voltage is visible near the phononic crystal defect.

5.4. Then, the LED is removed and 1064 nm laser light is sent into the cavity. The center of the Gaussian profile of the transmitted light is marked on the screen. After that, the LED is inserted again to the same position and the membrane holder is manually shifted in the xy-plane to achieve such a position that the center of the phononic crystal defect is coinciding with the transmitted light mark. When this is achieved, the screws holding the sample holder are tightened. This method is checked by the following observation: the sample holder is manually moved while observing the transmission signal; when the relative position of the mark and phononic crystal defect is such the mode is supposed to lie outside of the defect, the transmission signal abruptly decreases (checked for the shifts to the left, right, up and down).

Next, the membrane tip-tilt is corrected. Rough tip-tilt alignment is achieved by adjusting the tip-tilt screws while observing the shape of the transmitted light scanning the temperature of the laser crystal (300 mV at 1 Hz, small Innolight laser, effectively 0.1 FSR pk-pk based on our membranes reflectivity). When rough alignment is finished the reflection dip should be order of half of the reflection dip without the membrane. The relative position of the optical mode and the phononic crystal defect may change during the tip-tilt adjustment: for large changes due to rotation and due to the leaf-spring shift in the xy-plane because of friction.

Fine tip-tilt position is achieved by monitoring the reflection dip dependence on the membrane z-position relative to nodes of the standing wave light pattern in the cavity. Adjustment of the tip-tilt leads also to a shift of the membrane on the wavelength scale. The orthogonal position of the membrane relative to the optical axis is associated with the smallest reflection signal on resonance for all the membrane positions relative to the nodes. Practically it is achieved by finding a tip-tilt position with minimal reflection signal on resonance during the membrane shift by $\lambda/4$ along

the z-axis.

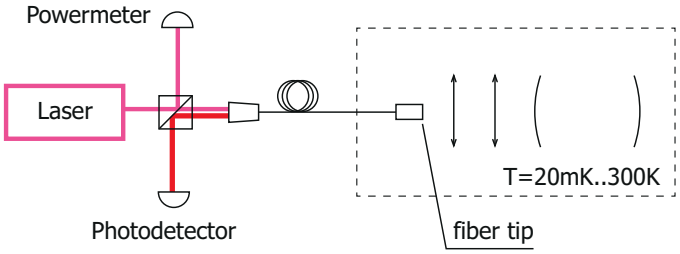

Figure 5.5: The whole setup used for measurements. The cavity is placed in a dilution cryostat. The fiber tip of the cryogenic setup is not angled and is not antireflection-coated, the light reflected from the tip interferes with the light both reflected and leaking from the cavity.

5.5 Measurements

The fiber tip is not anti-reflection coated and is not angled, therefore the reflection signal measured by the photodetector is the result of interference of the reflections from the fiber tip, mirror1 and mirror2, see Fig. 5.5. This allows us to accurately measure the change of the coupling efficiency of the light back-reflected from mirror1 α_m, and coupling efficiency of the cavity mode α_c. In this article, we define "coupling efficiency" of a field E as the intensity mode overlap of the fiber field E_f and E diminished by the losses ϵ:

$$\alpha = \frac{|\int E^* E_f dA|^2}{\int E_f^* E_f dA \int E^* E dA}(1-\epsilon). \tag{5.1}$$

In particular, if the total intensity losses on the way from the fiber tip to mirror1 are ϵ_{single} (say, a dust particle on the fiber tip and reflections from lens1, lens2 and back mirror1 surfaces) then

$$\begin{aligned} \alpha_m &= \frac{|\int E_m^* E_f dA|^2}{\int E_f^* E_f dA \int E_m^* E_m dA}(1-\epsilon_{\text{single}})^2, \\ \alpha_c &= \frac{|\int E_c^* E_f dA|^2}{\int E_f^* E_f dA \int E_c^* E_c dA}(1-\epsilon_{\text{single}}). \end{aligned} \tag{5.2}$$

The expression for α_m includes the term $(1-\epsilon_{\text{single}})^2$ as the light traveling from the fiber and back is experiencing the losses ϵ_{single} twice. The total reflectivity amplitude is given by

$$r_{\text{total}} = -r_1 + \frac{(1-r_1^2)Me^{i\phi_1}}{1-r_1 Me^{i\phi_1}}, \tag{5.3}$$

where

$$M = \sqrt{\alpha_m} r_2 - \frac{\alpha_c t_2^2 r_3 e^{i\phi_2}}{1-r_2 r_3 e^{i\phi_2}} \tag{5.4}$$

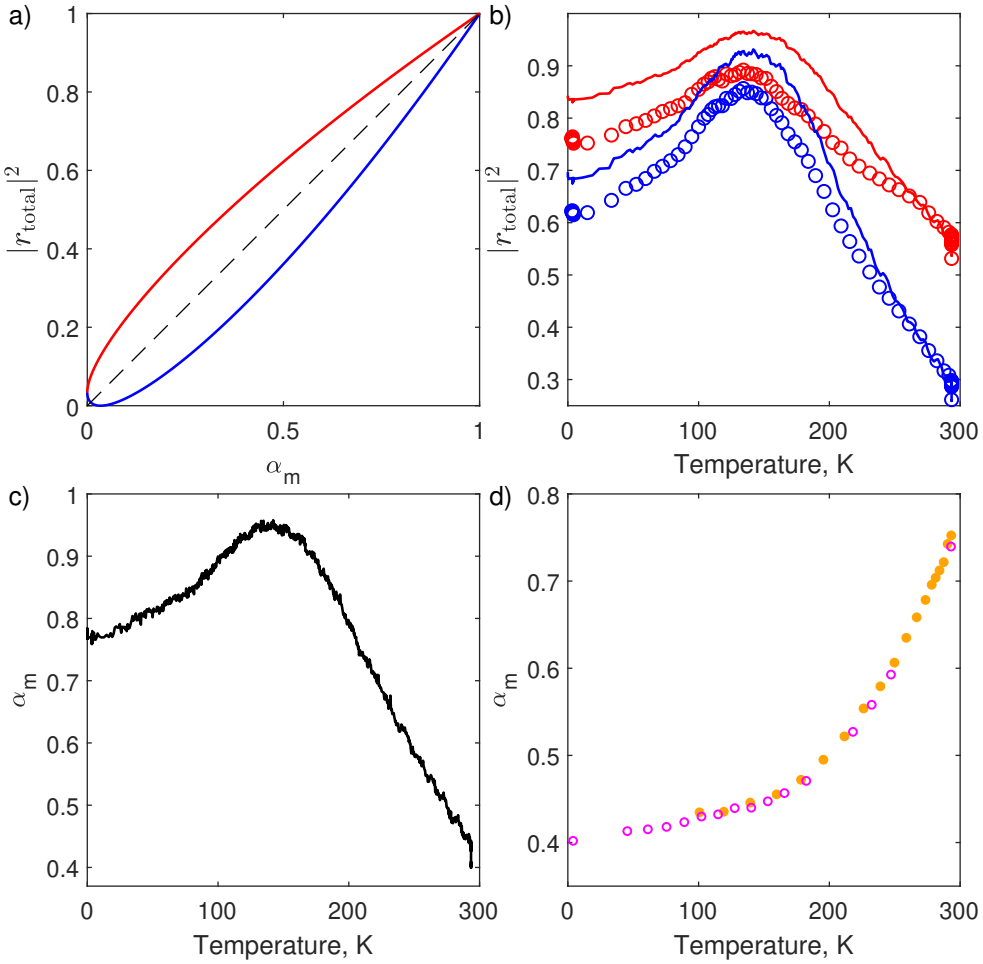

Figure 5.6: Total reflectivity $|r_{\text{total}}|^2$ far away from cavity resonances. (a) Theoretical interference of the light back-reflected from the fiber tip and mirror1 coupled into the fiber vs fiber coupling efficiency of the light back-reflected from mirror1 α_m. The red (blue) line is the maximum (minimum) total reflectivity $|r_{\text{total}}|^2$ for a given coupling efficiency. (b) Red (blue) lines/circles show the measured maximum (minimum) reflectivity due to the interference described in (a) during cooling down of the setup. The lines show the values extracted from measured visibility of the interference, while the circles show the reflectivity calculated as the ratio of light intensities measured by the photodetector and the powermeter with the ratio scaling corresponding to the room temperature measurements. (c) Coupling efficiency of back-reflected light from mirror1 α_m vs temperature extracted from the measured interference visibility. In the inset we demonstrate the reversibility of the coupling efficiency changes by showing the coupling efficiency α_m vs temperature for cooling down and warming up. The data is from another experimental run with a different optics positioning, magenta circles - cooling down, orange circles - warming up.

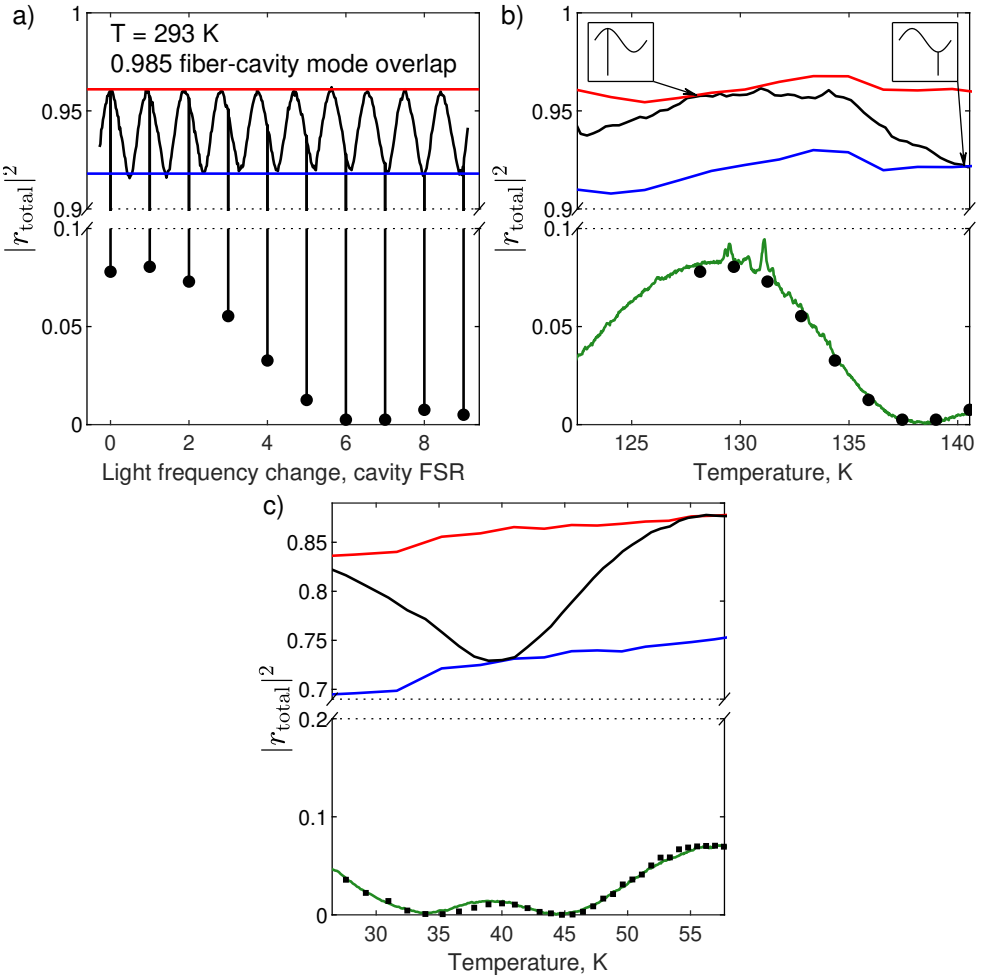

Figure 5.7: Total reflectivity $|r_{\mathrm{total}}|^2$. (a) Room temperature light frequency scan in the case of optimal alignment before the precompensational shift of the ferrule. The cavity resonance dips were measured separately. (b) A particular cavity resonance is traced during cooling down (after the precompensation). The black line shows the off-resonant reflectivity in the vicinity of the traced resonance, red (blue) - maximum (minimum, excluding cavity resonances) reflectivity when the laser frequency is swept over 1 FSR of the fiber tip - mirror1 system. The insets show the relative phases between the fiber tip - mirror1 system and the cavity. Green - resonance reflectivity of the traced cavity resonance. Black circles show the resonance reflectivity values mapped from the room temperature alignment shown in a). The very similar reflection properties of the optimal alignment at room temperature and at 130 K shows that the setup alignment at 130 K is very close to the best achievable alignment at room temperature. (c) Black, red, blue and green - same as in b). Black squares represent theoretical reflectivity dip values calculated with $\alpha_c = 94\%$.

and r_1, r_2, r_3 are reflectivity amplitudes of the fiber tip, mirror1, mirror2, respectively. t_2 is transmissivity amplitude of mirror1, $\phi_1 = 2\pi/\lambda \times 2L_{t1}$ with $\lambda = 1064$ nm and L_{t1} being fiber tip - mirror1 optical distance, $\phi_2 = 2\pi/\lambda \times 2L_c$ with L_c being cavity length. According to the specifications, mirror1 and mirror2 have an intensity transmissivity of 250 ppm; the scattering and absorption loss is not specified, but our measurements are consistent with 30 ppm. $r_1 = \sqrt{0.034}$ based on the Fresnel coefficients for silica.

First, let's consider optical frequencies far away from the cavity resonances (detuning from the nearest cavity resonance >10 cavity linewidths, cavity finesse is 12000). For these frequencies the measured reflection signal is the interference of the system fiber tip - mirror1. In this case Eq. 5.3 can be simplified:

$$r_{\text{total}} = \frac{-r_1 + \sqrt{\alpha_m} r_2 e^{i\phi_1}}{1 - r_1 r_2 \sqrt{\alpha_m} e^{i\phi_1}}. \tag{5.5}$$

The theoretical total reflectivity $|r_{\text{total}}|^2$ minimum and maximum values ($\phi_1 = 0$ and $\phi_1 = \pi$ respectively) are shown in Fig. 5.6(a) as a function of coupling efficiency of back-reflected light from mirror1 α_m. For known r_1 and r_2 the visibility of this interference is a function of α_m only. This allows us to accurately estimate the coupling efficiency α_m by measuring the visibility of the interference between the fiber tip and mirror1 reflections during cooling down of the setup, no calibration is needed. The minimum and maximum of the total reflectivity can be calculated from the measured visibility data, these are plotted by the solid lines in Fig. 5.6(b).

The total reflectivity can also be calculated directly as a calibrated ratio of the reflection signal and the powermeter signal, see Fig. 5.5. Resulting minimum and maximum reflectivity values are shown by circles in Fig. 5.6(b). This estimation assumes that the transmission of the optical fiber going to the cryostat does not change with time/temperature. There is a fiber connector in the cryostat at the 4 K plate, which might explain the difference between the two estimates of the total reflectivity. The coupling efficiency of the light back-reflected from mirror1 α_m calculated using the visibility data is shown in Fig. 5.6(c). There is an initial discontinuity in α_m at room temperature. This change occurred during evacuation of the cryostat vacuum chamber causing a change in properties of the optical elements. α_m reaches 95% at 140 K setting an upper bound on the total losses: $\epsilon_{\text{single}} \leq 0.025$. Lens1, lens2 and the back sides of the mirrors have anti-reflection coatings with a reflectivity of ~0.2% per surface (specs) setting the lower bound on the total losses: $\epsilon_{\text{single}} \geq 0.01$.

The change of the coupling efficiency with temperature is reversible: α_m is the same for a given temperature during cooling down and warming up as shown in Fig. 5.6(d) (data from previous cool down).

Next, we consider interference of the fiber tip, mirror1 and mirror2. The highest cavity mode overlap we could achieve at room temperature is 0.985 as stated in the section Alignment Procedure. A laser frequency scan covering 9 cavity resonances is shown in Fig. 5.7(a). A fit of Eq. 5.3 gives $\alpha_c = 0.965$ for this data, providing an estimate of the losses $\epsilon_{\text{single}} = 0.02 \pm 0.005$ (0.985/0.965-1). The interference pattern of fiber tip - mirror1 results in the sinusoidal reflectivity variation. The optical path from the fiber tip to mirror1 is 6% longer than the cavity length, which agrees

well with the ratio of the cavity and fiber tip - mirror1 free spectral ranges of $8.5/8$ extracted from Fig. 5.7(a).

During the cooling down the laser frequency was actively controlled in a way to trace the same resonance of the cavity. To achieve this, the laser frequency was scanned over 100 cavity linewidths once a second and the laser frequency was corrected to keep the cavity resonance approximately in the middle of each frequency scan. The reflectivity on cavity resonance is shown by green lines in Fig. 5.7(b) and 5.7(c). Every 10 minutes the laser was scanned over 1 fiber tip - mirror1 FSR to obtain the minimum and maximum reflectivity (blue and red lines in Fig. 5.7(b) and (c)).

The data plotted by black, blue and red lines in Fig. 5.7(a) and (b) allows to estimate ϕ_1 from Eq. 5.3. This phase information allows to map the reflectivity dip values from the optimal room temperature alignment onto the 130 ± 10 K temperature interval as depicted by black circles in Fig. 5.7(b). To do this ϕ_1 is estimated for each resonance from Fig. 5.7(a) and the resonance reflectivity values from Fig. 5.7(a) are plotted for temperatures corresponding to the same set of ϕ_1 values estimated from Fig. 5.7(b). Minimum and maximum reflectivity values together with the reflectivity on cavity resonance are practically the same for the optimal alignment at room temperature (before precompensation) and at around 130 K which can be seen by direct comparison of the data from Fig. 5.7(a) and (b). Therefore, the cavity indeed can be precompensated to reach near optimal alignment at cryogenic temperatures.

During the two temperature intervals shown in Fig. 5.7(b) and (c) ϕ_1 was changing by approximately 2π. The data with ϕ_1 spanning 2π is enough to extract a single value of α_c consistent with Eq. 5.3: 0.96 for Fig. 5.7(b) and 0.94 for Fig. 5.7(c). This analysis was performed on 7 additional temperature intervals giving 7 additional single values α_c, these estimates of the cavity coupling efficiency are shown by blue circles in Fig. 5.8.

Next, we check the hypothesis whether the cavity misalignment is axisymmetric during the cool down. Under this assumption the mode overlap of the back-reflected light from mirror1 with the fiber mode is a single variable function of the distance Δz_m between the fiber tip and the waist of the mirror1 back-reflected light, depicted by the red arrows in the inset of Fig. 5.8. We estimated that the beam waist radius of the back-reflected light changes negligibly small during the cool down. The back-reflected light from mirror1 mode overlap with the fiber mode can be calculated as $\alpha_m/(1-\epsilon_{\text{single}})^2$, see Eq. 5.2, and then used to calculate Δz_m as all parameters of the Gaussian beams are known.

The distance between the fiber tip and the waist of the light leaked from the cavity at the fiber tip [see inset Fig. 5.8] Δz_c is twice smaller than Δz_m because the light leaked from the cavity goes through lens1 and lens2 once, while the light back-reflected from mirror1 goes through lens1 and lens2 twice: $\Delta z_c = \Delta z_m/2$. Calculated values of $\Delta z_c(T)$ are shown in Fig. 5.8 by the red line. This estimate $\Delta z_c(T = 293\text{ K}) = 30\ \mu m$ agrees well with the precompensation shift of the fiber ferrule of 32$\pm$3 μm. Further, calculated values of $\Delta z_c(T)$ are used to calculate $\alpha_c(T)$ shown by the blue line in Fig. 5.8. These values are consistent with the previous estimates of $\alpha_c(T)$ based on the reflection dip measurements (blue circles) confirming the hypothesis of mainly axisymmetric misalignment of the setup during cooling down. The calculated fiber ferrule precompensation shift to reach the highest cavity

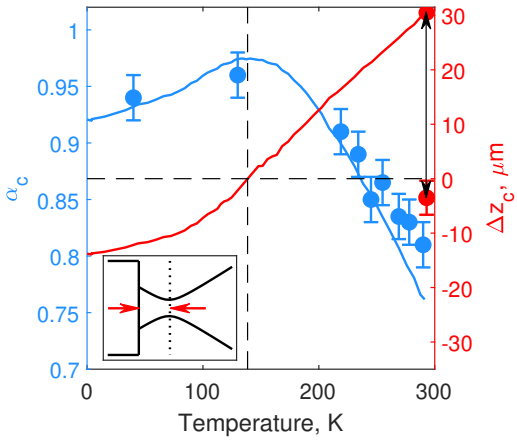

Figure 5.8: Cavity mode coupling efficiency (left axis). Blue circles - fits to the measured reflection data. Red line - shift of the cavity mode waist at the fiber tip (see inset) calculated from the data of Fig. 5.6(c) under the assumption that the misalignment due to cooling down is axial symmetric. Such a shift would result in the cavity mode coupling efficiency depicted by the blue line. The arrow represents the ferrule shift made at room temperature to precompensate for the changes due to cooling down. Dashed lines are guides to the eye.

mode coupling efficiency at mK temperatures is 45 μm.

Next, we discuss vibrational properties of the setup. The setup was cooled in a dilution cryostat with cooling provided by a pulse tube cryocooler known to introduce high levels of vibrations. We used a mass-spring system [79] acting as a fourth-order mechanical low pass filter with corner frequency of 50 Hz. The filter was placed between the 20 mK plate and the cryogenic cavity setup. The optical linewidth of the cavity was 130 kHz, the Pound-Drever-Hall lock was extremely stable with visible mechanical vibrations at 2-4 kHz just above the noise floor of our detection scheme while using 20 μW of probe laser intensity. Due to the monolithic design of the cryogenic cavity the most likely part susceptible to vibrations at 2-4 kHz are the mirror spring-loaded holders.

This setup is designed for quantum optomechanical experiments [75] where temperatures below 1 K and high collection efficiencies are required [74, 66]. For this, we have made an opening in the center of the cavity where an Invar 36 based holder can be mounted with a Si chip with a transparent high-stress SiN membrane. The membrane can be positioned at the waist of the cavity mode (beam waist radius 60 μm) and vibrational modes of the membrane are coupled to the light inside the cavity. The cavity finesse with the membrane is $\sim$10000, requiring the membrane to maintain its orientation perpendicularly to the optical axis during cooling down within $\sim 10^{-4}$ rad according to our experience. Cooling down the setup with the membrane shows the behavior of the reflectivity dip similar to Fig. 5.7(c), indicating that the loss due to membrane tilt is below 10^{-5} per membrane transmission. To maximize the collection efficiency of the photons scattered on the vibrations of the membrane, mirror2 will be exchanged for a 10 ppm transmission mirror to send

the light leaking from the cavity predominantly towards the fiber. We would like to note that the absence of an anti-reflection coating on the fiber tip does not diminish the collection efficiency in the case of the ideal cavity - fiber mode matching and transmissivity of mirror1 being much larger than the transmissivity of mirror2: the scattered photon will leak from the cavity preferentially through mirror1 and will be either transmitted to the fiber or reflected from the fiber tip, and after entering the cavity will leak again towards the fiber.

5.6 Conclusions

We developed and characterized a single-mode fiber-coupled cryogenic optical cavity enabling cavity mode coupling efficiency above 90% at mK temperatures. In particular, the setup does not require realignment during cooling down, due to the axisymmetric design and low expansion of the body made from Invar. The optics are aligned at room temperature to precompensate for the thermal contraction and change of refractive index during cooling down. The cavity mode coupling efficiency increases upon the start of cooling down from 81$\pm$2%, reaches 96$\pm$2% at 130 K and stabilizes at 92$\pm$2% at dilution cryostat temperatures. As there are no actuators in the setup and due to its monolithic design, it has increased stiffness which reduces its susceptibility to vibrations in the cryostat.

The setup is designed to operate in the membrane-in-the-middle configuration [54] for optomechanical experiments in the quantum regime [75] where high collection efficiency is essential [66].

6

Setup for optomechanical quantum experiments

In this chapter we discuss the optical setup that has been built, as well as new components that are still under construction, in our laboratory for quantum optomechanical experiments.

Full setup overview

Figure 6.1 presents a schematic overview of our setup for quantum optomechanical experiments involving mechanical state projection via detection of the Stokes and anti-Stokes scattered photons. Let's consider an example of a single-phonon state preparation considered in Chapter 4 as the first step for STIRAP of a quantum state. Experimentally we start from the mechanical mode being sideband cooled close to its ground state. Next, the cooling tone is switched off and a weak blue-detuned pump pulse is sent to the cryogenic cavity. With small probability the pulse will result in a Stokes photon. To separate the Stokes photon from the pump pulse the light leaking from the cavity is sent through a special optical filter. The filter consisting of 4 consecutive high-finesse cavities is resonant with the cryogenic cavity and thus the pump pulse is reflected from the filter cavities, while the Stokes photon is transmitted and then detected by a superconducting nanowire single photon detector (SNSPD).

The cryogenic cavity was described in the previous chapter.

In the first section the set of the filter cavities is discussed. These are four stable cavities of very similar design to the cryogenic cavity. These cavities are held in a room temperature vacuum chamber and the length of each cavity is controlled by a microprocessor within 5 pm. This work was done together with Sebastian ten Haaf [80] and Owen Huisman [81].

In the second section we describe the superconducting nanowire single photon detectors with $> 90\%$ detection efficiency and 10 mHz dark count rate installed in our dilution cryostat. This work was done together with Remi Claessen [82].

Kellan Colburn (UCSB) and Xinrui Wei also participated in the work presented in this chapter.

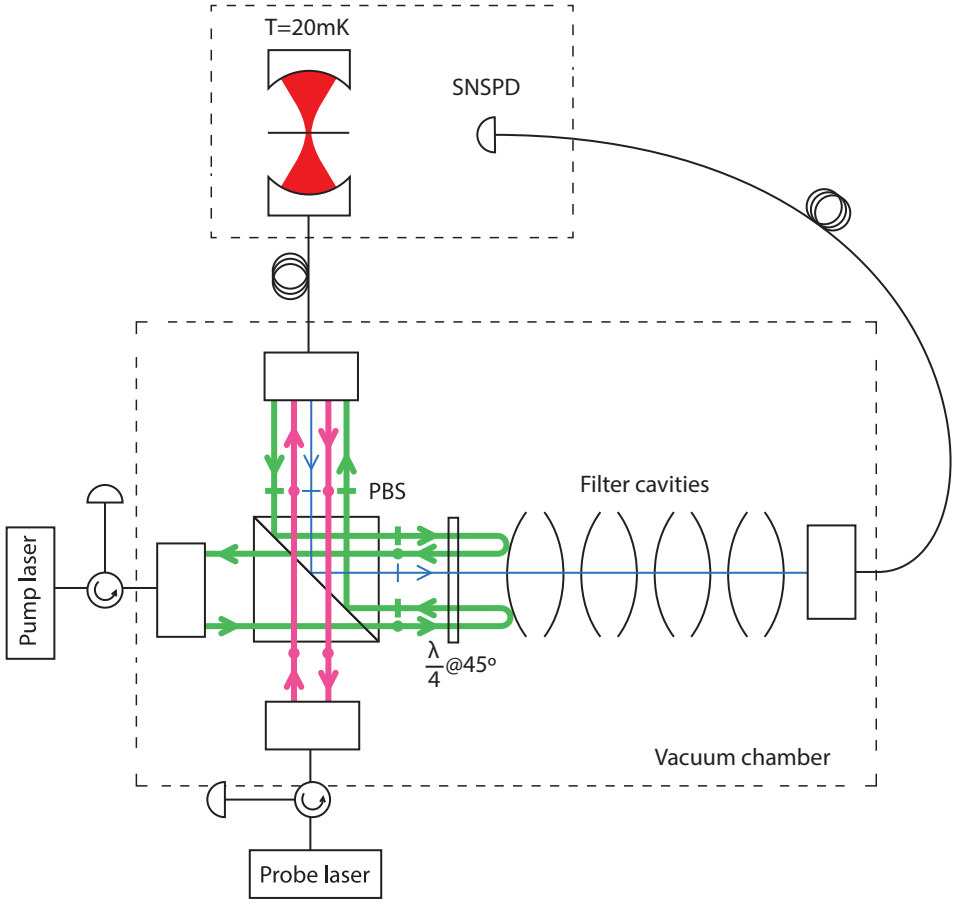

Figure 6.1: Schematics of a quantum optomechanical experiment with detection of a scattered heralding photon, depicted by the blue line. This design maximizes the transmission of the optomechanically scattered photons.

6.1 Filter cavities

6.1.1 Optical design

The inelastic scattering probability P_{scat} of a photon in a cavity with linewidth κ on a phonon is $\propto (g_0/\kappa)^2$, which is typically $10^{-8} - 10^{-6}$ [3, 66], where g_0 is the single-photon optomechanical coupling. Thus the scattered photon at frequency $\omega_{\mathrm{pump}} \pm \Omega_m$ is accompanied by order of $10^6 - 10^8$ pump photons at ω_{pump}, where Ω_m is the mechanical oscillator frequency. Observation of the scattering event re-

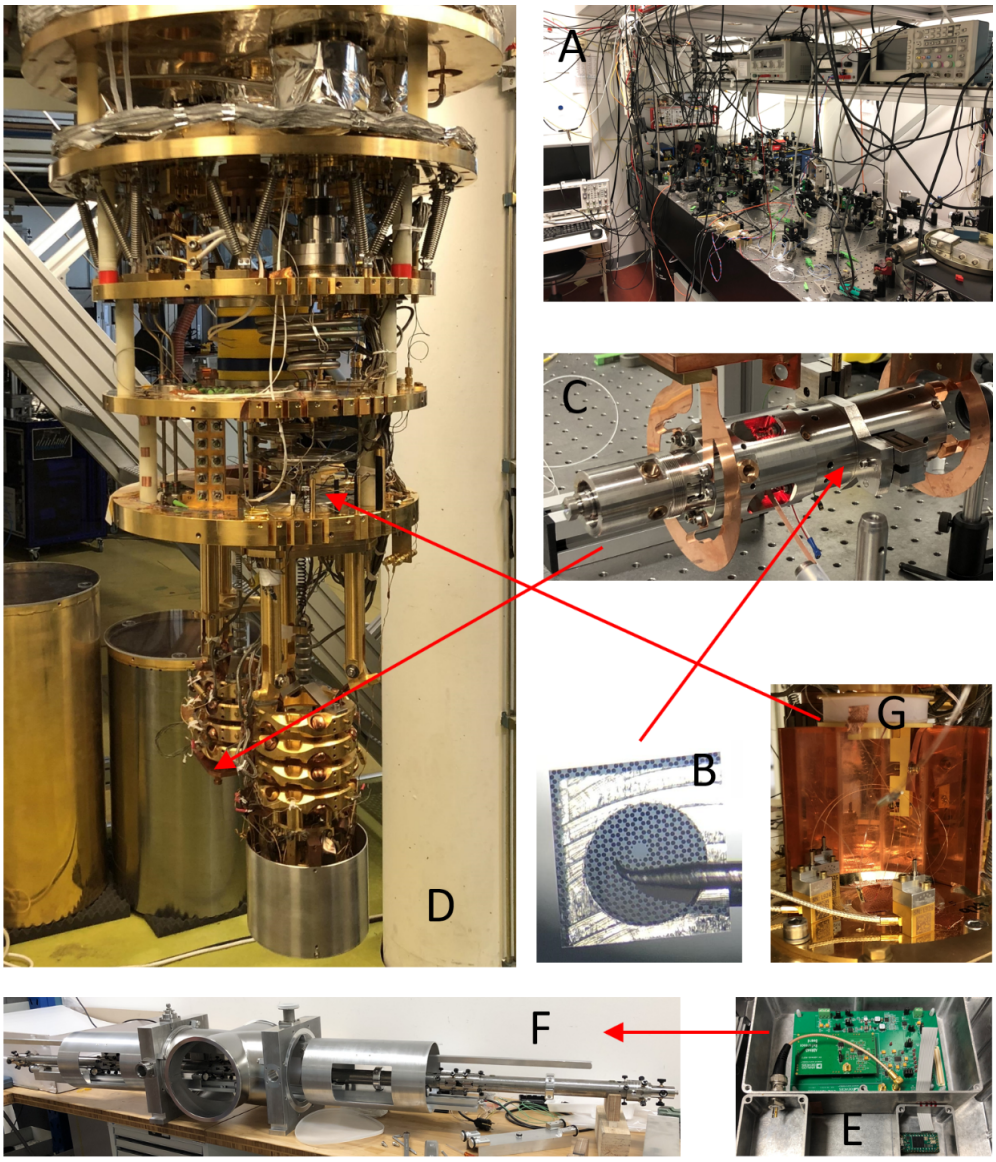

Figure 6.2: All components of the experiment: optical table with lasers (A), membrane (B), cryogenic cavity (C), ultra-low vibration due to the spring-mass mechanical filter dilution cryostat with a nuclear demagnetization stage reaching 1 mK (D), microprocessor control with a low noise digital to analog converter (E) for the filter cavities system (F), single photon detectors (G).

quires an optical filter capable of attenuating the light fields detuned from the filter transmission frequency by Ω_m by much more than $1/P_{\mathrm{scat}}$.

For optomechanical devices operating in the MHz regime it is a challenge to build

such a filter. For example, this would require a Fabry-Perot cavity with a linewidth of ~ 1 Hz causing a delay of about 1 second. In the presence of the cooling light tone the linewidth of the originating anti-Stokes photons will be equal to $\Gamma_{\rm opt} + \Gamma_m$ which is of the order of 100 Hz. Therefore, these photons will be transmitted through the filter with probability ~ 0.01 or less. Another consideration is stability: it is challenging to keep various optical components on resonance with precision of 1 Hz. Nevertheless, the required filter performance can be achieved by concatenating few Fabry-Perot cavities [66].

We adapt and significantly improve upon the filter design presented in [66]. Our filter consists of four consecutive Fabry-Perot cavities (Fig. 6.3) with a linewidth of 30 kHz each. The design transmission of the filter on resonance is ~ 0.85, which is determined by absorption and scattering in the dielectric coatings of the Bragg mirrors and residual reflection from the anti-reflection coatings of the lenses and backside of the mirrors. To achieve this high overall transmission the coatings with < 3 ppm scattering and absorption loss are required. We believe this can be achieved by state of the art supermirrors. We ordered superpolished substrates with surface roughness < 0.1 nm RMS (measured with white light interferometer) and the coatings were deposited using the ion beam deposition technique.

The design filter transmission of light fields detuned by 1 MHz is $< 10^{-14}$, see Fig. 6.4. We consider two optical arrangements with (red lines) and without back-reflection (blue lines) between the cavities.

In the first arrangement there are optical isolators (dotted boxes) making the cavities independent and the overall filter transmission equal to the product of each cavity transmission (red curves on Fig. 6.4). The first optical isolator consists of a polarizing beam splitter (PBS) and a $\lambda/4$ wave-plate at 45^o and accepts linearly polarized light. Light in each cavity is circularly polarized, thus all the subsequent isolators include an extra $\lambda/4$ wave-plate. Altogether there are 26 surfaces in the optical isolators and special care was taken to achieve high transmission through this system. A company Union Optic agreed to pick the best set of the required optical components from their stock achieving the overall transmission of 96% through the whole system of optical isolators (as measured). The overall transmission of the filter is independent of the distance between each two cavities due to the isolators.

If the inter-cavity isolators are removed then the light back-reflected from a cavity starts to interfere with the previous cavity, thus the overall transmission becomes dependent on all the distances between the mirrors. This case was carefully evaluated in [80]. It appears that the transmission as a function of the light detuning Δ can be made $1 - (\Delta/\Delta_0)^8$ for small detuning values $|\Delta/\Delta_0| \ll 1$ having ba-

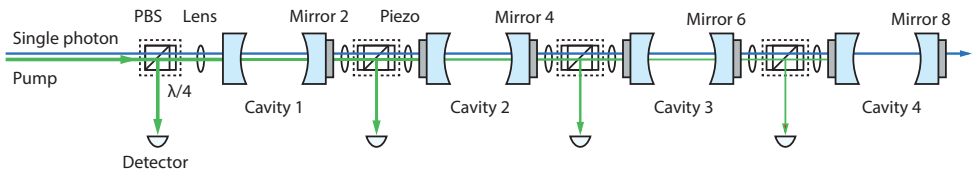

Figure 6.3: Optical setup of the filter. Only Stokes or anti-Stokes photons are transmitted.

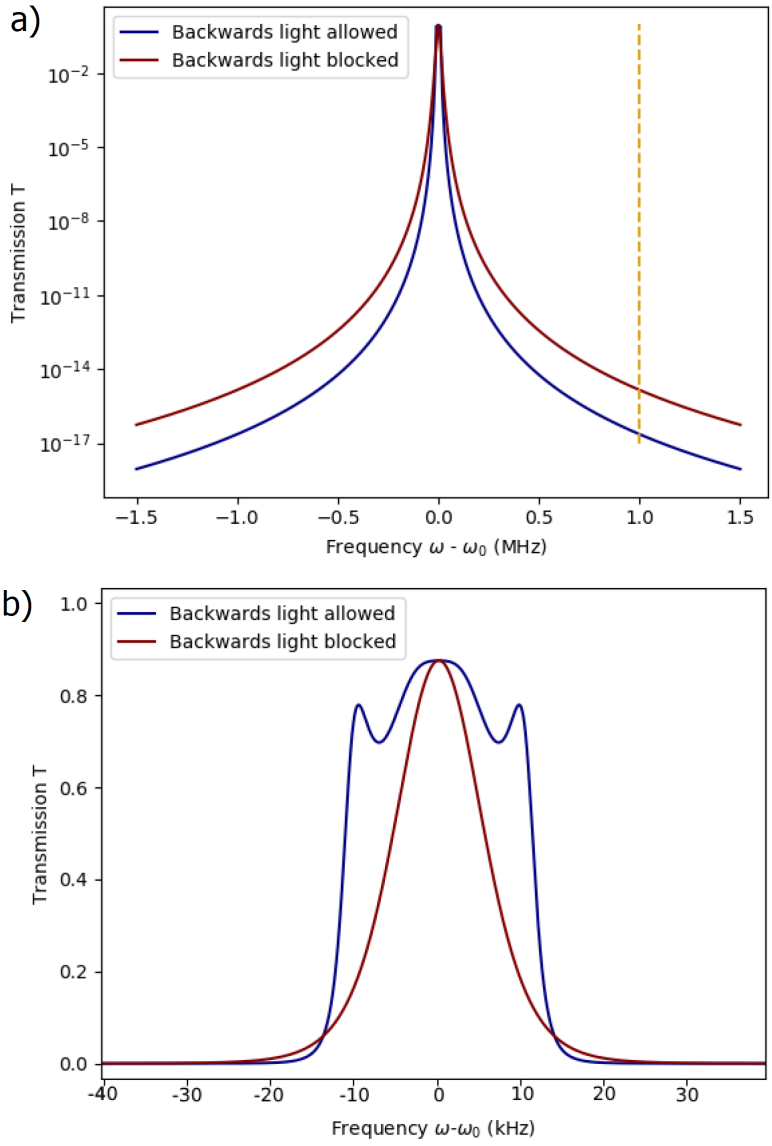

Figure 6.4: Filter transmission with optical isolators (red) and without optical isolators (blue). To achieve the transmission given by the blue line the inter-cavity distances must be controlled within 10 nm. a) shows the transmission for detunings less then 1.5 MHz on a logarithmic scale, b) shows the transmission for detunings less then 40 kHz on a linear scale.

sically a flat top, where Δ_0 is approximately the linewidth of an individual cavity. To achieve this the reflectivities of the mirrors should have specific values with $R_1 = R_8 < R_2 = R_7 < R_3 = R_6 < R_4 = R_5$, where R_i is the reflectivity of mirror

i. Another requirement is that the inter-cavity distances must be set to $n\lambda/2 + \lambda/4$ within 10 nm, where n is an integer number. If the reflectivities are restricted to be equal to have a single coating run, then the transmission curve looses its flat top as shown in Fig. 6.4b). Nevertheless, compared to the case of the system with optical isolators this case has three advantages:
- transmission on resonance is higher due to absence of the loss in the isolators;
- transmission in the vicinity of the resonance is significantly higher. This is beneficial if a scattered photon has some linewidth broadening and/or has random detuning from the resonance due to frequency noise;
- attenuation at 1 MHz detuning is ~ 100 stronger.
The price to pay is that the intercavity distances must be $n\lambda/2 + \lambda/4$ within ~ 10 nm, where n is an integer number. Another, significant complication is the aligning procedure and keeping the cavities resonant to a given frequency.

The filtering system with isolators can be aligned and locked on resonance sequentially using the dither locking technique as the cavities are independent. In the configuration without isolators case the alignment difficulty can be seen from the following. Let's assume the mode matching for the filter cavities is in place and the goal is to keep the four cavities resonant with the laser light. Let's consider mirrors having arbitrary z-axis shifts on the wavelength scale from the optimal resonant configuration. In the case of ideal mirrors with no absorption loss sweeping position of any mirror will have hardly any effect on the reflection signal for almost all mirror positions except for the resonant case of all the four cavities as 100% of light is reflected if at least 1 cavity is off-resonance.

We expect the following alignment procedure to work in the case of no isolators and non-ideal mirrors. For the initial mode matching alignment the cavities might be made independent by inserting optically thin isolators (true zero order $\lambda/4$ wave-plates and film polarizers). After alignment the isolators can be removed not disturbing the mode matching. Alternatively S.L.D. ten Haaf proposed a procedure of making the cavities resonant and setting the proper inter-cavity distances. The procedure is based on non-zero absorption in mirror coatings and can be understood from the following observation. Let's start from arbitrary mirrors positions on the wavelength scale. Simulations show that when mirror2 (see Fig. 6.3) position is swept a measurable reflection dip can be observed when cavity1 becomes resonant with the laser light, Fig. 6.5a). In this case light can propagate further to the space between cavity1 and cavity2 and part of the light is lost due to resonance in cavity1 with absorptive mirrors. The value of this reflection dip is proportional to the absorption loss in the coatings. Next, cavity1 is assumed to be locked on its resonance. A position sweep of Mirror3 has two features, Fig. 6.5b): the reflection signal has a periodic term due to the dependence of the effective reflectivity of the system of mirror2-mirror3 on the distance between these two mirrors and a resonance dip due to cavity2 becoming also resonant with the laser light. It appears that all four cavities can be made resonant and the inter-cavity distances can be set to $n\lambda/2 + \lambda/4$ exploiting similar effects as shown in Fig. 6.5.

Keeping all four cavities on resonance is also a non-trivial task. Modulating mirror2, mirror4, mirror6 and mirror8 positions at different frequencies and demodulating the overall reflection signal at these frequencies provides partial derivatives

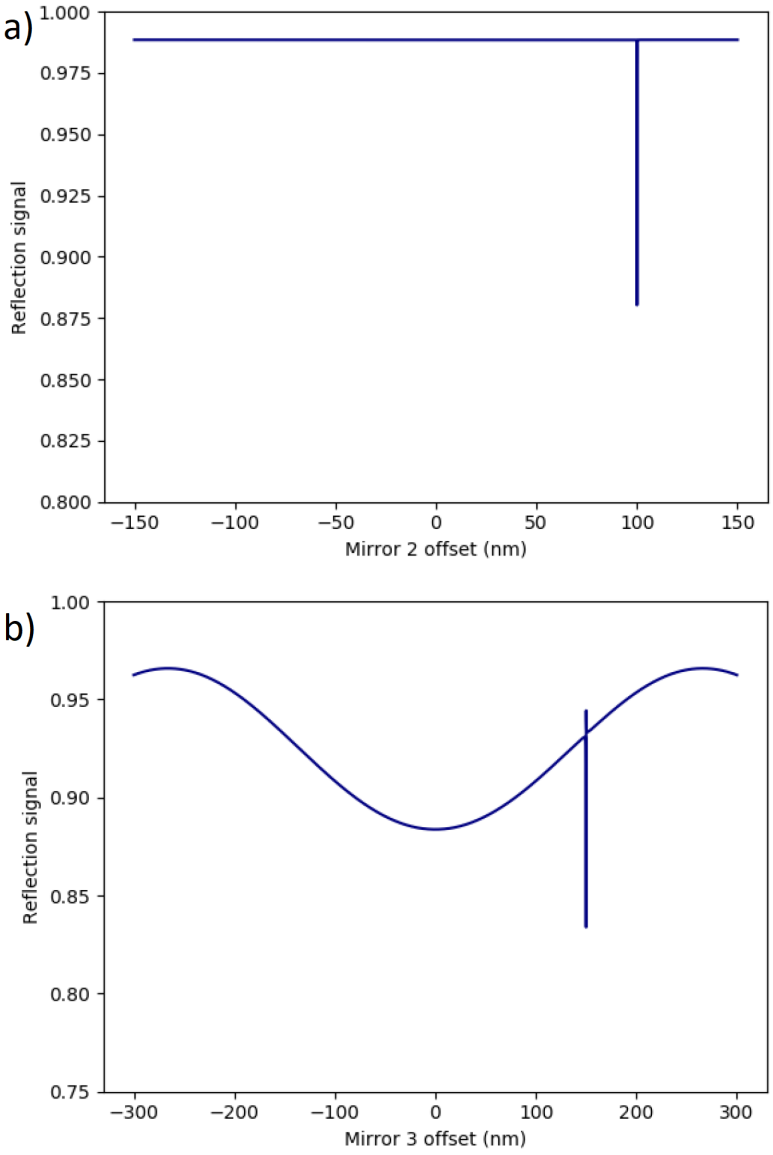

Figure 6.5: Filter reflection when the inter-cavity isolators are removed. a) Mirror2 position sweep with arbitrary other mirrors positions. Mirrors are numbered from left to right, see Fig. 6.3. b) Mirror3 position sweep with cavity1 resonant with the laser light and arbitrary other mirrors positions.

$\frac{\partial R}{\partial L_i}$, where R is the reflection signal and L_i are the i-th cavity lengths. In the configuration with isolators present the values of the derivatives give us full information on how to adjust each mirror position as the shift of mirror i from the ideal position

is directly proportional to $\frac{\partial R}{\partial L_i}$. To achieve the highest transmission of the laser to which the filter cavities are locked all mirrors must be set to their ideal positions, defined such that each individual cavity is on resonance with the incoming light fields. For any other mirrors positions the transmission will be lower. Situation is different in the configuration with no isolators. It appears, that if mirror2 is shifted from the ideal position, the transmission of the laser to which the filter cavities are locked can be restored to practically the same value as the transmission for the case with all mirrors at their ideal positions by adjusting the position of mirror4!

Simulations showed that the second derivatives matrix $\frac{\partial^2 R}{\partial L_i \partial L_j}$ is degenerate in the vicinity of the ideal mirrors positions. This means that observation of the partial derivatives $\frac{\partial R}{\partial L_i}$ does not provide the values ΔL_i - shifts of mirrors 2, 4, 6 and 8 to be corrected. This can be seen from

$$\frac{\partial R}{\partial L_i}(\Delta L_i) = \sum_{j=1}^{4} \frac{\partial^2 R}{\partial L_i \partial L_j} \Delta L_j. \tag{6.1}$$

The vector ΔL_i is not unique because $\left(\frac{\partial^2 R}{\partial L_i \partial L_j}\right)^{-1}$ is not defined. Simulations of a PID control keeping $\frac{\partial R}{\partial L_i} = 0$ shows that the lengths of the cavities do not converge to the mirrors configuration with $\Delta L_i = 0$, see Fig. 6.6. This confirms that there are non-zero mirrors position shifts ΔL_i for which $\frac{\partial R}{\partial L_i} = 0$.

Two solutions to this very challenging problem have been proposed. In the first one the shape of the transmission curve is taken as an additional input and a trained neural network finds the resonant situation for all four cavities. The second one is based on mechanical insertion of the inter-cavity isolators to make the cavities independent, adjust the cavity lengths appropriately and remove the isolators afterwards every few seconds. This can be achieved by a mechanism with step motors placing the isolators on the optical path and removing them after a short time enough for readjustment.

6.1.2 Mechanical design of filter cavities

The mechanical design is based on the cryogenic cavity design (see Fig. 6.7) as it demonstrated an ability to reach 96% optical coupling to a single mode fiber and very stable in time performance (optical coupling deteriorates by less than 1% during a couple of months at room temperature). The cryogenic cavity and the filter cavities together with its support were developed in close collaboration with Harmen van der Meer at the fine mechanical department of LION.. The fiber incoupling module and the first cavity are identical to the cryogenic cavity except for the cavity being 40 cm long. Each inter-cavity module holds 2 mode-matching lenses and an optical isolator ($\lambda/4$ waveplate at 45^o, PBS, $\lambda/4$ at waveplate 45^o). The light reflected from the next cavity is reflected by the PBS cubes and monitored by the photodiode.

In Fig. 6.1 all the four ports of the first PBS are used, this is planned to be implemented in the next iteration of the filter cavities system.

The whole setup of the filter cavities is about 2 m long and 5 cm in diameter resulting in high aspect ratio, thus it cannot be supported at two points. Multiple

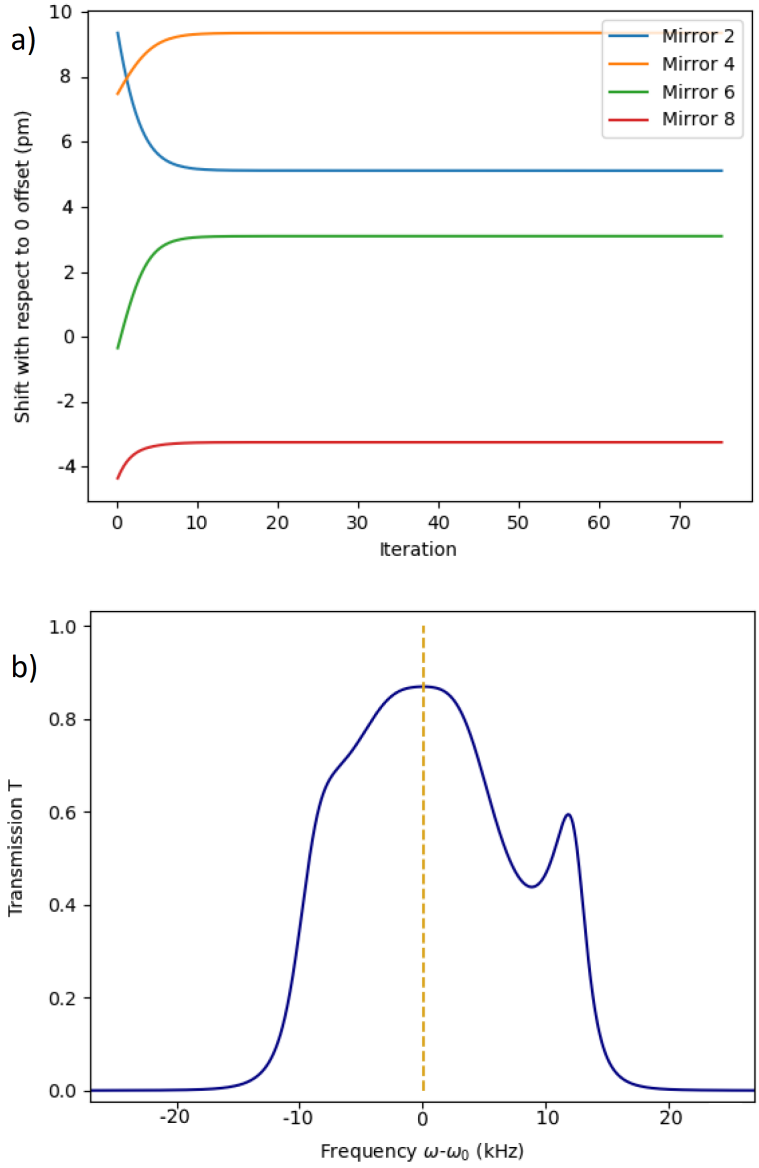

Figure 6.6: PID feedback control starting from a random state with non-zero demodulated signal proportional to $\frac{\partial R}{\partial L_i}$ and adjusting ΔL_i to reach a state with $\frac{\partial R}{\partial L_i} = 0$. a) The derivatives converge to 0. b) The total transmission of the final state.

point support is also not ideal as any aging effect in the support (rubber parts for example) will lead to support force redistribution and bending of the whole structure and misalignment as a result. To address these issues we developed a special support designed to hold each cavity with a constant force, see Fig. 6.8. The support

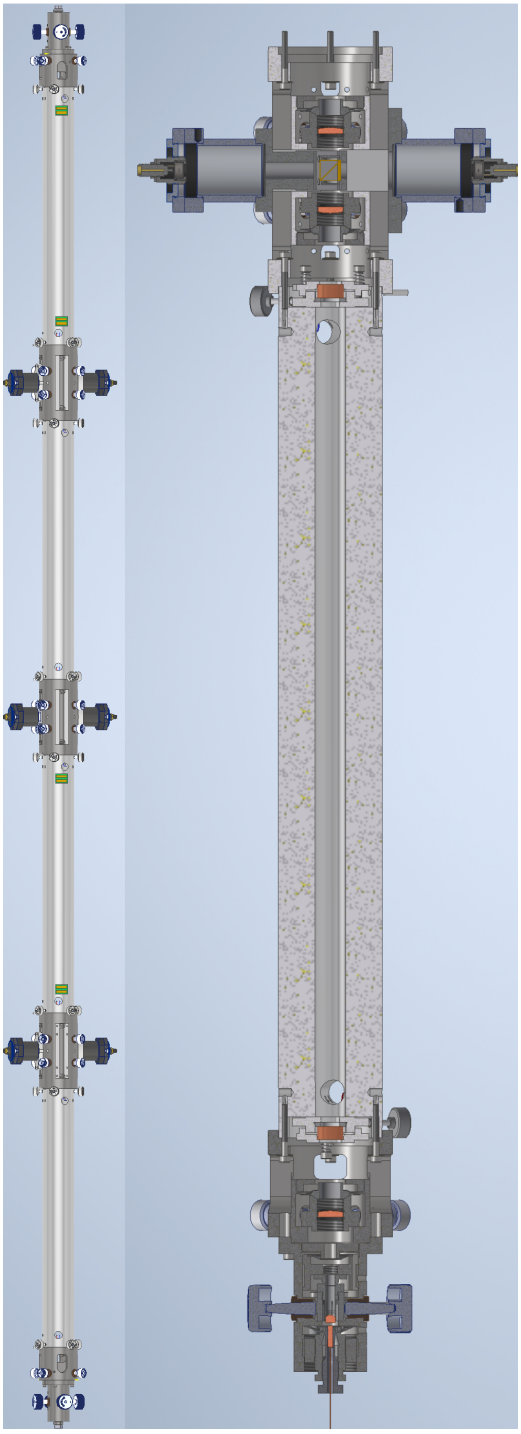

Figure 6.7: Mechanical design of the filtering cavities. All four cavities are arranged consecutively, left sketch. Right sketch shows the fiber incoupling together with the first cavity and an intercavity module containing mode matching lenses and an optical isolator.

consists of multiple moving parts connected by rubber rings. Rubber rings serve as springs with damping to create a multi-stage mechanical low pass filter. Each cavity is supported by an A-type piece held by B-type pieces in their centers such that A parts can rotate. The same holds for B parts. By design the force at all points holding the cavities are equal which is easy to see considering torque balance in the system. As a result if some rubber joint shrinks due to aging the whole system will adjust itself to restore the torque balance via force equality. We believe that this design of the support should benefit to the time stability of the optical alignment.

Figure 6.9 shows a photo of the filter cavities system together with the support assembled without optics. The C-type part is fixed inside the central part of the vacuum chamber, the B-type parts are represented by the two pieces of a tube with openings. The four A-type parts are also partly visible on the photo. After the optical alignment is done two large vacuum caps are attached from the sides and pressed against the large o-rings visible on the photo. The central part is closed by two blank flanges. Vacuum is maintained by an ion pump. There is a vacuum feedthrough for the fibers. The fiber going to the single photon detector is placed in a vacuum tight system of tubes connecting the filter vacuum chamber and the cryostat to ensure complete stray light isolation.

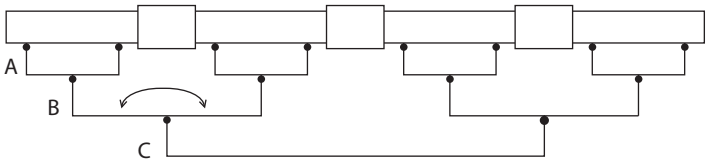

Figure 6.8: Constant force support design. The black circles represent joints free to rotate as shown by an arrow. The C part is fixed. Two B parts and four A parts can be rotated around their centers. This design ensures equal force support at each point holding the cavities.

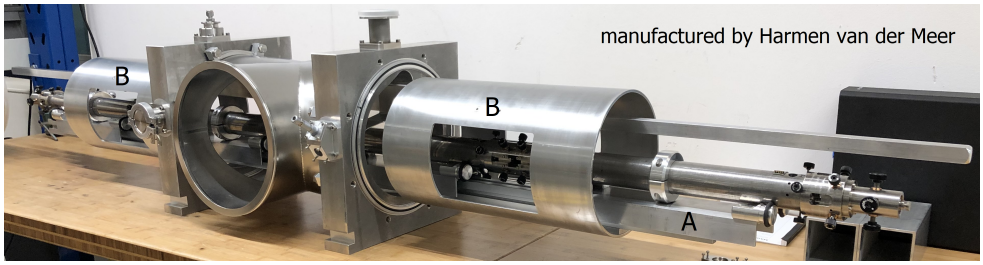

Figure 6.9: Photo of the support for the filter cavities holding the filter cavities. Each cavity is supported at two points of contact (black rubber rings) one of them is visible on the right side of the most right cavity. Moving parts A type and B type corresponding to Fig. 6.8 are marked with letters A and B. The C part is fixed to the central part of the vacuum chamber visible on the photo. After optical alignment is done vacuum caps are added on both sides to the large o-rings visible on the photo.

6.1.3 Control design

During the actual experiment we want to monitor for optomechanically scattered photons, thus the filter cavities must be resonant with these photons. To keep the filter cavities resonant some probe light should be transmitted through these cavities to monitor and subsequently being able to piezo adjust their lengths. But any transmitted light will reach the single photon detector, so these two requirements cannot be fulfilled simultaneously. Thus the experiment is organized in cycles: during the first part of each cycle (~ 0.1 s) the optical path towards the single photon detector is blocked not to blind the detector and the filter cavities are made resonant at the frequency of interest; during the second part of each cycle the feedback for filter cavities is frozen, the cavities probe light is switched off and the blocking is removed for optomechanical measurements (~ 1 s).

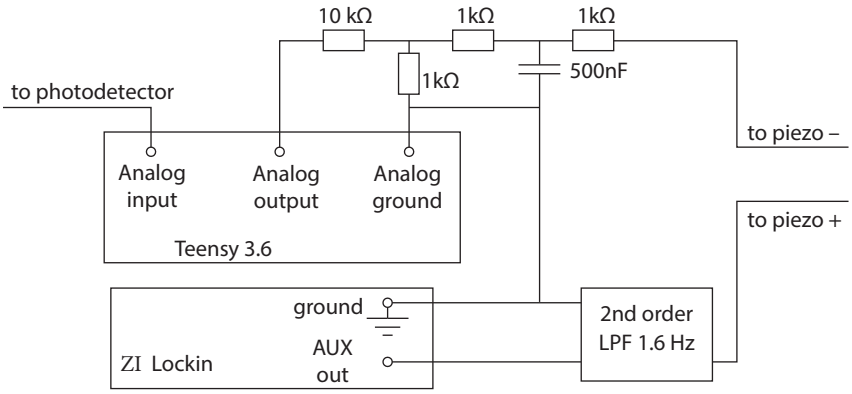

Figure 6.10: Electronic circuit used to keep each filter cavity locked to the laser light frequency. The Teensy 3.6 microprocessor modulates the piezo, demodulates the reflection signal and provides PID feedback signal.

In the actual experiment there are the following components which should be frequency locked: cryogenic cavity, filter cavities, probe and pump laser light fields. One possibility is to lock all the components to the cryogenic cavity as it might seem to be the quietest. But it is not the case: the pulse tube shakes the whole cryostat and modulates the cryogenic cavity resonance frequency by ~ 300 kHz (~ 0.1 nm) at multiple frequencies. The goal is to be able to freeze the feedback signal keeping the filter cavities resonant to the cryogenic cavity. The cryogenic cavity can be probed at all times, while the filter cavities cannot be observed during the collection of Stokes and anti-Stokes photons. Therefore we decided to introduce a stable narrow-linewidth reference cavity to which everything is locked. In the Fig. 6.12 we show that we indeed can freeze the feedback signal to filter cavities and they remain resonant with the reference cavity during a couple of seconds.

First, the probe filter cavity laser is locked to this reference cavity (9 kHz linewidth) via Pound-Drever-Hall technique.

Next, we demonstrate locking of a single test filter cavity (~ 20 kHz linewidth) to the reference cavity. The reference cavity and the test cavity are in separate vacuum

chambers. The locking is achieved by the dither locking technique: the length of the cavity is modulated by a piezo at 2 kHz, reflection signal is demodulated at the same frequency resulting in the derivative of the reflection signal with respect to the cavity length. This demodulated signal is used as an error signal for a PID feedback control. All these steps are done by a microprocessor connected to analog to digital (ADC) and digital to analog (DAC) converters [81]. The main requirement is that we should be able to scan 1 FSR (~ 50 V on piezo) and the voltage on the piezo should be stable to within a fraction of the filter cavity linewidth (~ 50 μV on piezo) during the freezing stage to guarantee close to unity transmission.

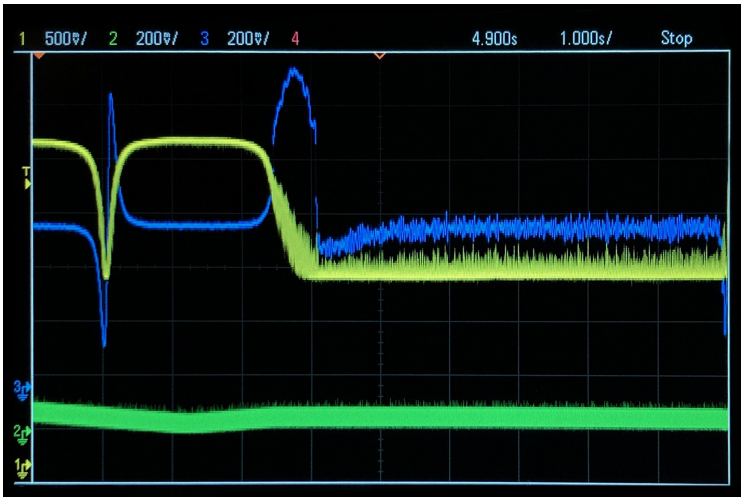

Figure 6.11: Locking a single test filter cavity with linewidth of ~ 20 kHz. Yellow trace shows reflection signal, blue trace shows the demodulated signal (PID error signal) and green trace shows the microprocessor output voltage before filtering and attenuation. First the voltage is swept across the cavity resonance, then the direction of the voltage change is reversed. When the reflection signal drops below a certain threshold approaching the cavity resonance, the rate of the voltage change is decreased 10 times. When the reflection signal reaches the next threshold the scanning is switched off and the feedback control is enabled.

In this proof of principle experiment we use a DAC of a Zurich Instruments lock-in as a source of stable voltage having a voltage range of -10..10 V. It's enough for a single cavity as it's always possible to find such a resonance of the reference cavity that the required voltage on the piezo of this test cavity is within range due to the cavities having different lengths (20 cm and 7 cm). This voltage is applied to the positive lead of the test cavity piezo passing through a low-pass filter, see Fig. 6.10. For this test we are using a Teensy 3.6 microprocessor having built-in 14 bit ADC and DAC with a range from 0 to 3 V for both of them. We assume that the noise of this DAC is of the order of the least significant bit (LSB), which is 200 μV. To satisfy our requirement for voltage stability of 50 μV we use a voltage divider 1:10 consisting of 1 kΩ and 10 kΩ resistors. This brings the low frequency noise of the DAC down to ~ 20 μV. This signal is sent to the negative lead of the piezo after passing through another low-pass filter (2nd order with the corner frequency of 20 Hz).

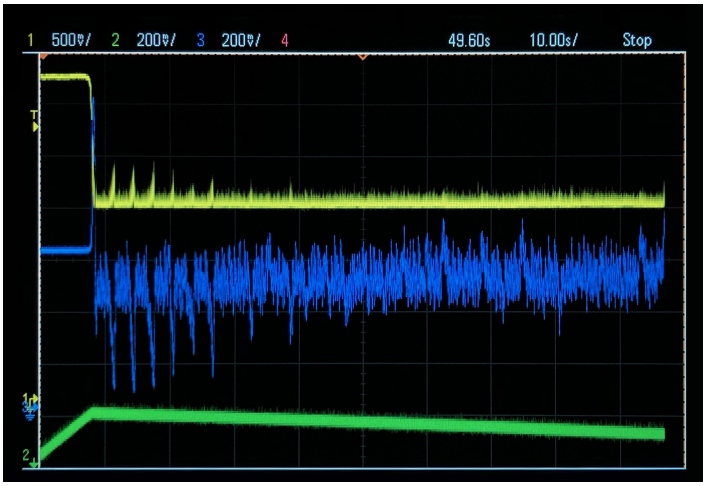

Figure 6.12: Repetitive cycles of 2 s locking and 1 s freezing the feedback voltage. During the first few cycles the system drift is not compensated, which is visible during the PID freeze states when the error signal monotonically decreases. Another PID feedback compensates for the drift. Just after locking the drift is not fully compensated as the integral part of the PID has not reached the steady state yet. The drift becomes fully compensated after $\sim$ 1 minute. The system reaches the steady state after $\sim$ 10 minutes.

Modulation signal of $\sim$ 50 μV pk-pk at 2 kHz is applied to the negative piezo lead, reflection light is detected by a photodetector, its output is sent to the ADC of the microprocessor. The demodulated signal is shown on Fig. 6.11 by the blue trace. The oscilloscope operates in the peak-detect mode. Here the cavity is scanned first, and then the PID feedback is switched on when the reflection signal is close to its minimum value.

Next we realize the freeze-lock cycles. After each lock period of 2 s the PID feedback is frozen for 1 s, see Fig. 6.12. Significant drift is present in the frequency difference of the filter cavity and the reference cavity which is visible in the first few lock-freeze cycles. To compensate for this drift another PID loop is realized (with an integral component only) which takes the first PID correction signal accumulated over a cycle as an error signal. This double-integrating scheme is able to keep the test filter cavity on resonance with the reference cavity for at least 30 s in this compensated freeze state.

To improve the transmission of the filter cavity even further and to cover the full FSR we will use a state-of-the-art 20 bit DAC instead of the built-in Teensy 3.6 DAC for the fine control of the piezo voltage and another 20 bit DAC output amplified 3 times using a zero drift operational amplifier for the coarse voltage control.

6.2 Single photon detectors

Scattered photons created in the optomechanical interaction inside the cryogenic cavity, travel through the filter cavities and finally are detected by a superconducting nanowire single photon detector (SNSPD). We tested four SNSPDs purchased from Photon Spot, optimized for 1064 nm. Each detector contains a SiW nanowire having a meander shape and covering an area of 20x20 μm^2. The bias current is sent through the DC port of a bias-T to the nanowire so that the nanowire is in the superconducting state close to its critical state. Absorption of a photon by the nanowire leads to creation of a hotspot - a small region with non-equilibrium state of electrons. This does not happen by direct heating above the critical temperature [83]. This breaks the Cooper pair locally creating a non-superconducting island in the nanowire. This, in turn, increases the current density above the critical value in the remaining superconducting part around the hotspot which in the end makes a piece of the nanowire to be in the normal state. This leads to an abrupt increase of the nanowire resistance to about 1 $k\Omega$ creating a voltage spike due to the nanowire inductance. The voltage spike travels to the bias-T and exits through its radio frequency port and is subsequently amplified and measured, see Fig. 6.13.

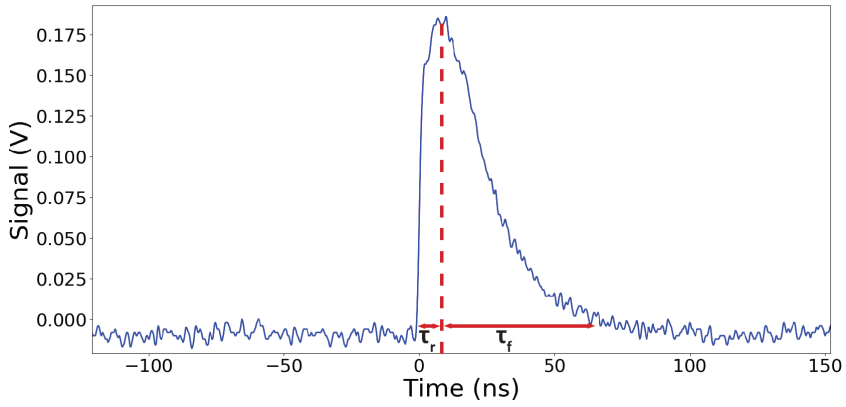

Figure 6.13: Signal resulting from detection of a single photon. Rise and fall times are denoted by arrows.

The detectors were installed in the cryostat and were calibrated using the procedure described in [84]. Laser light was split by a calibrated beamsplitter (BS). One output of the BS was measured by a powermeter, the other output was sent through two electronic variable optical attenuators to each detector. The BS and attenuators were single-mode fiber coupled. The detection efficiency of three detectors was measured as a function of the bias current, see Fig. 6.14. The system detection efficiency (SDE) is defined as the ratio of the number of clicks produced by the detection electronics and the number of photons entering the fiber attached to the detectors. Two detectors were measured to have SDE of the exceptional value of $95\% \pm 7\%$, and one of them will be used in the future quantum optomechanical experiments.

Another important characteristics of a single photon detector relevant to the pro-

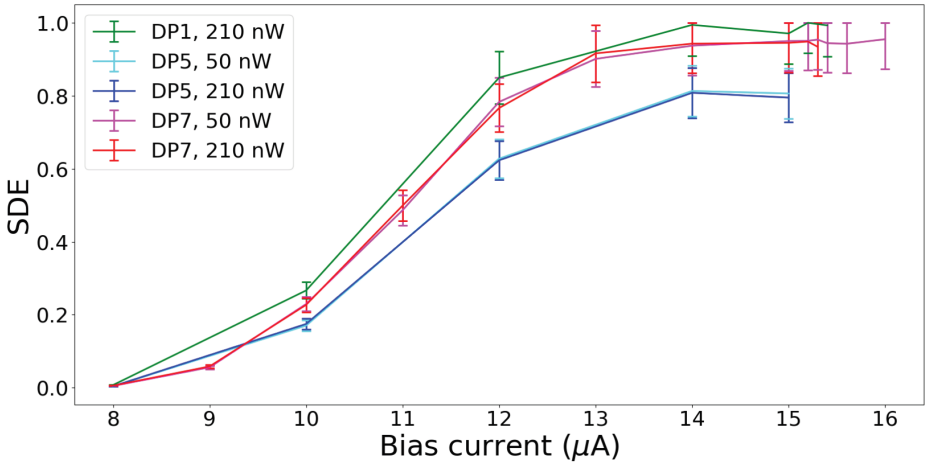

Figure 6.14: Measured system detection efficiency of superconducting nanowire single photon detectors. The efficiency depends on the bias current flowing through the nanowire. The detectors were illuminated by two different light intensities, 50 nW and 210 nW before the attenuation or $\sim 0.5 \times 10^5$ and $\sim 2 \times 10^5$ photons per second on the detectors.

tocol described in Chapter 4 is the dark count rate (DCR), meaning the rate at which a detector clicks without photons to be detected launched into the fiber. These detectors appeared to be extraordinary also from this point of view. The fourth detector was kept in the dark (no fiber attached) thermalized at 20 mK. The dark count click rate is ~ 0.3 mHz - on average we observed ~ 1 click per hour. The other three detectors with optical fibers leaving the cryostat were measured to have DCR of ~ 10 mHz. The increased DCR of these detectors might be explained by the black body radiation of the fiber segments kept at room temperature. We found that the click rate we were detecting with no light sent to the detectors heavily depended on the shielding of the detector fibers from the stray light. The smallest rate of DCR (~ 10 mHz) was observed when the fibers leading to the detectors were placed in a vacuum-tight metal tubing outside the cryostat. This guaranteed no stray light entering the fibers.

Acknowledgements

The results in sections 6.1.1 and 6.1.2 are part of the M.Sc. thesis of S.L.D. ten Haaf. The research was conducted together with and under the daily supervision of Vitaly Fedoseev. Figures 6.4, 6.5 and 6.6 were prepared by S.L.D. ten Haaf.

The results in section 6.1.3 are part of the B.Sc. thesis of O. Huisman. The research was conducted together with and under the daily supervision of Vitaly Fedoseev.

The results in section 6.2 are part of the M.Sc. thesis of R. Claessen. The research was conducted together with and under the daily supervision of Vitaly Fedoseev. Figures 6.13 and 6.14 were prepared by R. Claessen.

7 Mechanical ground state

In section 1 of this chapter we consider the requirements for our optomechanical system to measure the average phonon number of a thermal state of a mechanical mode close to its ground state by observing the Stokes and Anti-Stokes sidebands asymmetry.

In section 2 an experiment is proposed to investigate membrane heating due to the intracavity light fields at low temperatures.

7.1 Requirements

In most quantum optomechanical experiments it is desirable to initialize the mechanical oscillators in their quantum ground state. Therefore, it is essential to know the average phonon occupation $\bar{n}$ of the mechanical modes when they are prepared in a thermal state close to the ground state. One of the known methods of $\bar{n}$ determination is via the sideband asymmetry [9]. This method is based on the different boson enhancement factors of the scattering probabilities $\gamma_{n\to n+1}$ and $\gamma_{n\to n-1}$ of the transition rate between phonon levels n and $n \pm 1$ as mentioned in Chapter 1. The different prefactors lead to the different prefactors of the Stokes and anti-Stokes scattering rates:

$$\Gamma_{\mathrm{S}} = (\bar{n}+1) g_0^2 n_{\mathrm{cav}} \frac{\kappa}{\omega_m^2}, \tag{7.1}$$

$$\Gamma_{\mathrm{AS}} = \bar{n} g_0^2 n_{\mathrm{cav}} \frac{\kappa}{\omega_m^2}, \tag{7.2}$$

where g_0 is the single photon optomechanical coupling rate, n_{cav} is the intracavity photon number, κ is the optical decay rate and ω_m is the frequency of the mechanical mode.

In any measurement the field probe should be weak in order to not disturb the system too much. It's known that high intracavity light fields cause heating of the optomechanical devices. Therefore, we are finding the minimal probe intensity to

measure the thermal state of a mechanical mode close to its ground state via the sideband asymmetry. We are considering a defect mode of our phononic crystal membranes in a cavity with parameters of the cryogenic cavity discussed in Chapter 5. The settings are [9]:
- the membrane is optomechanically coupled with $g_0/2\pi = 1$ Hz (this is what we observe for our 10 cm cavity); the membrane temperature is 1 K, cavity linewidth $\kappa/2\pi = 50$ kHz;
- a strong pump is sent on the red-sideband to cool a high-Q mechanical mode ($\omega_m/2\pi = 1.3$ MHz, $Q = 10^9$) to a thermal state with $\bar{n}_f = 0.1$;
- a probe is sent on cavity resonance to measure the thermal state of the mechanical mode;
- the probe sidebands are detected via heterodyning on a shot-noise limited balanced photodetector with ideal mode overlap;
- all optomechanically scattered photons reach the photodetector: $\kappa_{\rm ext} = \kappa$.

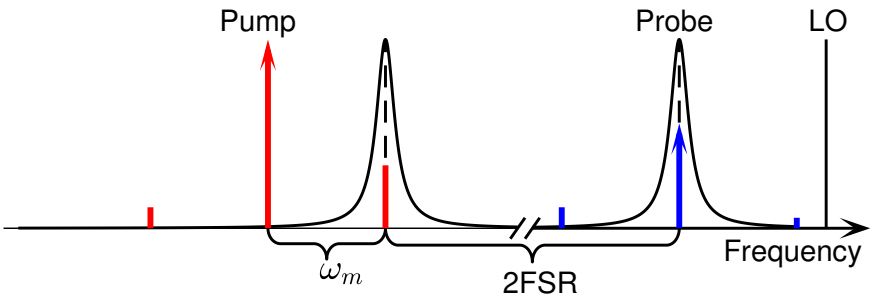

Figure 7.1: Sideband cooling experiment with resonant probe. The Stokes and Anti-Stokes sidebands from the resonant probe are detected via heterodyning with local oscillator (LO), the ratio of the sidebands provides information of the thermal state of the mechanical mode.

To do the measurement both sidebands must be observable above the shot-noise with signal to noise ratio of at least $r_{\rm signal/noise} = 0.1$ (which is measurable [65, 64]) for the power spectral density.

Let's start with the required cooling light intensity to reach $\bar{n}_f = 0.1$. Using

$$\bar{n}_f = \frac{\Gamma_{\rm opt}\bar{n}_{\rm min} + \Gamma_{\rm m}\bar{n}_{\rm th}}{\Gamma_{\rm opt} + \Gamma_{\rm m}}, \tag{7.3}$$

where $\bar{n}_{\rm min} \approx \kappa^2/16\omega_m^2$, we can estimate the required $\Gamma_{\rm opt} \approx \frac{k_B T}{\hbar Q}\frac{1}{n_f}$, $\Gamma_{\rm opt}/2\pi = 220$ Hz. The rates of Stokes and anti-Stokes scattering for the resonant probe are

$$\Gamma_{\rm S} = (\bar{n}_f + 1)g_0^2 n_{\rm cav.probe}\frac{\kappa}{\omega_m^2}, \tag{7.4}$$

$$\Gamma_{\rm AS} = \bar{n}_f g_0^2 n_{\rm cav.probe}\frac{\kappa}{\omega_m^2}, \tag{7.5}$$

where $n_{\rm cav.probe} = \frac{4P_{\rm probe}}{\kappa\hbar\omega_L}$. The weaker anti-Stokes sideband has the Lorentzian lineshape with linewidth $\Gamma_{\rm opt}$ due to scattering with the mechanical mode cooled by

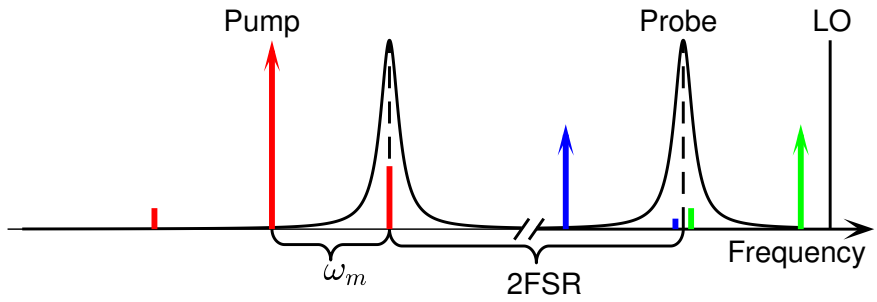

Figure 7.2: Sideband cooling experiment with two off-resonant probes. The probes are detuned by $\Delta = \pm(\omega_m + \delta)$ such that the Stokes and anti-Stokes sidebands are separated by more than $\Gamma_{\rm opt}$ to avoid interference between them. $\Gamma_{\rm opt} \ll \delta \ll \kappa$.

the pump light fields. The intensity of the anti-Stokes sideband is $I_{\rm AS} = \Gamma_{\rm AS}\hbar\omega_L = \bar{n}_f \frac{4g_0^2}{\omega_m^2} P_{\rm probe}$. Such a signal will have the following spectrum:

$$I_{\rm AS}(\omega) = \frac{1}{2\pi} \frac{\Gamma_{\rm opt}}{(\omega - \omega_{\rm AS})^2 + \Gamma_{\rm opt}^2/4} I_{\rm AS}, \tag{7.6}$$

which means $I_{\rm AS} = \int_{-\infty}^{\infty} I_{\rm AS}(\omega)\, d\omega$.

Interference of this sideband with a local oscillator with intensity $I_{\rm LO}$ and frequency $\omega_{\rm LO}$ on a balanced photodetector will result in the difference signal

$$2\sqrt{I_{\rm LO} I_{\rm AS}} \sin{(\omega_{\rm LO} - \omega_{\rm AS})t}. \tag{7.7}$$

The frequency of the local oscillator is chosen such that in the range of frequencies around $|\omega_{\rm LO} - \omega_{\rm AS}|$ the balanced photodetector is shotnoise limited.

The power spectral density of this signal will be

$$I_{xx}(\omega) = 2 I_{\rm LO} I_{\rm AS}(\omega) \tag{7.8}$$

with the maximum value

$$I_{xx,{\rm signal}}(\omega_{\rm AS}) = I_{\rm AS} \frac{2}{\pi \Gamma_{\rm opt}}. \tag{7.9}$$

This should be $r_{\rm signal/noise}$ of the shot noise power spectral density $I_{xx,{\rm SN}} = 2\hbar\omega_L I_{\rm LO}$:

$$I_{xx,{\rm signal}}(\omega_{\rm AS}) = r_{\rm signal/noise} I_{xx,{\rm SN}} \tag{7.10}$$

resulting in

$$\Gamma_{\rm AS} = \frac{r_{\rm signal/noise}\pi}{2} \Gamma_{\rm opt}. \tag{7.11}$$

We see that $I_{\rm LO}$ drops out. Using the expressions for $\Gamma_{\rm opt}$ and $\Gamma_{\rm AS}$ we obtain

$$P_{\rm probe} = \frac{r_{\rm signal/noise}\pi}{8} \frac{k_B T \omega_L}{Q} (\frac{\omega_m}{g_0})^2 \frac{1}{\bar{n}_f^2}. \tag{7.12}$$

For the given physical properties this will result in $P_{\mathrm{probe}} \approx 0.2$ mW.

This probe power will result in the intracavity photon number 3×10^4 times higher than the intracavity photon number due to the cooling pump light and will provide the dominant heat load on the membrane. Therefore, we conclude that observation of the sideband asymmetry of a resonant probe is not practical for our system parameters.

The intracavity photon number due to the probe can be minimized by introducing a pair of equal intensity light tones with detunings $\Delta = \pm(\omega_m + \delta)$ instead of a resonant probe [85], where $\Gamma_{\mathrm{opt}} \ll \delta \ll \kappa$. Taking into account the expression for the anti-Stokes scattering rate with an arbitrary detuning Δ

$$\Gamma_{\mathrm{AS}} = \bar{n}_f g_0^2 n_{\mathrm{cav.probe}} \frac{\kappa}{\kappa^2/4 + (\Delta + \omega_m)^2}, \tag{7.13}$$

the intracavity photon number $n_{\mathrm{cav.probe}}$ for the case of the two off-resonant probes will decrease $\frac{4\omega_m^2}{\kappa^2}/2 = 1300$ times. Even in this case the intracavity photon number due to the probe will be approximately 20 times higher than the intracavity photon number due to the cooling light fields. Therefore, the temperature of the membrane might increase when the probe light is introduced resulting in an increase of $\bar{n}_f$.

To make the membrane heating effect of the probe light small compared to the sideband cooling the single photon detection scheme discussed in the previous chapter can be used. In this case the reflected light is sent through the filtering system tuned to the right cavity resonance shown in Fig. 7.2 towards the single photon detector. Instead of the two off-resonant probes only one probe is used at a time. First, the probe with intensity $1/10$ of the cooling light fields and $\Delta = +\omega_m$ detuning is sent to the cavity and the Stokes rate $\Gamma_{\mathrm{S},1}$ is measured, then the same intensity probe and $\Delta = -\omega_m$ is sent and the anti-Stokes rate $\Gamma_{\mathrm{AS},1}$ is measured. The intracavity photon number due to these probe light fields will be $1/10$ of the intracavity photon number due to the cooling light fields. The expected scattering rates will be:

$$\Gamma_{\mathrm{S},1} = 150 \text{ Hz}, \tag{7.14}$$

$$\Gamma_{\mathrm{AS},1} = 13 \text{ Hz}. \tag{7.15}$$

The measured dark count rates of our single photon detectors are approximately 0.01 Hz making the expected rates possible to measure.

7.2 Membrane thermometry via Anti-Stokes sideband

The main uncertainty of the sideband asymmetry experiment and the quantum STIRAP experiment is how much the membrane is heated due to the strong driving light fields. It is important for two reasons: first, the time of one phonon to enter the mechanical mode from the environment is proportional to the temperature of the environment. Second, it was demonstrated [86] that the quality factor of a SiN membrane increases factor of ~ 4 upon cooling the membrane from 1 K to the dilution fridge temperature.

Here we will show that by measuring the anti-Stokes scattering rate it is possible to determine the dependence of the membrane temperature T_{env} on the intracavity

photon number. Let's consider an experiment where only the cooling light fields

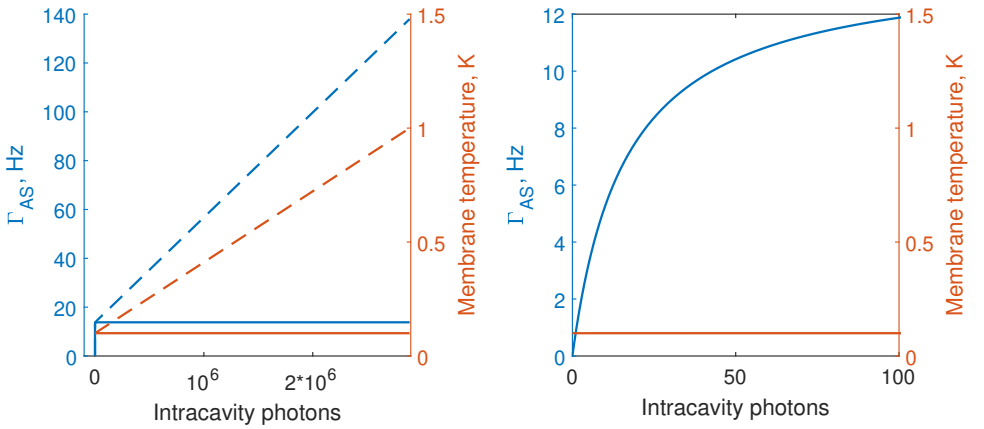

Figure 7.3: Anti-Stokes scattering rate used for thermometry. The left plot shows the scattering rate and the membrane temperature in the absence of membrane heating due to the pump light (solid lines) and in the presence of the heating (dashed lines). The membrane temperature is assumed to be proportional to the intracavity photon number. The right plot shows the scattering rate and the membrane temperature for low intracavity photon numbers. 2.9×10^6 intracavity photons result in $g/2\pi = 1.7$ kHz and $\bar{n}_f = 0.1$. For large intracavity photon numbers the scattering rate is proportional to the membrane temperature and can be used for direct thermometry.

with detuning $\Delta = -\omega_m$ are present. In the sideband-resolved regime the anti-Stokes scattering rate will be

$$\Gamma_{\mathrm{AS}} = \frac{k_B T_{\mathrm{env}}}{\hbar Q (1 + \frac{\omega_m \kappa}{4 Q g_0^2 n_{\mathrm{cav}}})}. \tag{7.16}$$

The dependence of Γ_{AS} on the intracavity photon number is shown in Fig. 7.3 by the blue solid line. For $n_{\mathrm{cav}} \gtrsim 1000$ Eq. 7.16 becomes independent of n_{cav}:

$$\Gamma_{\mathrm{AS}} \approx \frac{k_B T_{\mathrm{env}}}{\hbar Q}. \tag{7.17}$$

In this case the anti-Stokes scattering rate is directly proportional to the physical temperature of the membrane T_{env}. Here we assume that $Q = \mathrm{const}$. If the quality factor changes with temperature, than it can be measured independently via a mechanical ringdown. In the presence of membrane heating due to the intracavity light the anti-Stokes scattering rate will increase with the increase in the pump light intensity as shown by dashed lines in Fig. 7.3. Here we assumed direct proportionality between the temperature increase and the intracavity photon number with the membrane temperature being equal to 1 K for intracavity photon number necessary to reach $\bar{n}_f = 0.1$.

By choosing a membrane mode with not too high quality factor such an experiment is feasible even with a heterodyne detection scheme.

7.3 Conclusions

We analyzed the possibility to find the average phonon ocupation $\bar{n}$ of a mechanical mode by measuring the sideband asymmetry for our system using a balanced photodetector. It was supposed that the membrane is thermalized to a bath with $T = 1$ K and a strong enough pump light fields are used for the sideband cooling to reach $\bar{n} = 0.1$. It was found that if a single probe resonant with the cavity is used with light intensity high enough to do the sideband asymmetry measurement then the intracavity photon number due to the probe will be 3×10^4 times higher than the intracavity photon number due to the cooling light fields which already might cause heating of the membrane. Such a probe will definitely disturb the system by heating the membrane and the measured $\bar{n}$ will be higher than $\bar{n}$ without the probe.

If two probes are used simultaneously at $\omega_{\mathrm{cav}} \pm \omega_m$ then the intracavity photon number due to the probe will be 23 times higher than the intracavity photon number due to the cooling light fields which is much better but still may heat the membrane.

A way out can be to use a single photon detector instead of the balanced photodetector to increase the sideband measurement sensitivity. The pump photons must be filtered out by the filtering cavities as discussed in Chapter 6. The expected rate of detection of the Stokes and anti-Stokes photons are much higher than the dark count rate of our detectors making a non-disturbing measurement of $\bar{n}$ possible.

We also proposed a method to measure how much the membrane is heated due to the intracavity light fields. A cooling light field is sent to the cryogenic cavity and its light intensity is varied. If the measured anti-Stokes scattering rate is independent of the cooling light intensity for a certain intensity range then the membrane is not heated. Otherwise, it's possible to make an absolute measurement of the membrane temperature as a function of the intracavity photon number. This would require the ability to trace the cavity resonant with a probe intensity < 1 nW. We demonstrated locking with light intensity of 2 nW with some room to further decrease the required probe intensity. Alternatively, the modulation of the cryogenic cavity resonance frequency by the cryostat pulse tube should be removed and the cooling laser should be locked to a reference cavity.

These considerations show that the introduction of the filtering cavities together with SNSPD detection create an opportunity for new exciting experiments.

8

Summary

The work presented in this thesis is the continuation of a long-term research program towards the investigation of macroscopic quantum superpositions. At the start of the presented PhD research, optomechanics with trampoline resonators holding a DBR mirror had been investigated [78, 87]. Although a state transfer of a classical state between two mechanical modes coupled by two detuned light fields was achieved [12] the operation in the quantum regime remained elusive. Two main complications were found. Light absorption in the DBR stack resulted in significant heating of the device: 300 nW resonant readout probe laser light (after mode matching taken into account) resulted in an increase of the device temperature from 200 mK to 1 K [78]. We find it not a prohibitively large heating which might limit the operation in the quantum regime. A more significant drawback of this optomechanical system was a limited mechanical quality factor of $Q = 0.4 \times 10^6$ at cryogenic temperatures [87] for modes with frequency $\omega_m \sim 0.5$ MHz. Clamping losses at the points where the trampoline meets the DBR stack and bending losses in the DBR stack itself were identified as the main sources of mechanical dissipation. Such a modest mechanical quality factor results in the quantum coherence time $\tau \leq \frac{Q\hbar}{k_B T} = 4$ μs at 1 K being approximately equal to the mechanical oscillation period of the device. Coherent optomechanical manipulation would require multiphoton optomechanical coupling of $g \gtrsim 1$ MHz. The methods for high-fidelity state transfer between mechanical modes [12, 75] require the sideband-resolved regime $\kappa \ll \omega_m \sim 1$ MHz and weak optomechanical coupling $g \ll \kappa$, these requirements cannot be satisfied for the trampoline devices.

Another complication was maintaining optical alignment during cooling down. The cryogenic setup for the trampoline devices was highly asymmetric and had 7 low temperature actuators to compensate for the misalignment effects during cooling down. When cold, the set up had a modest mode coupling of 0.33 and it was challenging to lock the probe laser to the cavity resonance even with a fourth order mechanical low-pass filter installed in the cryostat [79].

To address these limitations we started with building an axisymmetric room temperature membrane-in-the-middle setup, described in Chapter 2. Using this setup

and a commercially available SiN membrane we achieved a strongly squeezed thermal state of a mechanical mode. One of the quadratures was cooled by the parametric driving. This is a well known technique possessing a limit of 3 dB squeezing due to divergence of the other quadrature. Our contribution was to apply a viscous damping force to this diverging quadrature via electrostatic interaction which allowed to reach 8.5 dB squeezing.

At room temperature the quality factors of commercially available SiN membranes are reaching 50×10^6 [88] when special care is taken to properly clamp these devices. In [88] it was reported that the major source of dissipation is through radiation losses from the membrane to the substrate. To avoid the radiation losses together with the bending losses at at the interface between the membrane and the substrate we adopted the idea of localizing the mechanical mode far away from the membrane-substrate boundary by creating a defect in the phononic crystal patterned on the membrane [7]. We observed quality factors as high as 40×10^6 for a 1.3 MHz mode at room temperature which allowed us to demonstrate optomechanical Stimulated Raman Adiabatic Passage (STIRAP) between two mechanical modes [75] described in Chapter 3. We didn't pick the best device out of tens of devices which might increase the quality factor to approximately 100×10^6 according to [7].

In Chapter 4 we investigate the possibility to create and transfer a single phonon mechanical Fock state between two high-Q modes using STIRAP at cryogenic temperatures. We found it feasible with state-of-the-art membranes under the assumption that the STIRAP pulses do not heat the membranes above 1 K. The state preparation and read out requires filtering out the driving pulses and high fidelity detection of the Stokes and anti-Stokes single photons. We also explored the possibility to create and detect entangled mechanical states via fractional STIRAP.

The optical cavity used in the experiments of Chapters 2 and 3 is close to concentric which makes the optical alignment very sensitive to lateral shifts of the cavity mirrors. To have the optical mode reasonably parallel to the mechanical axis the cavity mirrors should be positioned with lateral precision of ~ 100 μm. We found that by manually shifting one of the cavity mirrors laterally it was possible to achieve the required relative position of the two mirrors. This observation inspired the design of the cryogenic cavity where the cavity mirrors are shifted laterally with precision screws to make the optical mode parallel to the mechanical axis of symmetry. In addition, instead of an asymmetric design of the periscope for coupling to a single mode fiber we used the same idea of lateral shift of the mode matching lenses instead of tilting optical elements. Keeping the whole setup axisymmetric and made of Invar we found that the cavity remained reasonably well aligned when cooled to cryogenic temperatures without any actuators. During one of the cool downs we saw a monotonic decrease of the optical coupling with decrease in temperature. During warming up of the cryostat the setup was heated ~ 5 degrees Celcius above the room temperature and the coupling went up above the room temperature coupling to our surprise. We realized that the optical alignment was suboptimal and the cavity can be pre-aligned in such a way to compensate for the misalignment during cooling down. That worked - in the subsequent cool down the optical coupling between the fiber and the cavity increased from 0.8 at room temperature to 0.96 at 130 K and then stabilized at 0.93 at 20 mK after the precompensation has been made. The cryogenic

cavity allows for high collection efficiency of Stokes and anti-Stokes photons and has a stiff design. When a membrane is placed in the cryogenic cavity we didn't see a decrease in the external coupling to the linewidth ratio $\kappa_{\rm ext}/\kappa$. A probe laser can be easily locked to the cavity with a membrane when the setup is at mK temperatures, which allowed us to measure the mechanical ring down of one of the defect modes corresponding to $Q = 200 \times 10^6$. The cryogenic cavity is discussed in Chapter 5.

In addition to high quality mechanical modes and low temperature optomechanical quantum STIRAP requires an optical filter to filter out the pump pulses while transmitting the optomechanically scattered photons to a single photon detector. In Chapter 6 we are discussing an implementation of such a filter with the design transmissivity of 0.85 on resonance and attenuation of the unwanted light $> 10^{14}$ detuned by 1 MHz from the filter resonance. The filter was adapted from [66], it consists of 4 consecutive narrow linewidth optical cavities kept on resonance by feedback loops controlled by microprocessors. We proceed by evaluating the performance of superconducting nanowire single photon detectors aimed to register the optomechanically scattered photons. The requirement of the quantum STIRAP is an overall detection efficiency of $\gtrsim 0.05$ and a dark count rate of $\lesssim 10$ Hz. Our detectors were measured to have system detection efficiency > 0.9 and dark count rate ~ 0.01 Hz.

It is still an open question how much the membrane will be heated by the STIRAP pulses which might also affect the quality factor. In Chapter 7 we are addressing this issue by proposing a thermometry technique based on measuring the anti-Stokes scattering rate $\Gamma_{\rm AS} = \frac{k_B T}{Q\hbar}$ produced by a sideband cooling light fields. This method allows to estimate the increase of the membrane temperature when the STIRAP driving pulses are switched on. Under the assumption that the membrane is not heated by the intracavity light $\Gamma_{\rm AS}$ does not change when the intracavity photon number is varied from $\sim 10^3$ when the heating is most likely negligible to $\sim 10^7$ required to drive STIRAP. Any increase of measured $\Gamma_{\rm AS}$ with an increase of the cooling light fields intensity will signify the proportional increase of temperature of the membrane (more precisely T/Q).

At the moment of writing the thesis the complete setup for quantum optomechanical experiments is being finalized: the cryogenic cavity, high-quality membranes and single photon detectors are in place, while the optical filter setup together with its support and its vacuum chamber is produced and is in process of assembly. The control of the optical filter also requires extra attention.

We are planning to investigate membrane heating, a shot noise limited balanced detector is being produced for this purpose by our electronic department. The next step after the filter setup is ready will be preparation of a single phonon state via detection of a heralding Stokes photon and eventually STIRAP of a non-classical mechanical state between two modes of a membrane.

Samenvatting

Het werk dat in dit proefschrift wordt gepresenteerd, is de voortzetting van een lange termijn onderzoeksprogramma met als doel het bestuderen van macroscopische kwantumsuperposities. Aan het begin van het gepresenteerde promotieonderzoek werd de optomechanica onderzocht van een zogenaamde trampoline-resonator met een klein spiegeltje, met een diameter van ongeveer de dikte van een haar, in het midden [78, 87]. Hoewel een toestandsoverdracht van een klassieke toestand tussen twee mechanische modi gekoppeld door twee ontstemde lichtvelden werd bereikt [12] bleef de operatie in het kwantumregime ongrijpbaar. Er werden twee belangrijke complicaties gevonden. Lichtabsorptie in de spiegel resulteerde in een aanzienlijke verwarming van het sample: 300 nW resonant laserlicht, nodig voor het controleren en uitlezen van de mechanische beweging, resulteerde in een verhoging van de temperatuur van het sample van 200 mK naar 1 K [78]. We verwachten echter niet dat dit verwarmingseffect de werking in het kwantumregime onmogelijk zal maken. Een belangrijke tekortkoming van dit optomechanische systeem was een beperkte mechanische kwaliteitsfactor van $Q = 0.4 \times 10^6$ bij cryogene temperaturen [87] voor modi met een frequentie $\omega_m \sim 0.5$ MHz. Klemverliezen op de punten waar de trampoline het spiegltje ontmoet en buigverliezen in het spiegeltje zelf werden geïdentificeerd als de belangrijkste bronnen van mechanische dissipatie. Een dergelijke bescheiden mechanische kwaliteitsfactor leidt ertoe dat de kwantumcoherentietijd $\tau \leq \frac{Q\hbar}{k_B T} = 4$ μs bij 1 K ongeveer gelijk is aan de mechanische oscillatieperiode van het sample. Coherente optomechanische manipulatie zou multifoton optomechanische koppeling van $g \gtrsim 1$ MHz vereisen. De methoden voor high-fidelity toestandsoverdracht tussen mechanische modi [12, 75] vereisen het zijband-opgeloste regime $\kappa \ll \omega_m \sim 1$ MHz en zwakke optomechanische koppeling $g \ll \kappa$. Deze vereisten kunnen niet gerealiseerd worden voor de trampoline-spiegel-samples en alternatieve samples zijn noodzakelijk.

De tweede complicatie was het handhaven van de optische uitlijning tijdens het afkoelen van het sample. De cryogene opstelling voor de trampoline-spiegel-

samples was zeer asymmetrisch en had zeven lage-temperatuur actuatoren om de veranderingen in de uitlijning tengevolge van het afkoelen te compenseren. Bij lage temperaturen had de opstelling een bescheiden moduskoppeling van 0,33 en het was een grote uitdaging om de laserfrequentie te vergrendelen op een optische trilholte frequentie, zelfs na het dempen van mechanische vibraties met behulp van een mechanisch laagdoorlaatfilter van de vierde orde geïnstalleerd in de cryostaat [79].

Om deze beperkingen aan te pakken, zijn we begonnen met het bouwen van een axisymmetrische membraan-in-het-midden opstelling bij kamertemperatuur, zoals beschreven in hoofdstuk 2. Met behulp van deze opstelling en een commercieel verkrijgbaar SiN-membraan bereikten we een sterk samengedrukte (”squeezed”) thermische toestand van een mechanische modus. Eén van de kwadraturen van het optische veld in de resonator werd gekoeld door de parametrische aansturing. Dit is een bekende techniek met een limiet van 3 dB samendrukken als gevolg van divergentie van de andere kwadratuur. Onze bijdrage was het toepassen van een viskeuze dempingskracht op deze divergerende kwadratuur via elektrostatische interactie, waardoor een samendrukking van 8,5 dB kon worden bereikt.

Bij kamertemperatuur bereiken de kwaliteitsfactoren van de commercieel verkrijgbare SiN-membranen 50×10^6 [88] wanneer speciale zorg wordt besteed aan het correct vastmaken van deze samples in een houder. In [88] werd vermeld dat de belangrijkste bron van dissipatie de koppeling van mechanische modi van het membraan met modi in het substraat dat het membraan vasthoudt is. Om deze verliezen samen met de buigverliezen van het membraan op het grensvlak tussen het membraan en het substraat te vermijden, hebben we ervoor gekozen om de mechanische modus ver weg van de membraan-substraatgrens te lokaliseren door een defect te creëren in het fononische kristal dat op het membraan is gevormd [7]. We observeerden kwaliteitsfactoren van wel 40×10^6 voor een 1,3 MHz-modus bij kamertemperatuur, wat ons in staat stelde om optomechanische gestimuleerde Raman Adiabatic Passage (STIRAP) aan te tonen tussen twee mechanische modi [75], zoals beschreven in hoofdstuk 3.

In Hoofdstuk 4 onderzoeken we de mogelijkheid om een enkele fonon mechanische Fock-toestand te creëren en over te dragen tussen twee hoge-Q-modi met STIRAP bij cryogene temperaturen. We concluderen dat dit inderdaad haalbaar moet zijn zolang de STIRAP-pulsen het membraan niet tot boven 1 K zullen verwarmen. De voorbereiding en uitlezing van de toestand vereist het uitfilteren van de aandrijflaser-pulsen en high-fidelity detectie van de Stokes en anti-Stokes enkele fotonen. We hebben ook de mogelijkheid onderzocht om verstrengelde mechanische toestanden te creëren en te detecteren via fractionele STIRAP.

De optische trilholte die in de experimenten van Hoofdstuk 2 en 3 is gebruikt, is bijna concentrisch, wat de optische uitlijning erg gevoelig maakt voor laterale verschuivingen van de spiegels die de trilholte vormen. Om de optische modus redelijk parallel aan de mechanische as te verkrijgen, moeten de trilholtespiegels met een laterale precisie van ~ 100 μm worden gepositioneerd. We ontdekten dat het mogelijk was om door een van de trilholtespiegels handmatig zijdelings te verschuiven, de vereiste relatieve positie van de twee spiegels te bereiken. Deze observatie inspireerde het ontwerp van de cryogene trilholte waarbij de spiegels zijdelings worden verschoven met precisieschroeven om de optische modus evenwijdig aan de

mechanische symmetrie-as te verkrijgen. Bovendien gebruikten we in plaats van een asymmetrisch ontwerp van de periscoop voor koppeling met een single-mode glasvezel hetzelfde idee van laterale verschuiving van de mode-matching lenzen in plaats van optische elementen te kantelen. Door de hele opstelling axisymmetrisch te houden en geheel uit Invar te maken, bleek dat de trilholte redelijk goed uitgelijnd bleef wanneer die gekoeld werd tot cryogene temperaturen. Tijdens één van de afkoelingen zagen we een monotone afname van de optische koppeling bij afname van de temperatuur. Tijdens het opwarmen van de cryostaat werd de opstelling ~ 5 graden Celsius boven de kamertemperatuur verwarmd en de koppeling ging tot onze verbazing boven de kamertemperatuur koppeling. We realiseerden ons dat de optische uitlijning suboptimaal was en dat de trilholte vooraf kan worden uitgelijnd op een zodanige manier om de veranderende uitlijning tijdens het afkoelen te compenseren. Dat werkte - in de daaropvolgende afkoeling nam de optische koppeling tussen de glasvezel en de trilholte toe van 0,8 bij kamertemperatuur tot 0,96 bij 130 K en stabiliseerde zich vervolgens op 0,93 bij 20 mK nadat de voorcompensatie was ingevoerd. De cryogene trilholte zorgt voor een hoge verzamelefficiëntie van Stokes- en anti-Stokes-fotonen en heeft een uiterst stabiel ontwerp. Bij het plaatsen van een membraan in de cryogene trilholte zagen we geen afname van de externe koppeling met de lijnbreedteverhouding $\kappa_{\rm ext}/\kappa$. Door de hoge stabiliteit kon een laserbundel gemakkelijk aan het optomechanische systeem vergrendeld worden ("laser locking") wanneer de opstelling bij mK-temperaturen was, waardoor we de mechanische "ringdown" van één van de defectmodi konden meten die overeenkomt met $Q = 200 \times 10^6$. De cryogene trilholte wordt besproken in hoofdstuk 5.

Naast mechanische modi van hoge kwaliteit en optomechanische kwanta (fononen) bij lage temperatuur vereist STIRAP een optisch filter om de pomp-laser-pulsen uit te filteren terwijl de optomechanisch verstrooide fotonen naar een enkele fotondetector worden gestuurd. In Hoofdstuk 6 bespreken we een implementatie van zo'n filter met de ontwerptransmissiviteit van 0,85 op resonantie en verzwakking van het ongewenste licht $> 10^{14}$ ontstemd met 1 MHz van de filterresonantie. Het filter is aangepast van [66], het bestaat uit vier opeenvolgende optische trilholtes met smalle lijnbreedte die op resonantie worden gehouden door feedbacklussen die worden bestuurd door microprocessors. We gaan verder met het evalueren van de prestaties van supergeleidende nanodraad enkele-fotondetectoren die bedoeld zijn om de optomechanisch verstrooide fotonen te registreren. De eis van de quantum STIRAP is een algehele detectie-efficiëntie van $\gtrsim 0.05$ en een donkere telsnelheid ("dark counts") van lager dan 10 Hz. Onze detectoren hebben een systeemdetectie-efficiëntie van $> 0,9$ en een donkere telsnelheid van $\sim 0,01$ Hz.

Het is nog een open vraag hoeveel het membraan zal worden verwarmd door de STIRAP-pulsen, wat ook de kwaliteitsfactor kan beïnvloeden. In hoofdstuk 7 pakken we dit probleem aan door een thermometrietechniek voor te stellen die gebaseerd is op het meten van de anti-Stokes-verstrooiingssnelheid $\Gamma_{\rm AS} = \frac{k_B T}{Q\hbar}$ geproduceerd door een laserbundel afgesteld in frequentie op een mechanische zijband van een trilholte modus. Met deze methode kan de stijging van de membraantemperatuur worden geschat wanneer de STIRAP-stuurpulsen worden ingeschakeld. In de veronderstelling dat het membraan niet wordt verwarmd door het laserveld in de trilholte, verandert $\Gamma_{\rm AS}$ niet wanneer het aantal fotonen in de trilholte wordt gevarieerd van

$\sim 10^3$ wanneer de verwarming hoogstwaarschijnlijk verwaarloosbaar is tot $\sim 10^7$ vereist om STIRAP te besturen. Uit de toename van de gemeten Γ_{AS} met een toename van de intensiteit van de koelende lichtvelden zal de proportionele toename van de temperatuur van het membraan kunnen worden berekend.

Op het moment van schrijven van het proefschrift wordt de volledige opstelling voor optomechanische kwantumexperimenten afgerond: de cryogene trilholte, hoogwaardige membranen en enkele fotondetectoren zijn op hun plaats, terwijl de optische filteropstelling samen met de daarbij behorende vacuümkamer wordt geïnstalleerd. Ook de aansturing van het optische filter vraagt extra aandacht.

We zijn van plan om membraanverwarming te onderzoeken, en hiervoor wordt door onze elektronische afdeling een "shot-noise-limited" gebalanceerde detector geproduceerd. De volgende stappen nadat de filteropstelling klaar is, zijn de demonstratie van een enkele fonontoestand via detectie van een Stokes-foton en de demonstratie van STIRAP van een niet-klassieke mechanische toestand tussen twee modi van een membraan.

Bibliography

[1] Vladimir B. Braginski and Yurii I. Vorontsov, Sov. Phys. Usp. **17**, 644 (1975).

[2] V. B. Braginsky, Y. I. Vorontsov, and S. T. Kip, Science **209**, 547 (1980).

[3] J. D. Cohen, S. M. Meenehan, G. S. MacCabe, S. Gröblacher, A. H. Safavi-Naeini, F. Marsili, M. D. Shaw, and O. Painter, Nature **520**, 522 (2015).

[4] R. Riedinger, A. Wallucks, I. Marinković, C. Löschnauer, M. Aspelmeyer, S. Hong, and S. Gröblacher, Nature **556**, 473 (2018).

[5] G. S. MacCabe, H. Ren, J. Luo, J. D. Cohen, H. Zhou, A. Sipahigil, M. Mirhosseini, and O. Painter, Science **370**, 840 (2020).

[6] J. Chan, T. P. Alegre, A. H. Safavi-Naeini, J. T. Hill, A. Krause, S. Gröblacher, M. Aspelmeyer, and O. Painter, Nature **478**, 89 (2011).

[7] Y. Tsaturyan, A. Barg, E. S. Polzik, and A. Schliesser, Nature Nanotechnology **12**, 776 (2017).

[8] L. Midolo, A. Schliesser, and A. Fiore, Nature Nanotechnology **13**, 11 (2018).

[9] M. Aspelmeyer, T. J. Kippenberg, and F. Marquardt, Reviews of Modern Physics **86**, 1391 (2014).

[10] W. Marshall, C. Simon, R. Penrose, and D. Bouwmeester, Physical Review Letters **91**, 130401 (2003).

[11] R. Penrose, General Relativity and Gravitation **28**, 581 (1996).

[12] M. J. Weaver, F. Buters, F. Luna, H. Eerkens, K. Heeck, S. De Man, and D. Bouwmeester, Nature Communications **8**, 824 (2017).

[13] N. V. Vitanov, A. A. Rangelov, B. W. Shore, and K. Bergmann, Reviews of Modern Physics **89**, 015006 (2017).

[14] H. Xu, D. Mason, L. Jiang, and J. G. Harris, Nature **537**, 80 (2016).

[15] H. Xu, L. Jiang, A. A. Clerk, and J. G. Harris, Nature **568**, 65 (2019).

[16] U. Gaubatz, P. Rudecki, M. Becker, S. Schiemann, M. Külz, and K. Bergmann, Chemical Physics Letters **149**, 463 (1988).

[17] W. P. Bowen and G. J. Milburn, *Quantum Optomechanics* (2015), ISBN 9781107002173, URL `http://www.tandfonline.com/doi/abs/10.1080/00107514.2011.587535`.

[18] A. M. Jayich, J. C. Sankey, B. M. Zwickl, C. Yang, J. D. Thompson, S. M. Girvin, A. A. Clerk, F. Marquardt, and J. G. Harris, New Journal of Physics **10**, 095008 (2008).

[19] C. U. Lei, A. J. Weinstein, J. Suh, E. E. Wollman, A. Kronwald, F. Marquardt, A. A. Clerk, and K. C. Schwab, Physical Review Letters **117**, 100801 (2016).

[20] D. Rugar and P. Grütter, Physical Review Letters **67**, 699 (1991).

[21] F. Difilippo, V. Natarajan, K. R. Boyce, and D. E. Pritchard, Physical Review Letters **68**, 2859 (1992).

[22] A. A. Clerk, F. Marquardt, and K. Jacobs, New Journal of Physics **10**, 095010 (2008).

[23] M. R. Vanner, I. Pikovski, G. D. Cole, M. S. Kim, Č. Brukner, K. Hammerer, G. J. Milburn, and M. Aspelmeyer, Proceedings of the National Academy of Sciences of the United States of America **108**, 16182 (2011).

[24] A. Szorkovszky, A. C. Doherty, G. I. Harris, and W. P. Bowen, Physical Review Letters **107**, 213603 (2011).

[25] X. You, Z. Li, and Y. Li, Physical Review A **96**, 063811 (2017).

[26] J. B. Hertzberg, T. Rocheleau, T. Ndukum, M. Savva, A. A. Clerk, and K. C. Schwab, Nature Physics **6**, 213 (2010).

[27] J. Suh, A. J. Weinstein, C. U. Lei, E. E. Wollman, S. K. Steinke, P. Meystre, A. A. Clerk, and K. C. Schwab, Science **344**, 1262 (2014).

[28] E. E. Wollman, C. U. Lei, A. J. Weinstein, J. Suh, A. Kronwald, F. Marquardt, A. A. Clerk, and K. C. Schwab, Science **349**, 6251, p.952 (2015).

[29] F. Lecocq, J. B. Clark, R. W. Simmonds, J. Aumentado, and J. D. Teufel, Physical Review X **5**, 041037 (2015).

[30] J. M. Pirkkalainen, E. Damskägg, M. Brandt, F. Massel, and M. A. Sillanpää, Physical Review Letters **115**, 243601 (2015).

[31] A. Vinante and P. Falferi, Physical Review Letters **111**, 207203 (2013).

[32] M. Poot, K. Y. Fong, and H. X. Tang, New Journal of Physics **17**, 043056 (2015).

[33] A. Pontin, M. Bonaldi, A. Borrielli, F. S. Cataliotti, F. Marino, G. A. Prodi, E. Serra, and F. Marin, Physical Review Letters **112**, 023601 (2014).

[34] R. W. Drever, J. L. Hall, F. V. Kowalski, J. Hough, G. M. Ford, A. J. Munley, and H. Ward, Applied Physics B Photophysics and Laser Chemistry **31**, 97 (1983).

[35] B. Hu and Y. Zhang, Modern Physics Letters A **8**, 37, 3575 (1993).

[36] P. Pillet, Physical Review A - Atomic, Molecular, and Optical Physics **48**, 845 (1993).

[37] J. L. Sørensen, D. Møller, T. Iversen, J. B. Thomsen, F. Jensen, P. Staanum, D. Voigt, and M. Drewsen, New Journal of Physics **8**, 261 (2006).

[38] K. S. Kumar, A. Vepsälaïnen, S. Danilin, and G. S. Paraoanu, Nature Communications **7**, 10628 (2016).

[39] H. Goto and K. Ichimura, Physical Review A - Atomic, Molecular, and Optical Physics **75**, 033404 (2007).

[40] D. A. Golter and H. Wang, Physical Review Letters **112**, 116403 (2014).

[41] S. Longhi, Laser and Photonics Reviews **3**, 243 (2009).

[42] J. Simon, H. Tanji, S. Ghosh, and V. Vuletic, Nature Physics **3**, 765 (2007).

[43] H.-S. Chang, Y. Zhong, A. Bienfait, M.-H. Chou, C. R. Conner, É. Dumur, J. Grebel, G. A. Peairs, R. G. Povey, K. J. Satzinger, et al., Physical Review Letters **124**, 240502 (2020).

[44] K. Toyoda, K. Uchida, A. Noguchi, S. Haze, and S. Urabe, Physical Review A - Atomic, Molecular, and Optical Physics **87**, 052307 (2013).

[45] Y. D. Wang and A. A. Clerk, Physical Review Letters **108**, 153603 (2012).

[46] L. Tian, Physical Review Letters **108**, 153604 (2012).

[47] D. Garg, A. K. Chauhan, and A. Biswas, Physical Review A **96**, 023837 (2017).

[48] L. F. Buchmann and D. M. Stamper-Kurn, Physical Review A - Atomic, Molecular, and Optical Physics **92**, 013851 (2015).

[49] A. Noguchi, R. Yamazaki, M. Ataka, H. Fujita, Y. Tabuchi, T. Ishikawa, K. Usami, and Y. Nakamura, New Journal of Physics **18** (2016).

[50] C. F. Ockeloen-Korppi, E. Damskägg, J. M. Pirkkalainen, M. Asjad, A. A. Clerk, F. Massel, M. J. Woolley, and M. A. Sillanpää, Nature **556**, 478 (2018).

[51] S. Kotler, G. A. Peterson, E. Shojaee, F. Lecocq, K. Cicak, A. Kwiatkowski, S. Geller, S. Glancy, E. Knill, R. W. Simmonds, et al., Science **372**, 622 (2021).

[52] L. Mercier de Lépinay, C. F. Ockeloen-Korppi, M. J. Woolley, and M. A. Sillanpää, Science **372**, 625 (2021).

[53] C. Dong, V. Fiore, M. C. Kuzyk, and H. Wang, Science **338**, 1609 (2012).

[54] J. D. Thompson, B. M. Zwickl, A. M. Jayich, F. Marquardt, S. M. Girvin, and J. G. Harris, Nature **452**, 72 (2008).

[55] S. Schmid, K. D. Jensen, K. H. Nielsen, and A. Boisen, Physical Review B - Condensed Matter and Materials Physics **84**, 165307 (2011).

[56] A. Kuhn, G. W. Coulston, G. Z. He, S. Schiemann, K. Bergmann, and W. S. Warren, The Journal of Chemical Physics **96**, 4215 (1992).

[57] M. Dupont-Nivet, M. Casiulis, T. Laudat, C. I. Westbrook, and S. Schwartz, Physical Review A - Atomic, Molecular, and Optical Physics **91**, 053420 (2015).

[58] H. K. Xu, C. Song, W. Y. Liu, G. M. Xue, F. F. Su, H. Deng, Y. Tian, D. N. Zheng, S. Han, Y. P. Zhong, et al., Nature Communications **7**, 11018 (2016).

[59] J. Klein, F. Beil, and T. Halfmann, Physical Review A - Atomic, Molecular, and Optical Physics **78**, 033416 (2008).

[60] H. Theuer and K. Bergmann, European Physical Journal D **2**, 279 (1998).

[61] P. Marte, P. Zoller, and J. L. Hall, Physical Review A **44**, 4118 (1991).

[62] R. Unanyan, M. Fleischhauer, B. W. Shore, and K. Bergmann, Optics Communications **155**, 144 (1998).

[63] M. Rossi, D. Mason, J. Chen, Y. Tsaturyan, and A. Schliesser, Nature **563**, 53 (2018).

[64] R. W. Peterson, T. P. Purdy, N. S. Kampel, R. W. Andrews, P. L. Yu, K. W. Lehnert, and C. A. Regal, Physical Review Letters **116**, 063601 (2016).

[65] M. Underwood, D. Mason, D. Lee, H. Xu, L. Jiang, A. B. Shkarin, K. Børkje, S. M. Girvin, and J. G. Harris, Physical Review A - Atomic, Molecular, and Optical Physics **92**, 061801(R) (2015).

[66] I. Galinskiy, Y. Tsaturyan, M. Parniak, and E. S. Polzik, Optica **7**, 718 (2020).

[67] Y. Zhai, Z. X. Chen, and Q. Lin, Journal of the Optical Society of America B **37**, 956 (2020).

[68] J. Johansson, P. Nation, and F. Nori, Computer Physics Communications **183**, 1760–1772 (2012).

[69] N. V. Vitanov, K.-A. Suominen, and B. W. Shore, J. Phys. B: At. Mol. Opt. Phys. **32**, 4535–4546 (1999).

[70] T. P. Purdy, R. W. Peterson, P. L. Yu, and C. A. Regal, New Journal of Physics **14**, 115021 (2012).

[71] A. G. Kuhn, J. Teissier, L. Neuhaus, S. Zerkani, E. Van Brackel, S. Deléglise, T. Briant, P. F. Cohadon, A. Heidmann, C. Michel, et al., Applied Physics Letters **104**, 044102 (2014).

[72] E. Verhagen, S. Deléglise, S. Weis, A. Schliesser, and T. J. Kippenberg, Nature **482**, 63 (2012).

[73] F. Fogliano, B. Besga, A. Reigue, L. Lépinay, P. Heringlake, C. Gouriou, E. Eyraud, W. Wernsdorfer, B. Pigeau, and O. Arcizet, Nature Communications **12**, 4124 (2021).

[74] R. Riedinger, S. Hong, R. A. Norte, J. A. Slater, J. Shang, A. G. Krause, V. Anant, M. Aspelmeyer, and S. Gröblacher, Nature **530**, 313 (2016).

[75] V. Fedoseev, F. Luna, I. Hedgepeth, W. Loffler, and D. Bouwmeester, Physical Review Letters **126**, 113601 (2021).

[76] M. J. Weaver, D. Newsom, F. Luna, W. Löffler, and D. Bouwmeester, Physical Review A **97**, 063832 (2018).

[77] R. W. Peterson, PhD thesis, University of Colorado at Boulder (2017), URL `https://ui.adsabs.harvard.edu/abs/2017PhDT.....47P/abstract`.

[78] F. Buters, PhD thesis, Leiden University (2017), URL `https://hdl.handle.net/1887/58471`.

[79] M. De Wit, G. Welker, K. Heeck, F. M. Buters, H. J. Eerkens, G. Koning, H. Van der Meer, D. Bouwmeester, and T. H. Oosterkamp, Review of Scientific Instruments **90**, 015112 (2019).

[80] S. L. D. t. Haaf, MSc thesis, Leiden University (2021), URL `https://hdl.handle.net/1887/3166726`.

[81] O. T. Huisman, BSc thesis, Leiden University (2021), URL `https://hdl.handle.net/1887/3194937`.

[82] R. Claessen, MSc thesis, Leiden University (2021), URL `https://scholarlypublications.universiteitleiden.nl/handle/1887/58471`.

[83] C. M. Natarajan, M. G. Tanner, and R. H. Hadfield, Superconductor Science and Technology **25**, 063001 (2012).

[84] F. Marsili, V. B. Verma, J. A. Stern, S. Harrington, A. E. Lita, T. Gerrits, I. Vayshenker, B. Baek, M. D. Shaw, R. P. Mirin, et al., Nature Photonics **7**, 210 (2013).

[85] A. J. Weinstein, C. U. Lei, E. E. Wollman, J. Suh, A. Metelmann, A. A. Clerk, and K. C. Schwab, Physical Review X **4**, 041003 (2014).

[86] M. Yuan, M. A. Cohen, and G. A. Steele, Applied Physics Letters **107**, 263501 (2015).

[87] M. J. Weaver, PhD thesis, UCSB (2018), URL https://www.proquest.com/openview/7bf96a761685c167f976f0d94a445176/1?pq-origsite=gscholar&cbl=18750.

[88] S. Chakram, Y. S. Patil, L. Chang, and M. Vengalattore, Physical Review Letters **112**, 127201 (2014).

Curriculum Vitae

Vitaly Fedoseev

6 May 1986
Born in Vinnytsia, Ukraine.

2003
Graduated from Ukrainian Lyceum of Physics and Mathematics.

2003
Silver medal at the 34th International Physics Olympiad, Taiwan.

2003-2007
Bachelor of Science in Applied Physics and Mathematics, Moscow Institute of Physics and Technology, Russia.

2007-2009
Master of Economics, International College of Economics and Finance, Russia.

2009-2013
High frequency trading in a Russian proprietary trading firm.

2013 - 2014
Visitor at Institute of Solid State Physics, Russia.

2014 - 2015
Master of Philosophy in Physics, Quantum Matter group, University of Cambridge, the UK.

2016
PhD candidate, Quantum Matter group, Leiden University, the Netherlands.

2017-2021
PhD candidate, Quantum Optics group, promotor Prof. D. Bouwmeester, Leiden University, the Netherlands.

from August 2022
Postdoctoral Associate, Center for Ultracold Atoms, MIT, USA. Hopefully, this will happen in spite of the war in Ukraine.

List of publications

1. **V. Fedoseev**, M. Fisicaro, H. van der Meer, W. Löffler and D. Bouwmeester, *Realignment-free cryogenic macroscopic optical cavity coupled to an optical fiber*, Rev. Sci. Instrum. 93, 013103 (2022)
   (Chapter 5 of this thesis)

2. **V. Fedoseev**, F. Luna, I. Hedgepeth, W. Löffler and D. Bouwmeester, *Stimulated Raman Adiabatic Passage in Optomechanics*, Phys. Rev. Lett. 126, 113601 (2021)
   (Chapters 3 and 4 of this thesis)

3. D. C. Newsom, F. Luna, **V. Fedoseev**, W. Löffler and D. Bouwmeester, *Optimal optomechanical coupling strength in multimembrane systems*, Phys. Rev. A 101, 033829 (2020)

4. S. Sonar, **V. Fedoseev**, M. J. Weaver, F. Luna, E. Vlieg, H. van der Meer, D. Bouwmeester and W. Löffler, *Strong thermomechanical squeezing in a far-detuned membrane-in-the-middle system*, Phys. Rev. A 98, 013804 (2018)
   (Chapters 2 of this thesis)

5. I. Battisti, **V. Fedoseev**, K. M. Bastiaans, A. de la Torre, R. S. Perry, F. Baumberger, and M. P. Allan, *Poor electronic screening in lightly doped Mott insulators observed with scanning tunneling microscopy*, Phys. Rev. B 95, 235141 (2017)

6. I. Battisti, K. M. Bastiaans, **V. Fedoseev**, A. de la Torre, N. Iliopoulos, A. Tamai, E. C. Hunter, R. S. Perry, J. Zaanen, F. Baumberger and M. P. Allan, *Universality of pseudogap and emergent order in lightly doped Mott insulators*, Nature Physics 13, 21–25 (2017)

7. V. Dremov, **V. Fedoseev**, P. Fedorov and A. Grebenko, *Fast and reliable method of conductive carbon nanotube-probe fabrication for scanning probe microscopy*, Rev. Sci. Instrum. 86, 053703 (2015)

Acknowledgements

During my PhD studies I learnt so much about optics, mechanics, electronics. Now I perceive myself as a researcher. For sure, that would not be possible without the effort of many people who supported me these years.

I am particularly grateful to my promotor Dirk Bouwmeester for guiding me. Thank you for your patience and letting me accomplish risky ideas.

I would like to thank Wolfgang Löffler for teaching me optics in the lab, day to day supervision and tackling all kinds of technical problems.

Many experiments would not be possible without technical expertise of Harmen van der Meer from Fine Mechanics Department. I was often amazed how Harmen was able to find practical solutions for our crazy projects.

I would like to thank Kier Heeck, Raymond Koehler and Harry Visser for support in electronics. I thank our secretary Henriette van Leeuwen.

I thank Frank Buters, Fernando Luna and Matthew Weaver for introducing me to the optical lab and the setups. I am grateful to Ian Hedgepeth for fruitful discussions. I thank Xinrui Wei and Leon Raabe who worked with me in the lab as well as Sameer Sonar, Matteo Fisicaro, Tim Fuchs, Remi Claessen, Bas ten Haaf, Owen Huisman.

Finally, I am indebted to my wife Nastya for supporting me and my son Yakov for inspiration.